THE UNIVERSITY OF
WARWICK

University of Warwick institutional repository: http://go.warwick.ac.uk/wrap

A Thesis Submitted for the Degree of PhD at the University of Warwick

http://go.warwick.ac.uk/wrap/3811

This thesis is made available online and is protected by original copyright.

Please scroll down to view the document itself.

Please refer to the repository record for this item for information to help you to cite it. Our policy information is available from the repository home page.

THE UNIVERSITY OF
WARWICK

AUTHOR: **Louella Judy Vasquez** DEGREE: **Ph.D.**

TITLE: **High Precision Multifractal Analysis in the 3D Anderson Model of Localisation**

DATE OF DEPOSIT: .....

I agree that this thesis shall be available in accordance with the regulations governing the University of Warwick theses.

I agree that the summary of this thesis may be submitted for publication.

I **agree** that the thesis may be photocopied (single copies for study purposes only).

Theses with no restriction on photocopying will also be made available to the British Library for microfilming. The British Library may supply copies to individuals or libraries. subject to a statement from them that the copy is supplied for non-publishing purposes. All copies supplied by the British Library will carry the following statement:

> "Attention is drawn to the fact that the copyright of this thesis rests with its author. This copy of the thesis has been supplied on the condition that anyone who consults it is understood to recognise that its copyright rests with its author and that no quotation from the thesis and no information derived from it may be published without the author's written consent."

AUTHOR'S SIGNATURE: .....

USER'S DECLARATION

1. I undertake not to quote or make use of any information from this thesis without making acknowledgement to the author.
2. I further undertake to allow no-one else to use this thesis while it is in my care.

DATE SIGNATURE ADDRESS

.....

.....

.....

.....

.....

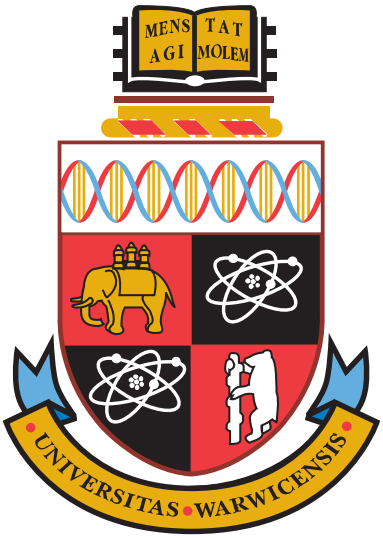

High Precision Multifractal Analysis in the 3D Anderson Model of Localisation

by

Louella Judy Vasquez

Thesis

Submitted to the University of Warwick

in partial fulfilment of the requirements

for admission to the degree of

Doctor of Philosophy

Department of Physics

July 2010

THE UNIVERSITY OF WARWICK

Contents

List of Tables

List of Figures

Acknowledgments

I am immensely grateful of the financial support from the University of Warwick via the Vice-Chancellor Studentship Award, the Theoretical Physics Group, the Institute of Advanced Study via the IAS Early Career Fellowship and EPSRC EP/C007042/1. I have spent three fruitful months in Japan with funding from Osaka University Fellowship where part of the work in finite-size scaling was started with Professor Keith Slevin. While in Osaka, I would like to acknowledge the hospitality of Akai Group headed by Professor Hisazumi Akai and the kindness of Miss Tomoko Shimokomaki. The results in this dissertation have been presented at various conferences for which I received financial support from the Theory Group and the Physics Department of the University of Warwick. All of the high performance computations in this work have been carried out at the Centre for Scientific Computing (CSC) - University of Warwick using CSC's IBM cluster and SGI Altix. I thank the whole staff of CSC for their utmost support, assistance and resources during my three years here. This dissertation has been completed with significant contributions from Professor Rudolf Römer and Dr. Alberto Rodriguez. These two gentlemen have given me their invaluable support throughout my Ph.D. They have inspired, challenged and taught me. To them, I am greatly and forever indebted. For their prayers and love, for welcoming me into their lovely homes, i thank my Filipino family in the UK. Maraming Salamat TGCM Coventry. For proofreading, 24/7 technical support, tlc, hot dinners, all the love and much more, I thank Karl Svensson. You are heaven sent, truly! Mahal na mahal kita. For their unwavering support and faith in me through these years, I thank my family back in the Philippines. If all else fail, I know that I could always go home and plant potatoes. I miss you all the time. I have written this thesis in memory of my papa Edilberto. He would have been proud of me. The resilience of the Filipino continues to be an inspiration. Mabuhay ang Pilipino. Mabuhay ang Pilipinas. Lastly, I dedicate this thesis to my first and greatest love, to the most important person in my life, for apart from Him I am nothing. To Jesus Christ, as always.

Declarations

I hereby declare that this dissertation entitled High Precision Multifractal Analysis in the 3D Anderson Model of Localisation is an original work and has not been submitted for a degree or diploma or other qualification at any other University. Chapters 1-2 provide information gathered from the literature as referenced to. Chapters 3-6 are based on the following published papers respectively:

- "Multifractal analysis of the metal-insulator transition in the 3D Anderson model I: Symmetry relation under typical averaging", L. J. Vasquez, A. Rodriguez, R. A. Römer, Phys. Rev. B 78, 195106-10 (2008)
- "Multifractal analysis of the metal-insulator transition in the 3D Anderson model II: Symmetry relation under ensemble averaging", A. Rodriguez, L. J. Vasquez, R. A. Römer, Phys. Rev. B 78, 195107-9 (2008)
- "Optimisation of multifractal analysis using box-size scaling", A. Rodriguez, L. J. Vasquez, R. A. Römer, Eur. Phys. J. B 67, 7782 (2009)
- "Multifractal analysis with the probability density function at the three-dimensional Anderson transition", A. Rodriguez, L. J. Vasquez, R. A. Römer, Phys. Rev. Lett. 102, 106406-4 (2009).

Chapter 7 is based on a published paper and a current work in progress:

- "Scaling law and critical exponent for α_0 at the 3D Anderson transition", L. J. Vasquez, K. Slevin, A. Rodriguez, R. A. Römer, Ann. Phys. (Berlin) 18, 901-904 (2009)
- "Finite size scaling from wavefunction amplitudes and multifractal exponents at the 3D Anderson transition", A. Rodriguez, L. J. Vasquez, K. Slevin, R. A. Römer, under review in Phys. Rev. Lett. 2010

The above-mentioned papers are results of a joint work with the indicated authors.

Abstract

This work presents a large scale multifractal analysis of the electronic state in the vicinity of the localisation-delocalisation transition in the three-dimensional Anderson model of localisation using high-precision data and very large system sizes of up to $L^3 = 240^3$. The multifractal analysis is implemented using box- and system- size scaling of the generalized inverse participation ratios employing typical and ensemble averaging techniques. The statistical analysis in this study has shown that in the thermodynamic limit a proposed symmetry relation in the multifractal exponents is true for the 3D Anderson model in the orthogonal universality class. Better agreement with the symmetry is found when using system-size scaling with ensemble averaging in which a more complete picture of the multifractal spectrum $f(\alpha)$ is also obtained. A complete profile of $f(\alpha)$ has negative fractal dimensions and shows the contributions coming from the tails of the distribution. Various box-partitioning approaches have been carefully studied such as the use of cubic and non-cubic boxes, periodic boundary conditions to enlarge the system, and single and multiple origins in the partitioning grid. The most reliable method is equal partitioning of a system into cubic boxes which has also been shown to be the least numerically expensive. Furthermore, this work gives an expression relating $f(\alpha)$ and the probability density function (PDF) of wavefunction intensities. The relation which contains a finite-size correction provides an alternative and simpler method to obtain $f(\alpha)$ directly from the PDF in which $f(\alpha)$ is interpreted as the scale-invariant distribution at criticality. Finally, a generalization of standard multifractal analysis which is applicable to the critical regime and not just at the critical point is presented here. Using this generalization together with finite-size scaling analysis, estimates of critical disorder and critical exponent based on exact diagonalization have been obtained that are in excellent agreement, supporting for the first time previous results of transfer matrix calculations.

Chapter 1

Introduction

1.1 Anderson model of localisation

The interest in this thesis is how electrons behave when the disorder in a lattice is sufficiently strong such that it can cause a transition from a metallic to an insulating state. By disorder, we mean the presence of impurities and distortions, both being randomly distributed in an otherwise perfect (clean and periodic) lattice. The picture of disorder for a travelling electron is a sea of random potential. Localisation of electrons happens as an interference effect due to multiple scatterings of the single particle electronic wavefunction with itself by a random potential. This phenomenon is first demonstrated by Anderson [1] in his seminal paper on the absence of diffusion in a simple system of noninteracting particles with random site potential energy and zero external fields. Since then, Anderson localisation [2–4] is experimentally observed in microwaves [5], ultrasound [6, 7], light waves [8, 9] quantum waves [10, 11] and cold atoms [12, 13].

If the phase coherence length l_φ of the electron is large compared with the system size L then the quantum interference effects become relevant and Anderson localisation for electrons can happen [4]. This regime is reached when temperature is sufficiently low such that inelastic electron-electron and electron-phonon scatterings

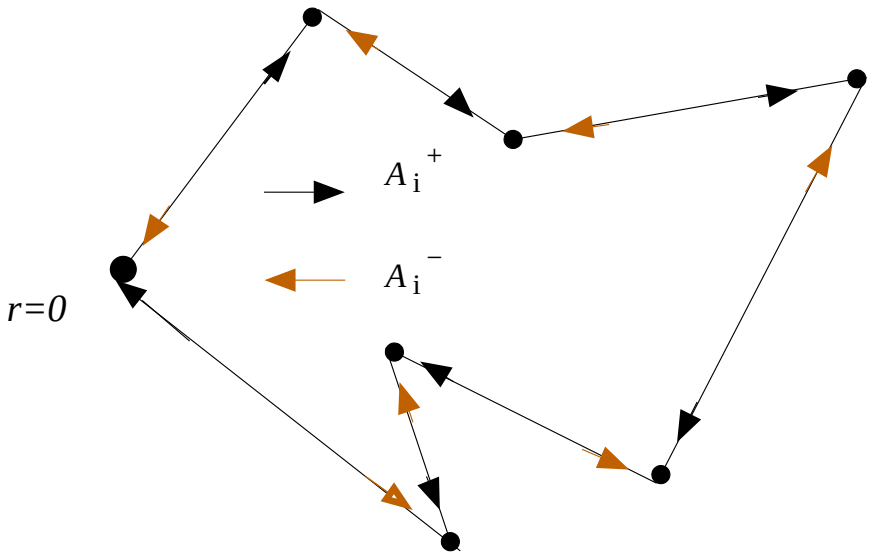

[t]

Figure 1.1: A schematic picture of coherent back-scattering of an electron by a random potential. An electron returns to its initial position at $r = 0$ with probability amplitude $A_i^+(t')$ after a series of scattering events as traced by the black arrows. The brown arrows trace the corresponding inverse path with probability amplitude $A_i^-(t')$.

are suppressed. We can visualize the coherent backscattering that causes localisation in the following manner [14, 15]. We consider an electron at point $\vec{r} = 0$ and time $t = 0$. The probability to return to the original point after some time $t = t'$ is given by

$$\mathcal{P}(t') = \left| \sum_{i \in S} A_i(t') \right|^2 , \tag{1.1}$$

where $A_i(t')$ is the probability amplitude of an electron that took the ith path to return to $\vec{r} = 0$ after a number of random scattering events. The return probability $\mathcal{P}(t')$ is the sum of all possible scattering paths S. Let us consider a simple illustration in Fig. 1.1. For every clockwise path S_i^+ traversed by an electron with probability amplitude $A_i^+(t')$, it is true that there exists a corresponding inverse or time reversal path S_i^- with $A_i^-(t')$. Hence, the set of all scattering paths S is a sum of these two subsets, i.e., $S = S^+ + S^-$. The return probability of the electron could

then be expressed as

$$\begin{aligned}
\mathcal{P}(t') &= \left| \sum_{i \in S^+} A_i(t') + \sum_{i \in S^-} A_i(t') \right|^2 \\
&= \left| \sum_{i \in S^+} A_i^+(t') + A_i^-(t') \right|^2 \\
&= \sum_{i \in S^+} \left| A_i^+(t') + A_i^-(t') \right|^2 + \sum_{i \neq j \in S^+} \left[A_i^+(t') + A_i^-(t') \right] \times \\
&\quad \left[A_j^+(t') + A_j^-(t') \right]^* . \qquad (1.2)
\end{aligned}$$

If there is time reversal symmetry such that the phase of the probability amplitude is preserved, i.e., $A_i^+(t') = A_i^-(t')$, then the above equation simplifies into $\mathcal{P}(t') = 4 \sum_{i \in S^+} |A_i(t')|^2$. Note that the second term in Eq. (1.2) which accounts for the interference effects between different scattering paths vanishes. In the classical case where the conductivity is defined by the Drude model, the return probability reduces to $\mathcal{P}(t') = 2 \sum_{i \in S^+} |A_i(t')|^2$. The enhancement by a factor of two of the return probability in the presence of coherent multiple backscattering simply means that the electrons are now more spatially restricted in a confined space. This picture which is brought upon by a significant degree of disorder offers a mechanism for the exponential localisation of the electrons. In Fig. 1.2, we present the one dimensional electronic eigenstate for the cases of weak and strong disorder. In the presence of weak disorder, the wavefunction amplitude ψ_i is on average uniform in space which means that the electron could be found anywhere and hence the state is extended. On the other hand if the disorder is strong enough to cause large backscatterings that can spatially confined the electron wavefunction then the state is localised. An example of which is shown in Fig. 1.2 where ψ_i is large in one region and decays in an exponential manner.

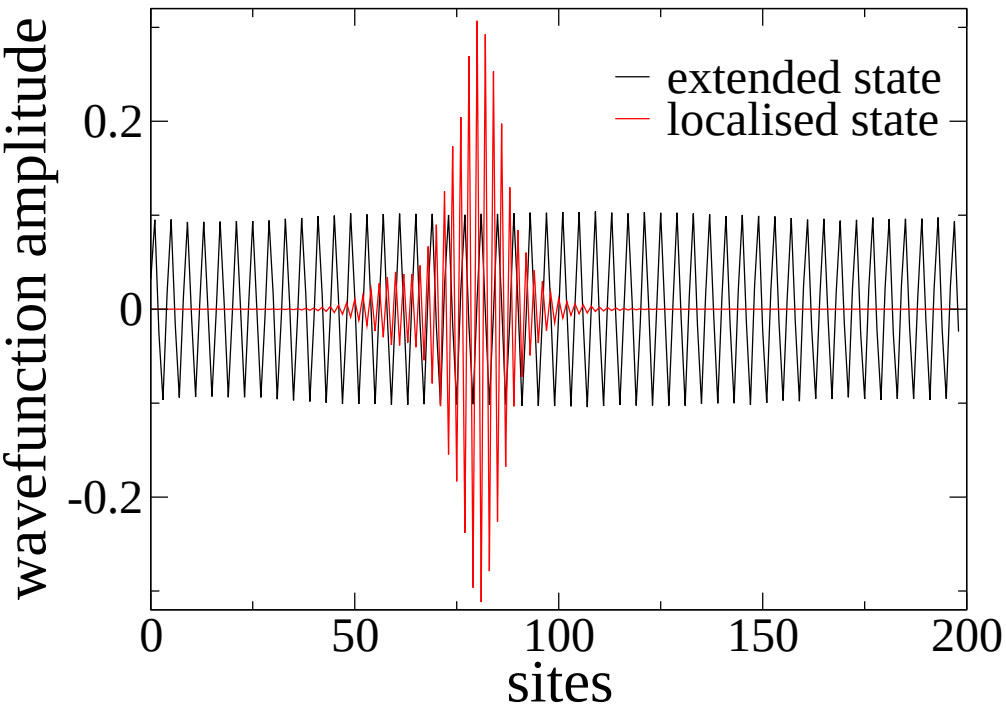

Figure 1.2: A comparison between an extended and localised electronic eigenstate. Shown here is the wavefunction amplitude for all 200 sites of a $1D$ lattice with length $L = 200$ in units of lattice spacing and periodic boundary condition imposed. Using a finite value of the parametrized disorder, the localised and extendend states here are found at the band edge and centre respectively.

1.2 Scaling theory of localisation

The scaling theory of localisation describes the dependence of the Anderson transition on the dimensionality of the system [16–18]. As a starting point, we consider the size-dependence of the conductance G. The conductance behaves as a measure of the effective disorder. It is finite for a metallic state and zero for an insulating state at absolute zero temperature. In units of e^2/h where e and h are the electronic charge and Planck's constant respectively, we have the dimensionless (Thouless) conductance $g = h/e^2\ G$ [19]. Here, $g(L, x)$ is only dependent on the system size L and x which represents the set of external parameters such as disorder, Fermi energy, pressure and electron density. The $g(L, x)$ generally does not depend on the microscopic details (e.g., unit cell) of the material.

The basic assumption of the scaling theory is that given a d-dimensional block with volume $(bL)^d$ and integer b its conductance will only be determined by the conductance of the b^d smaller blocks each with volume L^d that build up the larger block. In other words, the conductance can be expressed as

$$g(bL, x) = \mathcal{F}[g(L, x), b], \tag{1.3}$$

which simply means that a rescaling $g(L, x) \rightarrow g(bL, x)$ of the conductance can be defined by the function $g(L, x)$ and scaling factor b. In differential form, Eq. (1.3) can be expressed in dimensionless form as

$$\frac{\mathrm{d} \ln g(L, x)}{\mathrm{d} \ln L} = \beta(g). \tag{1.4}$$

Equation (1.4) states that the scaling function β is only dependent on $g(L, x)$. We will now obtain the asympotic behaviour of $\beta(g)$ for the limiting cases of small (localised insulating state) and big (extended metallic state) $g(L, x)$. When the random potential is weak, the electronic state is extended and plane wave-like. For a d-dimension system of size L, the Ohmic conductance for a metal is $G = 1/R = \sigma L^{d-2}$ where G is simply the inverse of the resistance R and σ is the d.c. conductivity of the material. When the disorder is sufficiently strong, the states very near the Fermi energy are localised. Electronic states nearly equal in energy are far apart from each other in space such that hopping between these states does not happen. The electronic wavefunction is exponentially localised and the conductance assumes the form $g = g_0 \ \mathrm{e}^{-L/\xi}$. The localisation length ξ defines the spatial extent of the wavefunction and here $L >> \xi$.

The scaling theory assumes that $\beta(g)$ is monotonic and that a continuous behaviour connecting the localised and extended regimes is possible. The scale-dependence of $\beta(g)$ is shown in Fig. 1.3. When $\beta > 0$ in the metallic case, the conductance increases with L and diverges in the thermodynamic limit. The asymp-

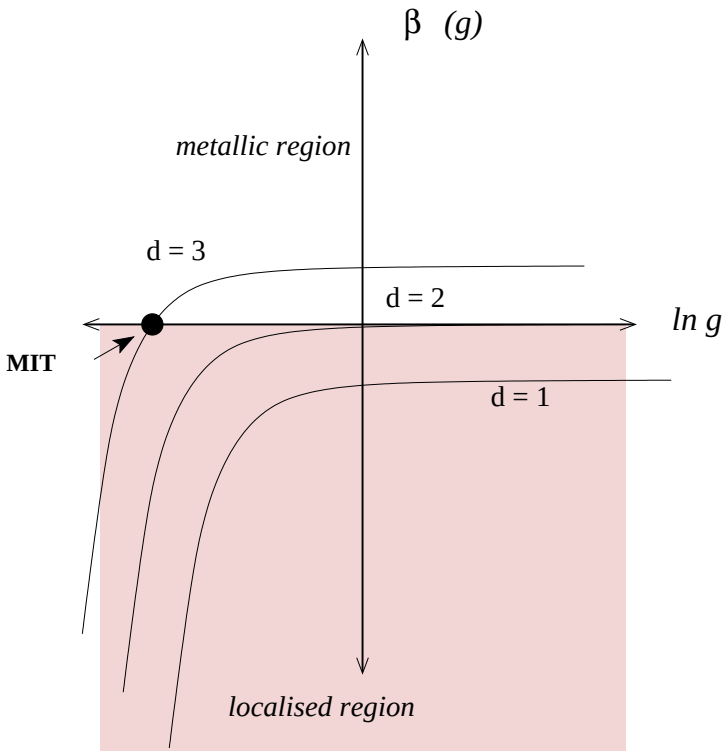

Figure 1.3: A schematic diagram showing the behaviour of the scaling function $\beta(g)$ for dimensions $d = 1, 2, 3$. The metallic region is $\beta > 0$. The localised region is the shaded part corresponding to $\beta < 0$. A crossing point at $\beta = 0$ for $d > 2$ indicates an MIT. According to the scale dependence of $\beta(g)$, there are no extended states for $d \leq 2$ in the presence of a finite degree of disorder.

totic behaviour of the function is $\beta(g) = d - 2$. For $\beta < 0$, g decreases with L and becomes zero as $L \to \infty$. In the latter case, $\beta(g) = \ln(g/g_0)$. The system becomes more metallic or insulating as it gets bigger in L. For $d \leq 2$, $\beta(g)$ is always negative. This means that in $d \leq 2$ unless it is a perfect conductor all electronic wavefunctions will always be localised and the system will always be an insulator in the presence of a finite disorder. This is not the case for $d = 3$. A crossover at $\beta = 0$ between the metallic and insulating regimes exists as seen in Fig. 1.3. At this critical point, the conductance does not depend on the system size and this scale-invariance implies that exactly at this point there is a metal to insulator transition (MIT). The set of parameters x such as disorder controls the value of $g(L, x)$. For instance, if the

disorder is weak then the state is in the extended region. If the disorder is strong enough, it is a localised state.

Near the critical transition, there is only one relevant length scale. It is the localisation length ξ in the localised regime or the correlation length between wave-function amplitudes in the extended region. The localisation (correlation) length diverges near the MIT and since it depends on x then it should diverge at the critical point $x = x_c$ as expressed by [20]

$$\xi \propto |x - x_c|^{-\nu}. \tag{1.5}$$

The critical exponent ν defines the Anderson transition and is the same regardless of the microscopic details for all systems belonging to one universality class or systems sharing the same symmetry in the Hamiltonian [21]. Furthermore, the scaling theory states that near the critical point of the Anderson transition all systems with finite length L can be scaled by the localisation length for $L \to \infty$. If so then the conductance or any measure characterizing critical properties can be described by one scaling function as

$$g(L, x) = \mathcal{F}\left(\frac{L}{\xi}\right). \tag{1.6}$$

Equations (1.3), (1.4) and (1.6) together is also known as one parameter scaling theory [2, 17, 18].

1.3 Numerical model

To model an electron in a disordered lattice, we use the single-electron tight-binding Anderson Hamiltonian as given by [22]

$$\mathcal{H} = \frac{p^2}{2m} + \sum_{i=1}^{N} U_i(r - R_i), \tag{1.7}$$

where m is an effective mass of an electron with momentum p, U_i is the potential energy of the i-th ion located at $r - R_i$ and the summation is for the total number of ionic sites N. The discrete version of this Hamiltonian in terms of lattice site basis is

$$\mathcal{H} = \sum_i \varepsilon_i \ |i\rangle\langle i| + \sum_{i \neq j} t_{ij} \ |i\rangle\langle j|, \tag{1.8}$$

for a simple case of only one state per site. Here, $|i\rangle$ is a basis denoting the electronic state localised at position $i = (x, y, z)$ in a cubic lattice of volume $V = L^3$, t_{ij} are nearest-neighbour hopping amplitudes between sites i and j, and ε_i is the i-th site potential energy. In this work, we only consider Hamiltonians that fall under the symmetry class of Gaussian orthogonal ensemble, i.e., the $\mathcal{H}$ has time-reversal and spin-rotational symmetries. The hopping term is set to unity $t = 1$ and disorder is introduced into the model by randomising the values of the site potential energies ε_i. We consider ε_i to have a uniform probability distribution in the interval $[-W/2,\ W/2]$, where W parametrizes the strength of the disorder. Here, the critical disorder is $W_c \approx 16.5$, above which all eigenstates are localised [23–26]. To minimize boundary effects, periodic boundary conditions are used. Due to the universality of the Anderson transition, some of the the critical properties such as the critical exponent will not depend on the details of the Hamiltonian. Hence, a simple tight-binding model for a cubic lattice as just described is able to give the critical properties of the transition.

The $L^3 \times L^3$ Hamiltonian matrix has random values in the diagonal elements which represent the site potential energies. If only nearest neighbor hopping is considered, it is also a sparse matrix with a few off-diagonal elements equal to one. The matrix is diagonalized using the JADAMILU package [27] which is a Jacobi-Davidson implementation with an integrated solver based on the incomplete-LU-factorization package (ILUPACK) [27, 28]. We have considered eigenstates only in the vicinity of the band centre $E = 0$ where the Anderson transition is found

when $W_c \approx 16.5$. We take about five eigenstates in a small energy window around $E = 0$ for any given realizations of disorder. The statistics involved in this work is unprecedented. At the critical point, we have used $\sim 5 \times 10^4$ states for system size $L \leqslant 100$ and ~ 100 states for $L > 100$. The largest system size we have used is $L^3 = 240^3$. In the critical regime, we have taken at least 10000 uncorrelated samples for each size and disorder combination, for a total of $1,530,000$ wave functions.

1.4 Fractal dimension and multifractals

Consider a line segment with unit length $L = 1$. Cover the line with spheres of diameter $l = 1/a$. Other geometrical shapes may be used as well. The least number of spheres that is needed to fully cover the line segment, $N(l)$, is exactly equal to $(L/l)^{D_f}$ where D_f is called the dimension of the support or simply the dimension of a system. Extending this to a square and a cube, we can say that $N(l) \propto l^{-D_f}$. For these three cases of the line segment, square and cube, it is clear to see that $D_f = 1, 2, 3$ respectively. The value of D_f for the above examples is simply equivalent to the Euclidean or topological dimension.

Let us now apply the same procedure to a deterministic fractal such as the Mandelbrot-Given fractal [29] as shown in Fig. 1.4. We consider its initial structure which is composed of eight line segments each with length $L = 1/3$. This fractal structure is being generated by replacing each line segment with the initial structure. For this fractal, $N(l = \frac{1}{3}) = 8$, that is eight spheres with diameter $l = 1/3$ is needed to separately contain each of the eight line segments of the initial structure. If l is reduced then $N(l = (\frac{1}{3})^2) = 8^2$. Recall that $N(l) \propto l^{-D_f}$, hence $D_f = -\ln[N(l)]/\ln[l]$. For the Mandelbrot-Given fractal, the dimension D_f is a non-integer value of $D_f = \log_3 8$ that is less than the Euclidean dimension d. Systems that are defined by one non-integer dimension are called self-similar structures or simply fractals [29–31]. Self-similar because they are scale invariant under isotropic scale

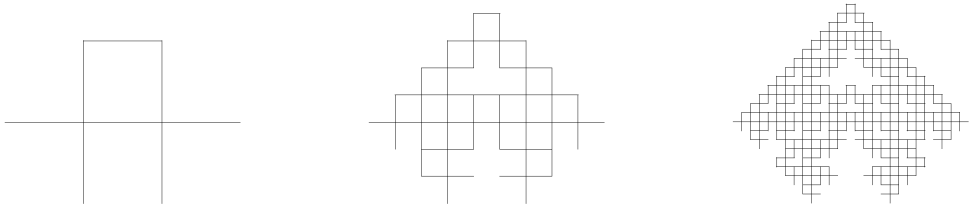

Figure 1.4: The Mandelbrot-Given curve with fractal dimension of $D_f = \log_3 8$. The initial structure shown on the left is composed of eight line segments each with length $L = 1/3$. The higher orders of the fractal structure are generated by replacing each line segment with the initial structure. Courtesy of K.M. Svensson.

transformation which means that the volume of the system increases uniformly in every spatial directions. Fractals occuring in nature are random fractals. Their structure could not be exactly formed by repeated generation of a pattern but in a statistical sense they are self similar.

The dimension that was obtained using the coverage procedure just outlined is called the capacity dimension. The definition of the dimension in terms of the capacity dimension is useful for the purpose of obtaining the corresponding dimension for a system with random distribution of measures, in particular, for multifractals [32, 33]. To illustrate the concept of multifractality, we consider the critical eigenstate $|\Psi\rangle = \sum_{i=1}^{L^d} \psi_i |i\rangle$ of an electron at the metal to insulator transition as shown in Fig. 1.5. Recall that $|i\rangle$ is a basis state at site i with wavefunction amplitude ψ_i and the eigenstate is a superposition of all the orthonormal basis states. This wavefunction corresponds to a three-dimensional cubic lattice of linear length L and volume $V = L^d$. The wavefunction is normalized such that $\sum_{i=1}^{L^d} \psi_i = 1$ and no site has exactly zero ψ_i. This critical state possesses very interesting characteristics. The values of the wavefunction amplitudes greatly fluctuate from site to site. Even more, these large fluctuations in ψ_i appear in all length scales [34–37], i.e., the fluctuations persist even when the scale at which the eigenstate is observed is varied. There are points in the wavefunction containing large values of ψ_i and the existence of sites having very small ψ_i such that the distribution function of ψ_i is

broad. We apply the coverage procedure by dividing the system equally into smaller boxes. One notices that different boxes enclose different substructures or densities. The number of boxes enclosing one similar structure gives one fractal dimension. In fact, a multitude of fractal dimensions is needed to completely characterize the full extent of the complex distribution that defines a system. Systems of this kind are called multifractals because they are made up of different fractal sets. This work probes the multifractal characteristics of the electronic eigenstate at the critical point and in the critical regime of the Anderson metal to insulator transition.

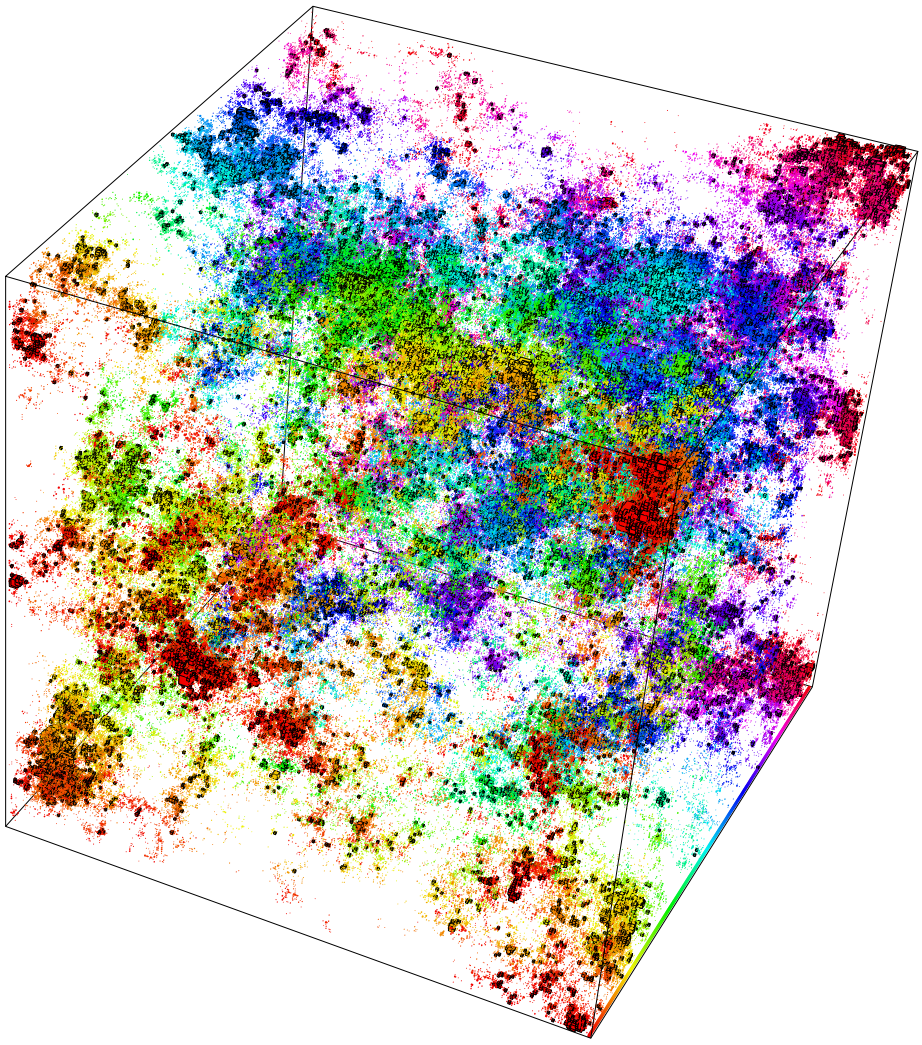

Figure 1.5: Multifractal eigenstate for the 3D Anderson model at $E = 0$ and $W_c = 16.5$ for linear system size L=240 with periodic boundary conditions. The 410075 sites with probability $|\psi_j|^2$ twice larger than the average $1/L^3$ are shown as boxes with volume $|\psi_j|^2 L^3$. The 26097 boxes with $|\psi_j|^2 L^3 > 2\sqrt{1000}$ are plotted with black edges. The color scale distinguishes between different slices of the system along the axis into the page.

Chapter 2

Theory of Multifractal Analysis

2.1 Mass exponents and generalized dimensions

We start by considering the distribution of the normalized wavefunction intensities $|\psi|^2$ in the multifractal electronic state at the critical point of the Anderson metal to insulator transition. Using the usual box counting method [32, 33, 38], we extract the multifractal properties of this wavefunction. Let $|\psi_i|^2$ be the value of the wavefunction intensity at the i-th site in a discretized d-dimensional system with volume L^d. If we cover the system equally with N_l boxes each with linear size l, the probability to find the electron in the k-th box is simply given by

$$\mu_k(l) = \sum_{i=1}^{l^d} |\psi_i|^2, \quad k = 1, \ldots, N_l. \tag{2.1}$$

The box probability $\mu_k(l)$ constitutes the normalized measure $\sum_{\text{all boxes}} \mu_k(l) = 1$. In the limit that $l \to 1$ (i.e., l is equal to the lattice spacing), the box probability reduces to the $|\psi_i|^2$. The sum of the moments of the box probability over all boxes in the volume

$$P_q(l) = \sum_{k=1}^{N_l} \mu_k^q(l), \tag{2.2}$$

is called the generalized inverse-participation ratios (gIPR). The gIPR serve as a q-microscope to effectively probe the fluctuations in $|\psi_i|^2$. The positive q enhances the contribution coming from the large $|\psi_i|^2$ while the negative q is a region where the small $|\psi_i|^2$ dominate. For $q = 2$, the gIPR is simply the usual IPR $P_2 = \sum_i |\psi_i|^4$ which is inversely proportional to the number of sites contributing to a state.

The general assumption underlying multifractality is that within a certain range of values for the ratio $\lambda \equiv l/L$, the moments P_q show a power-law behaviour indicating the absence of length scales in the system, [38]

$$P_q(\lambda) \propto \lambda^{\tau(q)}. \tag{2.3}$$

The exponent $\tau(q)$ is the mass exponent and is defined as

$$\tau(q) = \lim_{\lambda \to 0} \frac{\log\ P_q(\lambda)}{\log\ \lambda}, \tag{2.4}$$

where the limits states that the true value of $\tau(q)$ at criticality is in the thermodynamic limit $\lambda \to 0$. The values for $\tau(q)$ in the limiting cases of weak and strong disorder and at the MIT are

$$\tau(q) = \begin{cases} d(q-1) & \text{for metals,} \\ 0 & \text{for insulators } (q > 0), \\ D_q(q-1) & \text{at the MIT.} \end{cases} \tag{2.5}$$

In an extended metallic state where the wavefunction intensity is uniformly distributed as $|\psi_i|^2 \propto L^{-d}$ and d is the dimension of the support, $\tau(q)$ is a linear function of q with slope $d = 3$ for a $3D$ system. For a strong disorder state where the wavefunction is highly localized within one small spatial region, $P_q = 1$ for all positive q's and hence $\tau = 0$. An indication that a state is multifractal is when $\tau(q)$ is a nonlinear function of q. Generally, $\tau(q)$ is a non-decreasing convex function. The general profile for $\tau(q)$ and the corresponding generalized dimensions D_q are shown

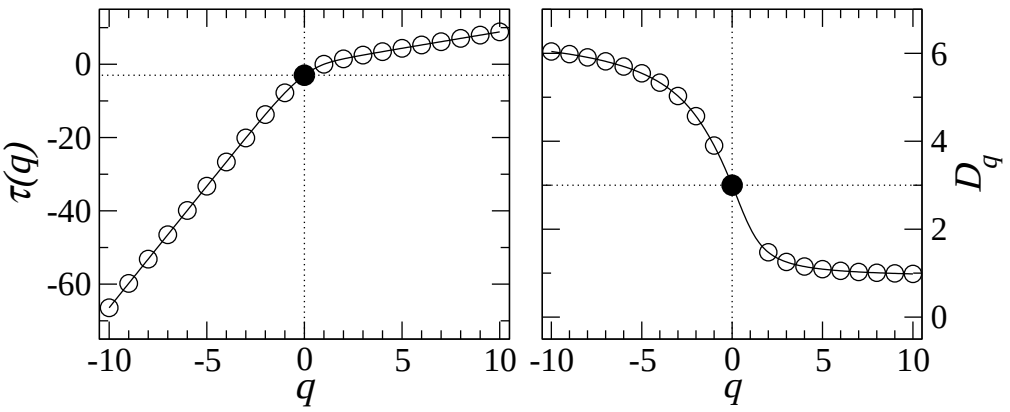

Figure 2.1: Schematic profile of the mass exponents (left) and generalized fractal dimensions (right). The filled black circles correspond to $q = 0$ while the empty circles denote integer q. The thin horizontal and vertical lines indicate the $\tau(0) = -3$, $D_0 = 3$ and $q = 0$ values, respectively.

in Fig. 2.1. At criticality, $\tau(q)$ can also be parametrized as $\tau(q) = d(q-1) + \Delta_q$, where Δ_q are the anomalous scaling exponents characterizing the critical point [39]. Furthermore, from Eqs. (2.2) and (2.3) it is easy to see that $\tau(0) = -d$ and due to the normalization condition $\tau(1) = 0$.

The values of $\tau(q)$ will give the set of generalized dimensions D_q that defines the multifractal system. To show that this is the case, we consider for the present purpose a uniform distribution of $|\psi_i|^2$ on a support with fractal dimension D_f. Using the normalization condition, we can say that the box probability can be expressed as $\mu_k(l) \propto l^{D_f} L^{-D_f}$ since $|\psi_i|^2 \propto L^{-D_f}$ and the number of sites in a box is proportional to l^{D_f}. Take note that the assumption of normal distribution for $|\psi|^2$ allows the relation $|\psi_i|^2 \propto L^{-D_f}$ to be valid for all q and that D_f to be independent of q. The gIPR can then be reformulated as

$$P_q(\lambda) \propto \lambda^{D_f(q-1)}, \tag{2.6}$$

where the summation in Eq. (2.2) is replaced by the number of boxes $N_l = (\frac{L}{l})^{D_f}$. Comparing equations (2.3) and (2.6), we can see that $\tau(q) = D_f(q-1)$. If the

distribution of the measure is not normal such that the fractal dimension depends on q then $\tau(q) = D_q(q-1)$. The set of generalized fractal dimensions is then given as

$$D_q = \frac{1}{q-1} \lim_{\lambda \to 0} \frac{\log\ P_q(\lambda)}{\log\ \lambda}. \tag{2.7}$$

D_q is a monotonically decreasing positive function of q. As with $\tau(q)$, the q-dependence of D_q is an indication of multifractality. For $q = 0$, D_0 is equal to the dimension of the support of the measure. D_1 is equivalent to the information dimension of the system which is in statistical mechanics related to the entropy of the probability distribution of box probabilities $S_\lambda = -\sum_{N_l} \mu_k(\lambda) \log \mu_k(\lambda)$. The generalized dimension corresponding to $q = 2$ is related to the correlation dimension.

2.2 Relation between the mass exponents and singularity spectrum

We shall demonstrate that the mass exponents $\tau(q)$ are related to a set of fractal dimensions called the singularity spectrum $f(\alpha)$ and that they are exactly equivalent such that a multifractal state is completely defined by either one of them. Again, we consider the multifractal distribution of the wavefunction intensities with volume L^d and we divide it into boxes of length l. If we take one box probability μ_1, we will find that its value will have a λ dependence as $\mu_1(\lambda) \sim \lambda^{\alpha_1}$ to some exponent α_1. Another box would scale to another exponent as $\mu_2(\lambda) \sim \lambda^{\alpha_2}$. In fact, different boxes scale to different exponents α. Furthermore, the number of these boxes, $N_{\alpha'}$, corresponding to the same $\alpha = \alpha'$ scales as $N_{\alpha'} \propto \lambda^{-f(\alpha')}$. The set of boxes that scale to the same $\alpha = \alpha'$ is a fractal with a fractal dimension of $f(\alpha')$. A multifractal state such as the electronic state at the MIT is completely defined by an infinite set of $f(\alpha)$ values which is called the singularity spectrum.

The ensemble (arithmetic) average of the generalized inverse participation ratios in terms of the probability density function (PDF) of the box probability

$\mathcal{P}(\mu_k)$ is given by

$$\langle P_q \rangle \equiv \lambda^{-d} \langle \mu_k^q(\lambda) \rangle = \lambda^{-d} \int_0^1 \mathcal{P}(\mu_k)\ \mu_k^q(\lambda)\ \mathrm{d}\mu_k, \tag{2.8}$$

where the average is over all disorder realizations and over the lattice volume L^d. The normalization of $\mu_k(\lambda)$ gives the limits of the integration. We make a change of variables, $\mathcal{P}(\mu_k)\mathrm{d}\mu_k = \mathcal{P}(\alpha)\mathrm{d}\alpha$. In terms of α, we parametrize the box probability to be $\mu_k(\lambda) \equiv \lambda^\alpha$ and its logarithmic form is $\alpha \equiv \ln \mu_k / \ln \lambda$. When $l = 1$, the box probability reduces to the wavefunction intensity that is given by $|\psi_i|^2 \equiv L^{-\alpha}$. Furthermore, $\mu_k^q(\lambda) = \lambda^{\ln_\lambda \mu_k^q} = \lambda^{q \frac{\ln \mu_k}{\ln \lambda}}$. Equation (2.8) becomes

$$\lambda^{-d} \langle \mu_k^q(\lambda) \rangle = \lambda^{-d} \int_0^\infty \mathcal{P}(\alpha)\ \lambda^{q\alpha}\ \mathrm{d}\alpha. \tag{2.9}$$

In terms of the PDF $\mathcal{P}(\alpha)$, the number of boxes having the same values of $\mu_k = \lambda^\alpha$ is $N_\alpha = \mathcal{P}(\alpha)\mathrm{d}\alpha \cdot \lambda^{-d} \propto \lambda^{-f(\alpha)}$. Hence, using $\mathcal{P}(\alpha) \propto \lambda^{d-f(\alpha)}$ into Eq. (2.9) we have

$$\begin{aligned} \lambda^{-d} \langle \mu_k^q(\lambda) \rangle &\propto \int_0^\infty \lambda^{q\alpha - f(\alpha)}\ \mathrm{d}\alpha \\ &\propto \int_0^\infty e^{\ln \lambda \cdot \tilde{F}(\alpha)}\ \mathrm{d}\alpha, \end{aligned} \tag{2.10}$$

where $\tilde{F}(\alpha) = q\alpha - f(\alpha)$. We evaluate the above integral using the saddle-point method which is justified in the limit of large L or small λ. The saddle-point method requires that the function $\tilde{F}(\alpha)$ must have a unique global maximum at some $\alpha = \tilde{\alpha}$, i.e, $\tilde{F}''(\tilde{\alpha}) < 0$, and that $\tilde{\alpha}$ is not an end point in the integration interval. Solving the integral of Eq. (2.10) reproduces the scaling relation in (2.3) and gives the following relations

$$q = f'(\tilde{\alpha}), \tag{2.11}$$

$$\tau(q) = q\tilde{\alpha} - f(\tilde{\alpha}), \qquad f(\tilde{\alpha}) = q\tilde{\alpha} - \tau(q). \tag{2.12}$$

Furthermore using Eq. (2.12) into Eq. (2.11), we will obtain

$$q = q + \tilde{\alpha}\frac{\mathrm{d}q}{\mathrm{d}\alpha} - \frac{\mathrm{d}\tau}{\mathrm{d}q}\frac{\mathrm{d}q}{\mathrm{d}\alpha}, \tag{2.13}$$

which gives the values of the singularity strength or the Lipschitz-Hölder exponent to be

$$\tilde{\alpha}_q = \frac{\mathrm{d}\tau(q)}{\mathrm{d}q}. \tag{2.14}$$

Equations (2.11) to (2.14) state that $f(\alpha)$ is just the Legendre transformation of $\tau(q)$. Furthermore, since $q = f'(\tilde{\alpha})$ then the maximum of the singularity spectrum can exactly be found at $q = 0$.

The singularity spectrum $f(\alpha)$ is a convex function of α. A pictorial sketch of the properties of $f(\alpha)$ is shown in Fig. 2.2. Due to the normalization condition of $|\psi_i|^2$, $f(\alpha)$ is only defined on a semi-axis $\alpha \geq 0$. It has its maximum at $\alpha_0 \geqslant d$ where $f(\alpha_0) = d$. Since nowhere in the wavefunction will $|\psi_i|^2 = 0$, d is simply the topological dimension. As previously shown, α_0 corresponds exactly to the moment $q = 0$ evaluation of the gIPR. To the right of α_0 is the region of negative q's where the contributions coming from small wavefunction intensities $|\psi_i|^2 < L^{-d}$ are dominant. The left region at $\alpha < \alpha_0$ of the singularity spectrum is the positive q's area that is being populated by large $|\psi_i|^2 > L^{-d}$. For α_1 that corresponds to $\tau(1) = 0$, we have $f(\alpha_1) = \alpha_1$ and $f'(\alpha_1) = 1$. In the limit of vanishing disorder the singularity spectrum becomes narrower and eventually converges to one point $f(d) = d$. On the other hand, as the value of disorder increases the singularity spectrum broadens and in the limit of strong localisation the singularity spectrum tends to converge to the points: $f(0) = 0$ and $f(\infty) = d$. Only at the MIT we can have a true multifractal behaviour and as a consequence the singularity spectrum must be independent of all length scales, such as the system size.

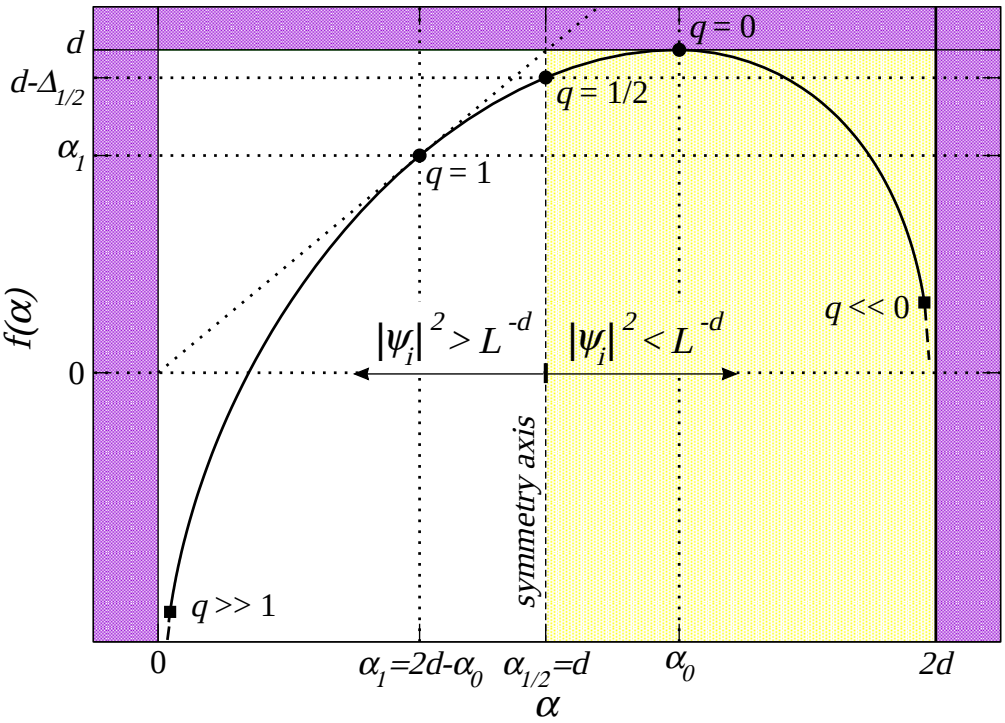

Figure 2.2: Pictorial representation of the general features of the multifractal spectrum at criticality. The dotted purple areas highlight forbidden regions for $f(\alpha)$. Each point on the spectrum corresponds exactly to an evaluation of a q-moment of the gIPR. The maximum is found at the point $q = 0$ where $f(\alpha_0) = d$. At $q = 1$, $f(\alpha_1) = \alpha_1$ and $f'(\alpha_1) = 1$. The two regions to the right and left of $q = 1/2$ are determined by different wavefunction amplitudes, $|\psi_i|^2 > L^{-d}$ (white) and $|\psi_i|^2 < L^{-d}$ (yellow). The symmetry axis at $q = 1/2$ is highlighted and here $f(\alpha_{1/2} = d) = d - \Delta_{1/2}$. The yellow shaded area can be connected to the white area via the symmetry relation (2.20),(2.21), and vice versa. The points corresponding to $q = 0$ and $q = 1$ are symmetry related points.

2.3 Parabolic approximations to the $f(\alpha)$

From an analytical viewpoint not much is known about how the singularity spectrum should look like at criticality. However, an approximate expression for the $f(\alpha)$ has been put forward that is valid in the regime of weak multifractality, i.e. when the critical point is close to a metallic behaviour. This applies to the Anderson transition in $d = 2 + \epsilon$ dimensions with $\epsilon \ll 1$. In this case a parabolic dependence of the

singularity spectrum is found to be [40]

$$f(\alpha) \simeq d - \frac{[\alpha - (d+\epsilon)]^2}{4\epsilon}. \tag{2.15}$$

Equation (2.15) implies a corresponding approximation for the anomalous dimensions as given by $\Delta_q \simeq -\epsilon q(q-1)$. For the case of $d = 2+1$, we have $f(\alpha) = d - (\alpha - \alpha_0)^2/4$. This parabolic approximation for the $f(\alpha)$, apart from the dimension of the support d, only depends on one parameter α_0 that is exactly $\alpha_0 = 4$ for $d = 2+1$ case and that defines the position of the maximum $f(\alpha_0) = d$. Generally, equation (2.15) provides a very good approximation to the critical $f(\alpha)$ near $\alpha = \alpha_0$ and deviates from the true $f(\alpha)$ at α values far away from α_0. Due to the normalization condition of the wavefunction intensities, we have to impose the condition $\alpha \geqslant 0$ to Eq. (2.15). In the limit of $\alpha = 0$ such that $\alpha = \frac{\mathrm{d}\tau(q)}{\mathrm{d}q} = 0$, the mass exponent $\tau(q)$ should approach a constant value as $q \to q_c$ where critical q_c corresponds to $\alpha_{q_c} = 0$. Therefore, the parabolic $f(\alpha)$ should terminate at $\alpha = 0$ with a finite value. This behaviour is known as the termination of the multifractal spectrum. Whether the $f(\alpha)$ at $\alpha = 0$ terminates or continues to negative infinity will be further discussed later on. Although the parabolic approximation has turned out to be exact for some models [41] its validity, in particular for the integer quantum Hall transition, is currently under an intense debate [42] due to the implications that this result has upon the critical theories describing the transition.

2.4 Symmetry relations in the multifractal exponents at the Anderson transition

Recently, the existence of exact symmetry relations in the multifractal exponents of the Anderson transition has been reported [43]. The mass exponents that describe the scaling of the generalized inverse participation ratio in Eq. (2.3) can be defined

at criticality to be $\tau(q) = d(q-1) + \Delta_q$. The anomalous exponents Δ_q separate the critical point from the metallic phase for which $\Delta_q = 0$. Furthermore, Δ_q determine the scale dependence of the moments of the local density of states (LDOS) ρ^q [39] that is expressed as

$$\langle \rho^q \rangle \propto L^{-\Delta_q}. \tag{2.16}$$

Previous works have suggested a symmetry relation in the distribution function of LDOS $\mathcal{P}_\rho(\tilde{\rho})$ as given by [44–46]

$$\mathcal{P}_\rho(\tilde{\rho}) = \tilde{\rho}^{-3} \mathcal{P}_\rho(\tilde{\rho}^{-1}), \tag{2.17}$$

where $\tilde{\rho} = \rho/\langle \rho \rangle$ is the normalized LDOS. Since $\langle \tilde{\rho}^q \rangle = \int \mathrm{d}\tilde{\rho}\ \tilde{\rho}^q\ \mathcal{P}_\rho(\tilde{\rho})$, Eq. (2.17) implies the relation $\langle \tilde{\rho}^q \rangle = \langle \tilde{\rho}^{1-q} \rangle$ which from Eq. (2.16) in turn gives

$$\Delta_q = \Delta_{1-q}. \tag{2.18}$$

Equation (2.17) has been derived using a supersymmetric nonlinear σ model [44] that is able to approximately model the critical properties of the Anderson transition for the case of weak disorder but breaks down for strong disorder. It has been argued that although the mapping of the Anderson model onto the nonlinear σ model is not exact, there exist several microscopic models (e.g., N-orbital Wegner model for $N \to \infty$) for the Anderson transition that can be reduced exactly to the nonlinear σ model. The universality of the critical exponents permits the validity of the symmetry relation (2.18) in the multifractal exponent Δ_q on any microscopic model of criticality.

In terms of the mass exponents and $\tau(1-q) = d(1-q-1) + \Delta_{1-q}$, Eq. (2.18) can also be written as

$$\tau(q) - \tau(1-q) = d(2q-1). \tag{2.19}$$

Equations (2.18) and (2.19) reveal the existence of the symmetry axis at $q = 1/2$ as

clearly marked in Fig. 2.2. Furthermore, expressing $\tau(q)$ in its Legendre transform of $f(\alpha_q = \frac{\mathrm{d}\tau_q}{\mathrm{d}q})$ and since $-\alpha_{1-q} = \frac{\mathrm{d}\tau_{1-q}}{\mathrm{d}(1-q)}\frac{\mathrm{d}(1-q)}{\mathrm{d}q}$, the corresponding symmetry relations are given by

$$\alpha_q + \alpha_{1-q} = 2d, \tag{2.20}$$

$$f(2d - \alpha) = f(\alpha) + d - \alpha. \tag{2.21}$$

Equation (2.21) follows from using the relations (2.19) and (2.20) into the definition of $f(\alpha_{1-q}) = (1-q)\alpha_{1-q} - \tau_{1-q}$. In Fig. 2.2, we highlight the symmetry points and relations in the critical multifractal spectrum.

We shall look at the implications of these symmetry relations on the multifractal spectrum. The wave function normalization condition gives the lower bound $\alpha_{\min} = 0$ for the singularity strength and requires that α is always positive. It readily follows from the symmetry in (2.20) that in the limit of $\alpha_{q\to+\infty}$ then $\alpha_{q\to+\infty} + \alpha_{q\to-\infty} = 2d$ which means that α should only be contained in the interval $[0, 2d]$. If $\alpha_{q\to+\infty} = 0$ then the upper bound is $\alpha \leqslant 2d$. Furthermore, the symmetry relation in the singularity spectrum $f(\alpha)$ states that $0 \leqslant \alpha \leqslant d$ and $d \leqslant \alpha \leqslant 2d$ regions of the singularity spectrum must be related by the relation (2.21). In other words, using (2.21) one can be mapped onto another. The symmetry axis $\alpha = d$ is exactly equivalent to $q = \frac{1}{2}$. However, in the presence of a termination point at $\alpha = 0$ the validity of the symmetry relation is not yet clear [39].

Numerical calculations have since then supported this symmetry in $f(\alpha)$ in the one-dimensional power-law random-banded-matrix model [43] and the two-dimensional Anderson transition in the spin-orbit symmetry class [47] and SU2 model [48]. Recent experimental work on the multifractal analysis of vibrations in elastic networks have successfully shown the existence of the symmetry [7]. In the present work we numerically verify that this symmetry in the singularity spectrum also holds in the three-dimensional (3D) Anderson model. In order to address this hypothesis with sufficient accuracy, we have considered the box- and system-size

scaling of the typical and ensemble averages of P_q in computing the $f(\alpha)$. We discuss which numerical strategy will produce the best possible agreement with the symmetry and we highlight the statistical analysis that must be used to observe the reported symmetries with sufficient confidence.

Chapter 3

Multifractal Analysis with Typical Averaging

The numerical analysis is essentially based on an *averaged* form of the scaling law for the gIPR (2.3) in the limit $\lambda \equiv l/L \to 0$. The limit can be achieved either by making the box size $l \to 0$ for a fixed system size L, or by considering $L \to \infty$ for a fixed box-size. The question of how to compute a proper average of the moments P_q is determined by the form of their distribution function [49, 50]. The scaling law for the typical average of the moments P_q is defined as

$$e^{\langle \ln P_q(\lambda) \rangle} \propto \lambda^{\tau^{\rm typ}(q)}, \tag{3.1}$$

where $\langle \cdots \rangle$ denotes the arithmetic average over all realizations of disorder, i.e. over all different wavefunctions at criticality. The mass exponents are then defined by

$$\tau^{\rm typ}(q) = \lim_{\lambda \to 0} \frac{\langle \ln P_q(\lambda) \rangle}{\ln \lambda}, \tag{3.2}$$

and can be obtained from the slope of the linear fit of $\langle \ln P_q \rangle$ versus $\ln \lambda$. Applying Legendre transformation we obtain similar definitions for α and $f(\alpha)$,

$$\alpha_q^{\mathrm{typ}} = \lim_{\lambda \to 0} \frac{1}{\ln \lambda} \left\langle \sum_{k=1}^{N_\lambda} \delta_k(q,\lambda) \ln \delta_k(1,\lambda) \right\rangle, \tag{3.3a}$$

$$f_q^{\mathrm{typ}} = \lim_{\lambda \to 0} \frac{1}{\ln \lambda} \left\langle \sum_{k=1}^{N_\lambda} \delta_k(q,\lambda) \ln \delta_k(q,\lambda) \right\rangle, \tag{3.3b}$$

where $\delta_k(q,\lambda) \equiv \mu_k^q(\lambda)/P_q(\lambda)$ is the normalized q-th power of the integrated probability distribution $\mu_k(\lambda)$. Note that, for varying l and L, $\mu_k(\lambda)$ values depend on the ratio $\lambda = l/L$. The singularity spectrum could also be obtained from $\tau(q)$ by means of the numerical Legendre transformation which involves a differentiation process, but this latter method is numerically less stable.

The typical average is dominated by the behaviour of a single (representative) wavefunction. It is because of this that the $f^{\mathrm{typ}}(\alpha)$ will usually only have positive values, since the average number of points in a single wavefunction with a singularity $\bar{\alpha}$ such that $f(\bar{\alpha}) < 0$ is $L^{-|f(\bar{\alpha})|} \ll 1$. It is also worth mentioning that due to the relations (2.11) and (2.14), the typical singularity spectrum is expected to approach the abscissa axis with an infinite slope. However, it has been proven numerically, that the region of α values near the ends where the slope tends to diverge gets narrower and eventually disappears as the thermodynamic limit is approached [51, 52]. A list of the number of states and the size of ψ_i used for each L is given in Table 3.1.

3.1 Scaling with box size

In the scaling law of Eq. (2.3), the limit $\lambda \to 0$ can be reached by taking the box size $l \to 0$, i.e., we are evaluating the scaling of P_q with box size l at constant L. Numerically, we consider a system with large L and we partition it into smaller boxes such that condition $l_m \ll l < L$ is fulfilled with l_m the lattice spacing. This

Table 3.1: The linear system size L, corresponding volume V and the number of samples taken and correspondingly the total number of wavefunction amplitudes ψ_i evaluated. All eigenstates are at the critical MIT for which $W_c = 16.5$ and correspond to the five eigenvalues closest to the band center. The diagonalization of the matrix was computed on an SGI Altix 3700BX2 where for $L = 240$ it took approximately 24 hours and requires ∼24GB of memory to obtain five eigenstates for one disorder realization.

L	$V = L^3$	samples	ψ_i
20	8×10^3	24 995	2×10^8
30	9×10^3	25 025	6.8×10^8
40	6.4×10^4	25 025	1.6×10^9
50	1.3×10^5	25 030	3.1×10^9
60	2.2×10^5	25 030	5.4×10^9
70	3.4×10^5	24 950	8.6×10^9
80	5.1×10^5	25 003	1.3×10^{10}
90	7.3×10^5	25 005	1.8×10^{10}
100	1×10^6	25 030	2.5×10^{10}
140	2.7×10^6	105	2.9×10^8
160	4.1×10^6	125	5.1×10^8
180	5.8×10^6	100	5.8×10^8
200	8×10^6	100	8×10^8
210	9.3×10^6	105	9.7×10^8
240	1.4×10^7	95	1.3×10^9

ensures that the multifractal fluctuations of $|\psi|^2$ will be properly measured. We usually take values of the box size in the range $l \in [10, L/2]$. We have found that the most adequate box-partitioning scheme is when the system is divided into *integer* number of *cubic* boxes, each box with linear size l [53]. The system is partitioned in such a way that it can be divided equally into boxes and the origin of the first box coincides with the origin $(x, y, z) = (0, 0, 0)$ of the system. We have used this method to produce all the results in this section. We have also tried other box-partitioning strategies, however, their results were less accurate and will be discussed in chapter 5.

For each wave function, we compute for the q-th moment of the box probability in each box, and P_q as in (2.2), as its sum from all the boxes. The scaling

behaviour of the averaged gIPR with box size (3.1) is then obtained by varying l. Finally, the corresponding values of the singularity strength α and spectrum $f(\alpha)$ are derived from the linear fits of the Eqs. (3.3) in terms of the box size. With only one system size to be considered, the box-size scaling is numerically relatively inexpensive and has been much used previously in performing a MFA [36,54,55]. In Figs. 3.1 and 3.2 we show examples of $f(\alpha)$ and associated linear fits. We note that here and in the following, all data have been generated using $q \in [-10, 10]$ in steps of 0.1.

3.1.1 General features of $f^{\mathrm{typ}}(\alpha)$

The singularity spectrum for system size $L = 240$ with 95 states that is obtained using Eqs. (3.3) with $l \to 0$ is shown in Fig. 3.1. The f^{typ} is compared with the corresponding spectrum that is derived from the symmetry relation (2.21) and with the parabolic spectrum [40]. Here, the maximum $f^{\mathrm{typ}}(\alpha_0) = 3$ which is equal to the dimension of the support can be found very near to $\alpha_0 = 4$ where the maximum of the parabolic spectrum is located at [40]. In the region within the vicinity of $\alpha = 3$, the typical singularity spectrum closely resembles the parabolic $f(\alpha)$. However, for large $|q|$ values particularly at the tails, the $f^{\mathrm{typ}}(\alpha)$ starts to deviate from the parabolic spectrum. We note that the symmetry relation (2.21) requires that the spectrum should be contained below the upper bound of $\alpha = 2d$.

In order to obtain α and $f(\alpha)$ via the linear fit of Eqs. (3.3), a general χ^2 minimization is considered taking into account the statistical uncertainty of the averaged right-hand side terms. In this way we can carry out a complete analysis of the goodness of the fits via the quality-of-fit parameter Q, as well as the usual linear correlation coefficient r^2. The behaviour of these quantities for the different parts of the spectrum (corresponding to different values of the moments q) is shown in the bottom panel of Fig. 3.1. The r^2 value is almost equal to one for all α which shows the near perfect linear behaviour of the data. Furthermore, acceptable

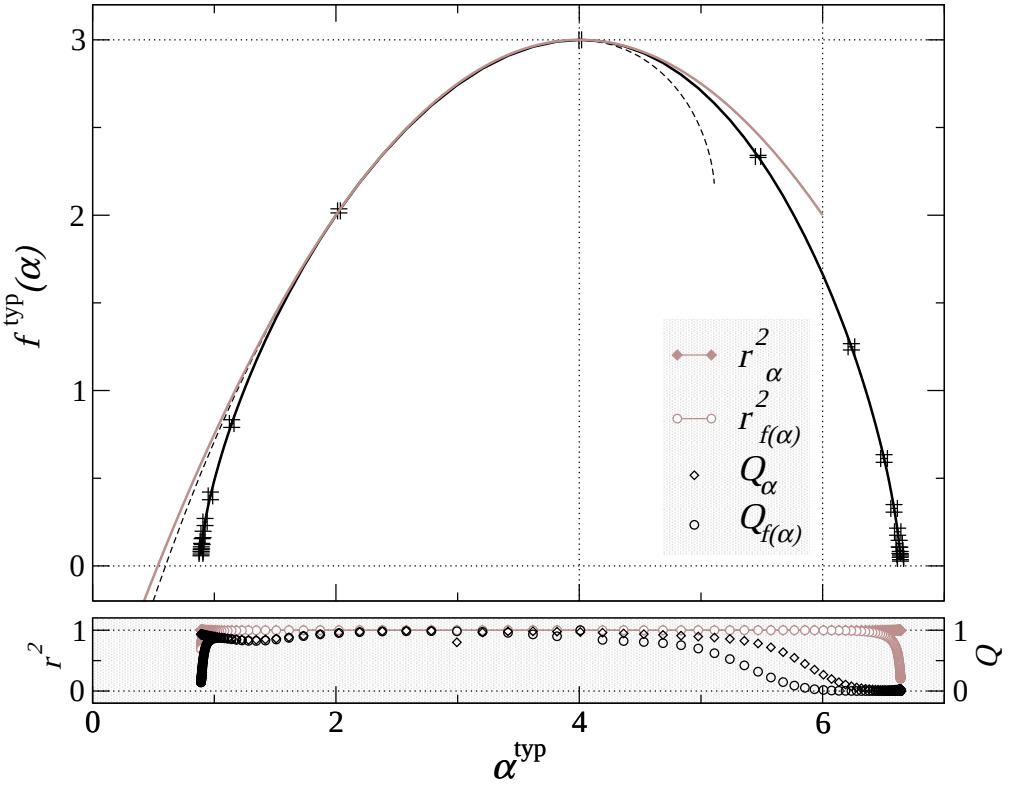

Figure 3.1: Singularity spectrum (thick solid black line) obtained using box-size scaling of the typical average of P_q for system size $L = 240$ with 95 states. The error bars which are equal to one standard deviation mark the locations corresponding to integer q values. The corresponding symmetry-transformed spectrum (2.21) is shown as thin black dashed line. The analytical parabolic form (2.15) is represented by the thick gray solid line. The thin horizontal and vertical lines denote the $f = 0$, $f = 3$ and $\alpha = 4$, $\alpha = 6$ values, respectively. The values for the linear correlation coefficient r^2 and quality-of-fit parameter Q for both α^{typ} and $f^{\mathrm{typ}}(\alpha)$ are shown in the bottom shaded panel. Note that unless otherwise specified in the $f(\alpha)$ plot, the solid lines are not fits but represent actual data points for all values of $q \in [-10, 10]$ in steps of 0.1. Furthermore, only data points corresponding to integer q are marked by symbols.

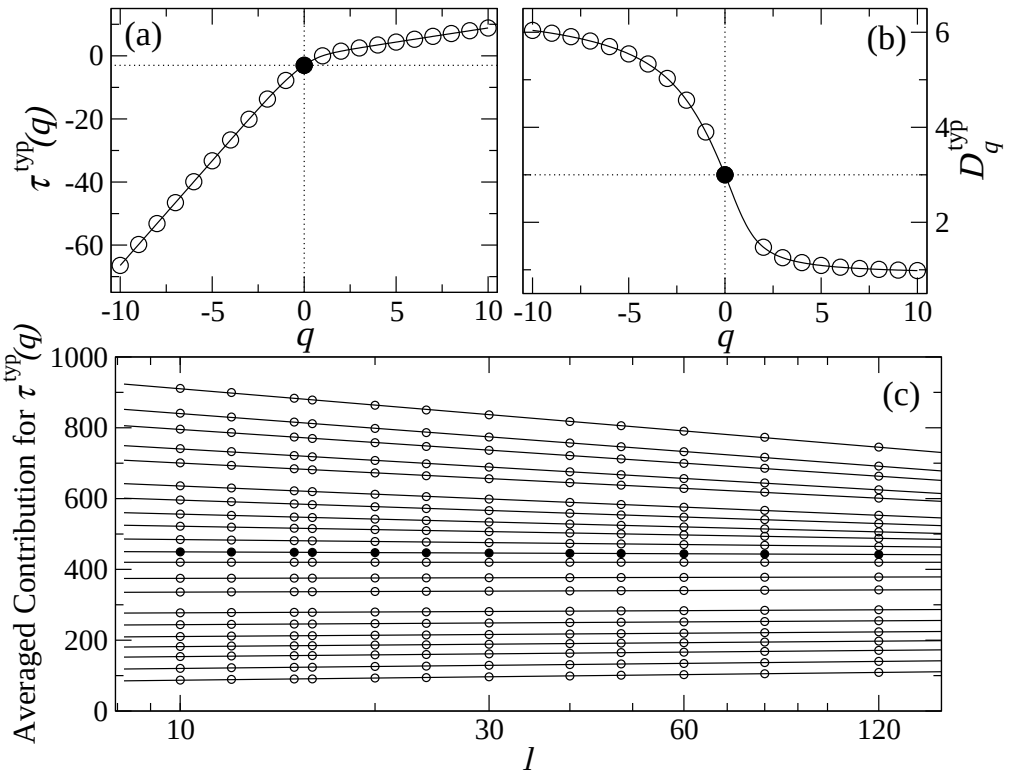

Figure 3.2: Mass exponents (a) and generalized fractal dimensions (b) obtained using box-size scaling of the typical average of P_q for $L = 240$ considering 95 states. The filled black circles correspond to $q = 0$ while the empty circles denote integer q. The thin horizontal and vertical lines indicate the $\tau(0) = -3$, $D_0 = 3$ and $q = 0$ values, respectively. In panel (c), we show the linear fits of Eq. (3.2) for the $\tau^{\rm typ}(q)$ in panel (a). Only fits for integer values of q ranging from $q = -10$ (top) to $q = 10$ (bottom) are shown. The values of $\tau^{\rm typ}(q)$ are given by the slopes of the fits. Data points for $q \neq 0$ have been properly shifted vertically to ensure optimal visualization. Data for $q = 0$ is highlighted with filled symbols. Standard deviations of all data are contained within symbol size in all cases.

values of the Q parameter are also obtained. However, a decline in the r^2 and Q values is seen at the tails. These regions correspond to the large $|q|$ values where the numerical uncertainties in computing for the P_q over a number of different disorder realizations are large enough to affect the reliability of the data. Figure 3.2 presents the corresponding sets of mass exponents $\tau^{\rm typ}(q)$, generalized fractal dimensions $D_q^{\rm typ}$ and linear fits for $\tau^{\rm typ}(q)$ for the singularity spectrum in Fig. 3.1. The q-dependence of the decreasing function $D_q \equiv \tau(q)/(q-1)$ is an indication of multifractality. Here, we see that $D_0 = d$ as expected. The corresponding $\tau^{\rm typ}(q)$ is shown in Fig. 3.2(a). It displays the characteristic nonlinearity of a multifractal where $\tau(0) = -d$. The regions corresponding to large $|q|$ values show a linear behaviour with a constant slope. Since the singularity strength is defined as $\alpha_q = \tau'(q)$ then a linearity in $\tau^{\rm typ}(q)$ found in the limit of $|q| \to \infty$ results in $\alpha_q^{\rm typ}$ values that approach upper α_+ and lower α_- bounds. Hence, the $f^{\rm typ}(\alpha)$ meets the $\alpha^{\rm typ}$ axis at these termination points with an infinite slope [52]. Furthermore, we will show that the location of α_- and α_+ is greatly affected by system size. For a detailed discussion on the relationship between the shapes of $\tau(q)$ and $f(\alpha)$, we refer to the references [39] and [51].

3.1.2 Effects of the number of states and L on $f^{\rm typ}(\alpha)$

In panel (a) of Fig. 3.3, we show the small-α region of $f^{\rm typ}(\alpha)$ for the case of $L = 90$ with 2.5×10^2 and 2.5×10^4 states. When more states are considered for a fixed system size, the symmetry relation is more closely satisfied. We also see the tendency that the termination point α_- moves further towards smaller values with more states. This tendency is possible because the distribution for the generalized inverse participation ratios P_q which give the values for α_q has a long tail and is not symmetric. A study near the tail of the $f(\alpha)$ is a region where the influence of low-probability events or rare eigenfunctions becomes more significant. As we increase the number of states, the number of these rare events also increases and

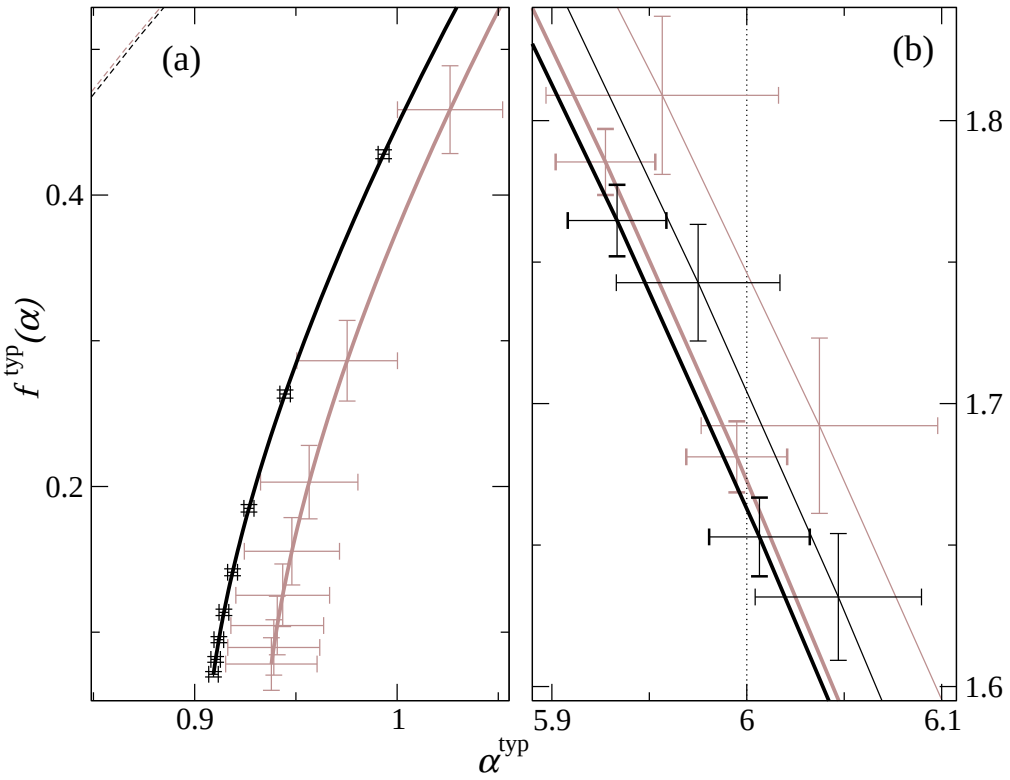

Figure 3.3: Singularity spectrum obtained using box-size scaling of the typical average of P_q. In panel (a): system size $L = 90$ for 250 (thick gray line) and 2.5×10^4 (thick black lines) states. The corresponding symmetry-transformed spectra (2.21) are shown as thin dashed lines. The error bars mark the location of integer q values. In panel (b): system size $L = 60$ (thick gray line), $L = 100$ (thin gray line), $L = 200$ (thin black line) and $L = 240$ (thick black line) each having 10^3, 10^2, 10^2 and 95 states respectively. The dashed vertical line indicates $\alpha = 6$. In all cases, the error bars denote one standard deviation.

therefore although its influence under typical averaging is subtle, it manifests itself as a slow shift in the tail of the spectrum. However, when a large number of states has already been considered (such as 2.5×10^4 for $L = 90$) the shape of the $f^{\mathrm{typ}}(\alpha)$ will not significantly change anymore with more states as illustrated by the already small uncertainties. This takes us to consider bigger system sizes in order to be able to improve the symmetry relation. In panel (b) of Fig. 3.3, we show a portion of the large-α part of $f^{\mathrm{typ}}(\alpha)$ for varying system sizes $L = 60$ with 10^3 states, $L = 100$ and $L = 200$ with 10^2 states each, and $L = 240$ with 95 states. We see that for

the same number of states the degree of fluctuations as represented by the size of the error bars is larger for smaller system size. Moreover, the $f^{\rm typ}(\alpha)$ for $L = 60$ with 10^3 states is, within the standard deviations, the same as that for $L = 240$ with 95 states. This can be explained by the total number of wavefunction values ψ_i involved in the average, which are nearly the same for both cases and hence causes the same shape of $f^{\rm typ}(\alpha)$. This means that when using box-size scaling for the typical average of P_q, the number of disorder realizations needed to obtain the singularity spectrum up to a given degree of reliability decreases with the size of the system. Remarkably, we also see in Fig. 3.3(b) a general tendency that with larger L the singularity spectrum approaches the upper bound of $\alpha = 6$ in keeping with what the symmetry relation requires.

In Fig. 3.4, we show the spectra corresponding to $L = 60$ with 2.5×10^4 and $L = 240$ with 95 states to clearly show the effect of the system size. We observe that the value of α_0 (i.e., location of the maximum) and the shape of the singularity spectrum near the maximum do not change anymore with L. This L-invariant behaviour of the singularity spectrum is an attribute of a critical point. In inset (a), with increasing system size the position of the termination point α_- moves towards smaller values. Furthermore, a closer look of $f^{\rm typ}(\alpha)$ in insets (a) and (b) shows that when a bigger system size is used, even with less eigenstates, there is a well defined improvement to satisfying the symmetry.

3.1.3 Symmetry relation

In order to quantify how the symmetry is being satisfied with regards to either taking more states or considering bigger system size, we present Fig. 3.5. The top panel is an exact calculation of the symmetry relation of Eq. (2.20) whereas the bottom panel shows the difference between the singularity spectrum and its

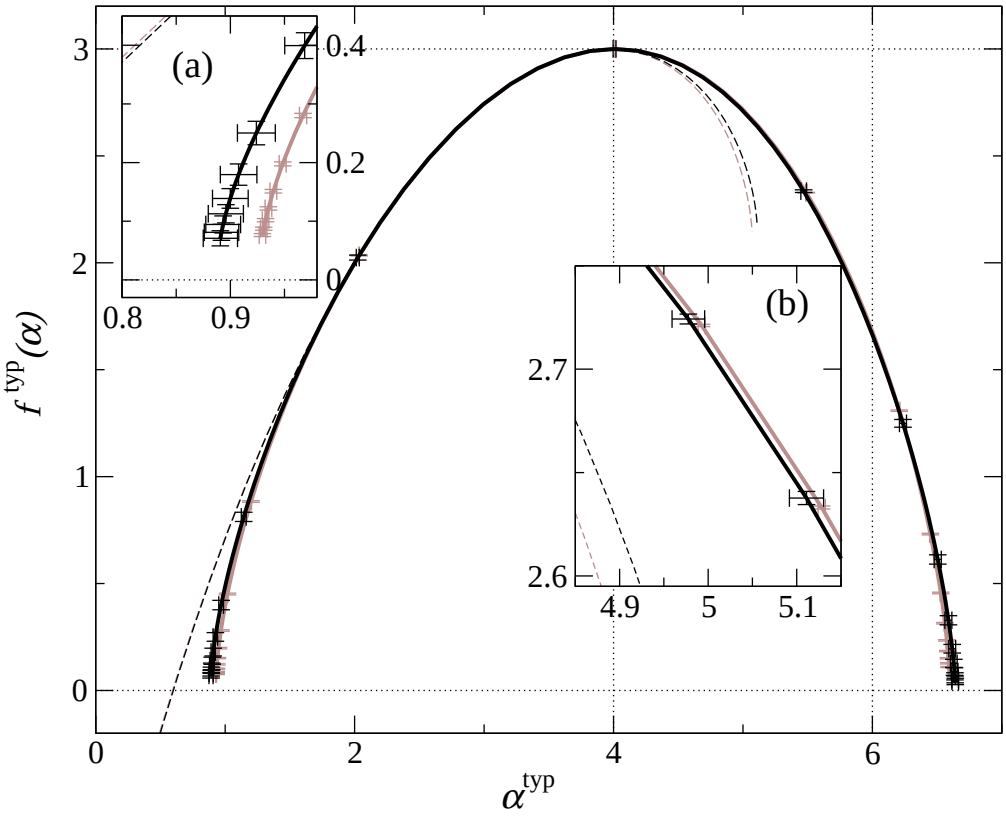

Figure 3.4: Singularity spectrum obtained using box-size scaling of the typical average of P_q, for system sizes $L = 60$ (thick gray line) and $L = 240$ (thick black line) with 2.5×10^4 and 95 states respectively. The corresponding symmetry-transformed spectra (2.21) are shown as thin dashed lines. The insets show details for (a) small and (b) large α values. In all cases, the error bars are equal to one standard deviation. In inset (a), the error bars mark the location corresponding to integer q values.

symmetry-transformed counterpart, defined as

$$\delta f(\alpha) \equiv |f(\alpha) - f(2d - \alpha) + d - \alpha|. \tag{3.4}$$

The latter plot is an effective tool to tell us the range of the α values where the symmetry is satisfied up to a given tolerance. However, directly comparing the degree of symmetry via $\delta f(\alpha)$ is just an approximation since (i) linear interpolation has to be used to measure the vertical distance properly at several values of α, and (ii) for a given q the corresponding value of α as well as its uncertainty depend upon

sizes and realizations of disorder, and this makes the comparison of the different curves in terms of α not as reliable as Eq. (2.20). In fact, the resulting error bars are much larger than in the top panel of Fig. 3.5 and even larger than the variation between the 3 shown $\delta f(\alpha)$ curves. Nevertheless, the results in Fig. 3.5 illustrate that there is a tendency to find a better agreement with the symmetry relation whenever more states or bigger system sizes are considered. The best situation corresponds to the biggest system size available ($L = 240$) even though the number of eigenstates is lower than for smaller systems. The relatively weak effect of the number of states on the shape of the singularity spectrum is a result of taking the typical average where by nature the average does not dramatically change with the number of samples taken. Furthermore, a rough estimation from our results suggest that in order to obtain numerically a good $f(\alpha)$ symmetry relation ($\delta f(\alpha) \leqslant 0.01$) for $\alpha \in [1.5, 4.5]$ using box-size scaling one would have to consider very big system sizes $L \gg 1000$.

3.2 Scaling with system size

The scaling law of the gIPR (2.3) can also be studied in terms of the system size L. Obviously the numerical calculation of eigenstates for very large 3D systems is a demanding task [28, 56–58]. Hence previous MFA studies at the MIT have been mostly based on the box-partitioning scaling described in Sec. 3.1. One naturally would expect the scaling with the system size to perform better in revealing the properties of the system in the thermodynamic limit. The fact that for each system size one has several independent realizations of the disorder helps reduce finite-size effects, which will be unavoidably more pronounced when doing scaling with the box size. Obviously the larger the system sizes and the more realizations of the disorder, the better.

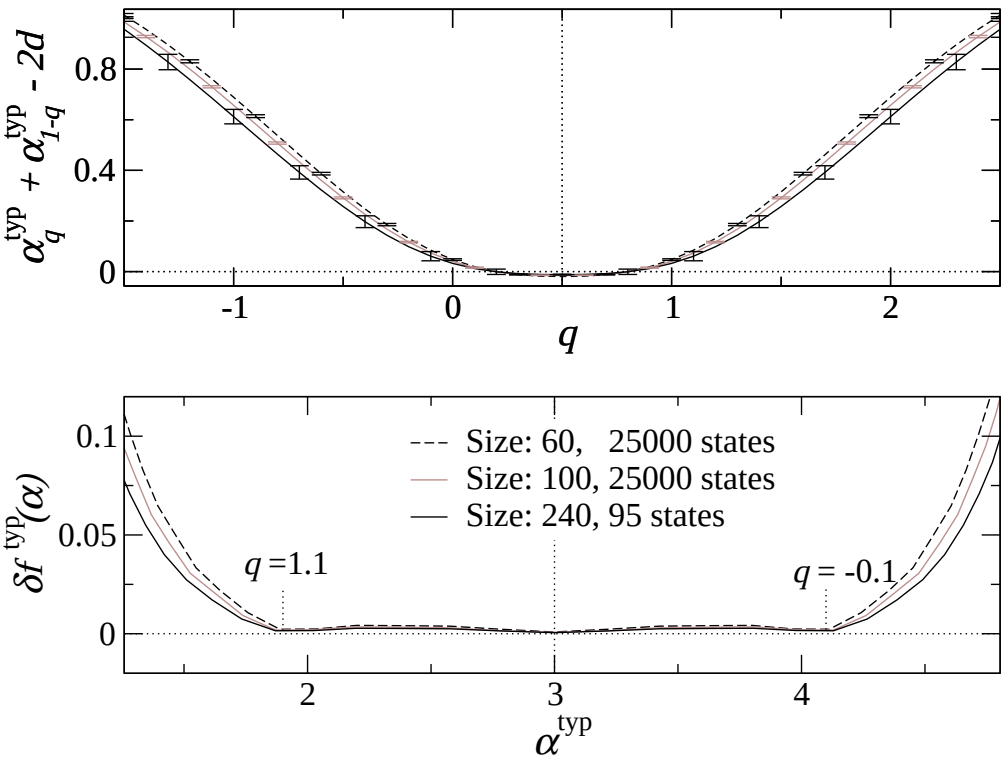

Figure 3.5: Measures for the degree of symmetry of the multifractal spectrum obtained from the typical average with box-size scaling. The upper panel shows the numerical evaluation of the symmetry law as a function of q for system sizes $L = 60$ with 2.5×10^4 states (dashed black), $L = 100$ with 2.5×10^4 (dark grey) and $L = 240$ (black) with 95 states. For each curve only one error bar in every three is shown for clarity. The bottom panel shows $\delta f(\alpha)$ versus α. Note that there is no correspondence between the abscissa axes of the upper and lower plots. For clarity, two values of q for the black line are explicitly written.

3.2.1 Coarse-graining for negative q

In the present case the scaling variable is L, and the formulae (3.2) and (3.3) for the singularity spectrum are only affected by the substitution: $\lim_{\lambda \to 0} \Rightarrow -\lim_{L \to \infty}$. The box size l which determines the integrated probability distribution $\mu_k(l)$ is now a parameter in the expressions (3.2) and (3.3) for $\tau^{\rm typ}(q)$, $\alpha_q^{\rm typ}$ and $f_q^{\rm typ}$. Changing the value of l is effectively equivalent to renormalize the system size to a smaller value $L' \equiv L/l$. Therefore it is clear that the most favourable situation to approach the thermodynamic limit is setting $l = 1$, thus defining the generalized IPR in terms

of the wavefunction itself, $P_q = \sum_{i=1}^{L^3} |\psi_i|^{2q}$. However, when considering negative moments, all the possible numerical inaccuracies that may exist in the small values of $|\psi_i|^2$ will be greatly enhanced, which in turn causes a loss of precision in the right branch ($\alpha > \alpha_0$) of the singularity spectrum. The best way to fix this problem is to use a box-size $l > 1$ for $q < 0$. In this way the relative uncertainties in the smallest values of the coarse-grained integrated distribution $\mu_k(l)$ are reduced with respect to the values of the wavefunction. This coarse-graining procedure to evaluate the negative moments of the wavefunction when doing system-size scaling was first described in Ref. [43] and as we have seen its validity is readily proven when one assumes the scaling relation (2.3) as the starting point of the MFA.

The numerical singularity spectrum is thus obtained from the slopes of the linear fits in the plots of the averaged terms in Eqs. (3.3) versus $\ln L$, for different values of the system size L. Where for positive q we have $\mu_k(1) = |\psi_k|^2$ and for negative q the integrated measure $\mu_k(l > 1)$ is kept, with $l = 5$ in most of the calculations. The value of l for the coarse-graining procedure should not be very large, otherwise finite-size effects will be enhanced again due to the reduction in the effective system size. For the benefit of the reader let us rewrite the formulae (3.3) in the particular case where $l = 1$,

$$-\alpha_q^{\mathrm{typ}} \ln L \sim \left\langle \frac{\sum_i |\psi_i|^{2q} \ln |\psi_i|^2}{\sum_j |\psi_j|^{2q}} \right\rangle, \tag{3.5a}$$

$$-f_q^{\mathrm{typ}} \ln L \sim \left\langle \frac{\sum_i |\psi_i|^{2q} \ln |\psi_i|^{2q}}{\sum_j |\psi_j|^{2q}} - \ln \sum_i |\psi_i|^{2q} \right\rangle, \tag{3.5b}$$

for large enough system sizes L. As before the angular brackets denote the average over all eigenstates.

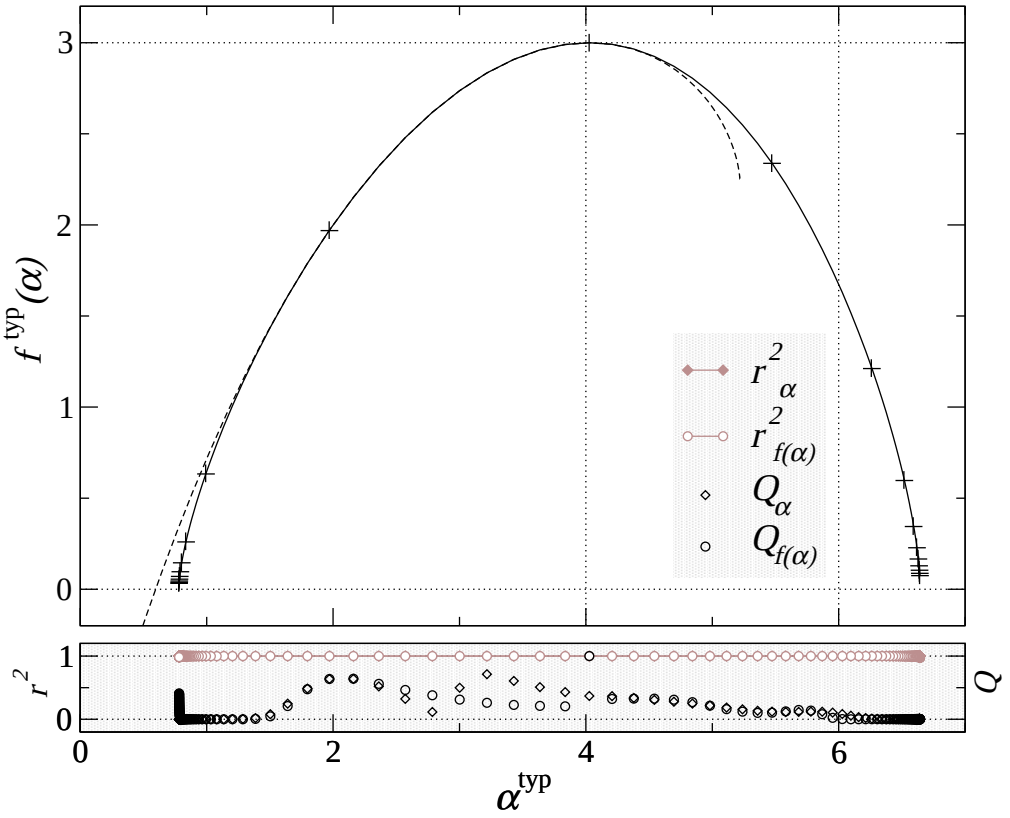

Figure 3.6: Singularity spectrum obtained from typical averaging. System sizes from $L = 20$ to 100 have been considered with $\sim 2.5 \times 10^4$ different wavefunctions for each system size, as shown in Table 3.1. The dashed line is the symmetry-transformed spectrum according to $f(6-\alpha) = f(\alpha) + 3 - \alpha$. The values of q range from $q = -10$ to $q = 10$ with a step of 0.1 ($l = 1$ for $q \geqslant 0$ and $l = 5$ for $q < 0$). Error bars which are equal to one standard deviation highlight the values corresponding to integer q. The lower panel shows the linear correlation coefficient (r^2) and the quality-of-fit parameter (Q) of the linear fits to obtain the values for α and $f(\alpha)$.

3.2.2 General features of $f^{\mathrm{typ}}(\alpha)$ and the effects of the number of states and L

In Fig. 3.6 we show the singularity spectrum obtained from Eqs. (3.3) ($q < 0$) and (3.5) ($q \geqslant 0$). We have considered system sizes ranging from $L = 20$ to 100, and $\sim 2.5 \times 10^4$ states for each system size, as shown in Table 3.1. In spite of the good linear behaviour observed in the fits to obtain α_q^{typ} and f_q^{typ}, shown in Fig. 3.7, the values for Q in the bottom panel of Fig. 3.6, suggest a loss of reliability near the

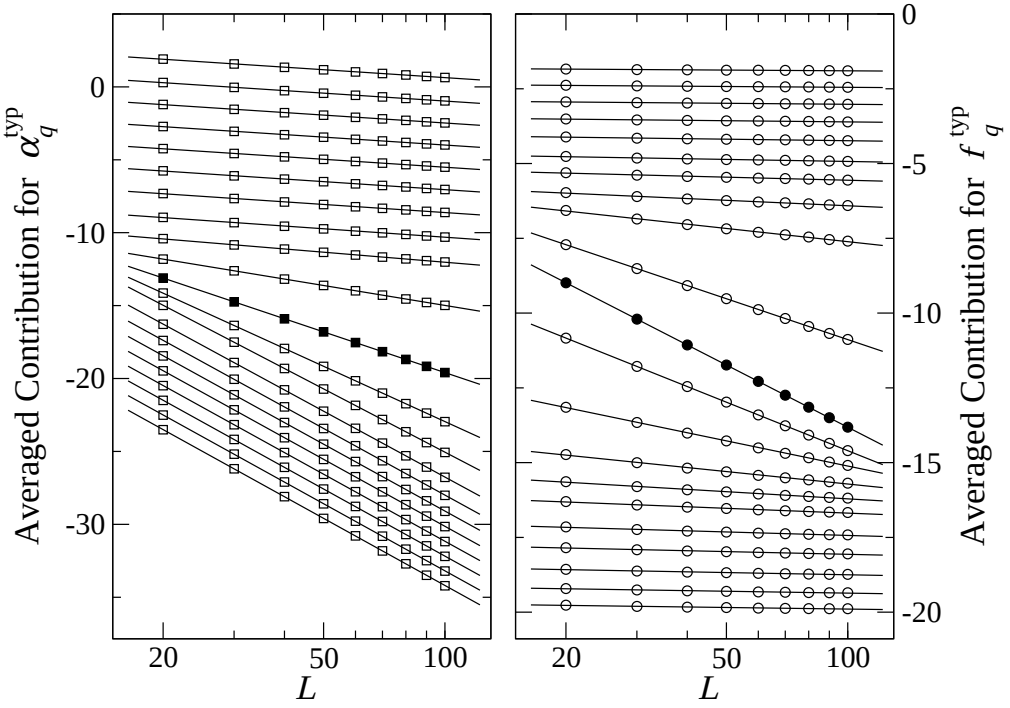

Figure 3.7: Linear fits of Eqs. (3.3) for $\alpha_q^{\rm typ}$ values (left) and $f_q^{\rm typ}$ values (right) of the singularity spectrum in Fig. 3.6. Only fits for integers values of q ranging from $q = 10$ (top) to $q = -10$ (bottom) are shown. The values of $\alpha_q^{\rm typ}$ and $f_q^{\rm typ}$ are given by the slopes of the fits. Data points for $q \neq 0$ have been properly shifted vertically to ensure optimal visualization. Data for $q = 0$ highlighted with filled symbols. Standard deviations are contained within symbol size in all cases.

termination regions of the spectrum. On the other hand the standard deviations of the $\{\alpha^{\rm typ}, f^{\rm typ}(\alpha)\}$ values are really small even near the ends. These uncertainties are directly related to the number of states we average over: the more realizations, the smaller these uncertainties are. It must be clear that these standard deviations only give an idea about the reliability of data as a function of the number of disorder realizations for the particular range of system sizes that one is using. To illustrate the influence of the number of disorder realizations upon the typical average a comparison can be found in Fig. 3.8, between the $f^{\rm typ}(\alpha)$ spectrum obtained after averaging over 10^3 states for each system size and the one for $\sim 2.5 \times 10^4$ states. As can be seen, after this increase in the number of states the overall change in the spectrum is not very significant, altough some variation can be noticed in the

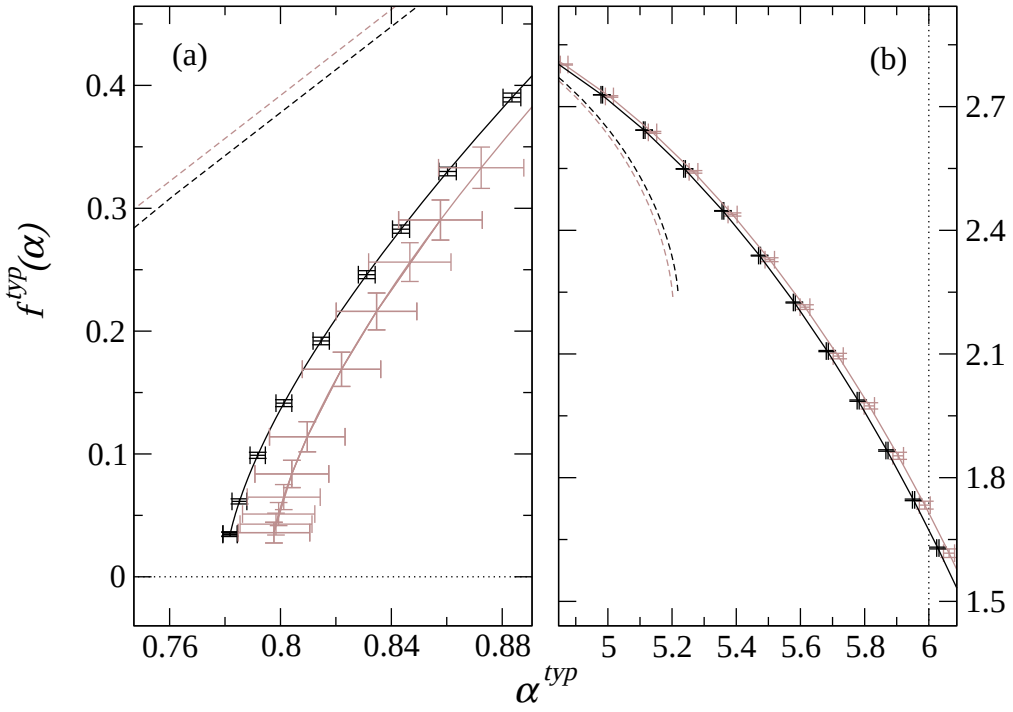

Figure 3.8: Left branch (a) and right branch (b) of the singularity spectrum obtained from typical average, scaling with system sizes from $L = 20$ to 100 for $\sim 2.5 \times 10^4$ states (black) and 10^3 (grey) for each system size. Dashed lines correspond to spectra transformed according to the symmetry law. The values of q range from $q = -10$ to $q = 10$ with a step of 0.1 ($l = 1$ for $q \geqslant 0$ and $l = 5$ for $q < 0$). Error bars are standard deviations.

regions shown. In particular, the right branch of the spectrum moves inwards and the end of the left tail shifts to smaller values of α. In both regions the expected variation of the spectrum is well described by the standard deviations. In the case of Fig. 3.6 according to the standard deviations the conclusion is that a further increase of the number of states will not mean a significant change in the shape of the spectrum. Nevertheless it must also be very clear that if we consider a different range of larger system sizes, noticeable changes could happen in the singularity spectrum. The standard deviations do never account for the effects stemming from the range of system sizes used.

To evaluate the effects due to the system size, we compare in Fig. 3.9 the multifractal spectrum obtained considering different ranges of system sizes with a

similar number of disordered realizations. In the main plot it can be seen how the shape of the spectrum changes in its right (large α) branch, which moves inwards, when we consider system sizes in the interval $[140, 240]$ compared to the situation for sizes in $[40, 100]$. The left end of the spectrum also shifts to smaller values of α when larger system sizes are considered. In this case the standard deviations are noticeable since we have only considered 10^2 states for each system size. In the insets (c) and (d) within Fig. 3.9 a similar comparison can be found for ranges of smaller sizes, $[60, 100]$ versus $[20, 60]$ but with a much higher number of states, $\sim 2.5 \times 10^4$ for each size. In this situation the change is less dramatic, but the tendency remains the same. In particular it should be noticed in Fig. 3.9(c) how the change in the left end of the spectrum is not contained in the uncertainty regions given by the error bars, confirming the fact that these standard deviations do not fully describe system size effects.

3.2.3 Symmetry relation

The symmetry relation (2.21) is only partially fulfilled in Fig. 3.6. Still, a nice overlap between the original spectrum and the symmetry-transformed one occurs in the region around the symmetry point $\alpha = 3$. The agreement is lost when approaching the tails, which are the parts more affected by numerical inaccuracies and system-size effects. For a given range of system sizes, the symmetry relation tends to be better satisfied whenever the number of disordered realizations is increased, as can be observed in Fig. 3.8. On the other hand the improvement of the symmetry is even more dramatic when we consider larger system sizes to do the scaling, as shown in the insets (a) and (b) of Fig. 3.9. In this figure it is evident how the value of $f(\alpha = 6)$ decreases when considering larger system sizes, hence tending towards the upper bound at $\alpha = 2d$ as predicted by (2.21).

A quantitative analysis of the symmetry relation is shown in the upper panel of Fig. 3.10. The best data correspond to the scaling with system sizes in $[140, 240]$

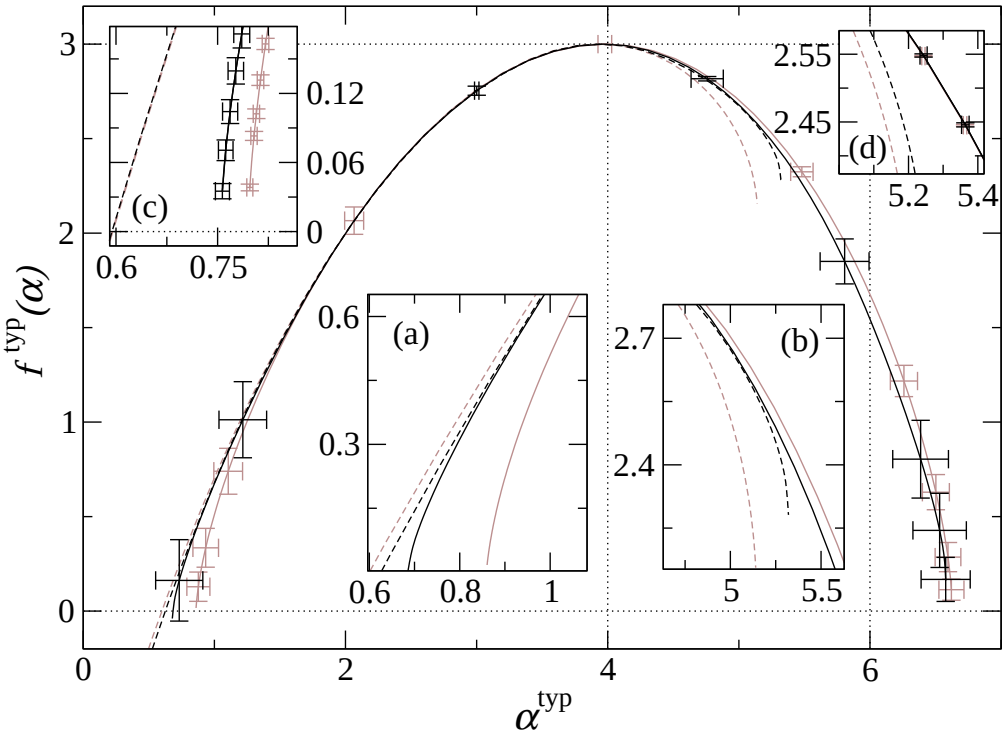

Figure 3.9: Singularity spectrum obtained from typical average using different ranges of system sizes. Grey line: 7 system sizes from $L = 40$ to 100 and 10^2 states for each. Black line: 6 system sizes from $L = 140$ to 240 and $\sim 10^2$ states for each. Insets (c) and (d): Grey line: 5 system sizes from $L = 20$ to 60 and $\sim 2.5 \times 10^4$ states for each. Black line: 5 system sizes from $L = 60$ to 100 and $\sim 2.5 \times 10^4$ states for each. In all cases dashed lines correspond to spectra transformed via the symmetry law. The values of q range from $q = -10$ to $q = 10$ with a step of 0.1 ($l = 1$ for $q \geqslant 0$ and $l = 5$ for $q < 0$). Error bars are standard deviations.

after averaging over ~ 100 states for each size (cp. Table 3.1). Even with such a low number of disorder realizations, the observed symmetry is better on average than the one obtained for sizes in $[20, 100]$ with 2.5×10^4 states for each L. Let us emphasize that for $L = 100$ the total number of wave function values involved in the calculation is 2.5×10^{10} while for $L = 240$ it is only 1.3×10^9. This shows that although the number of disorder realizations is important to improve the reliability of data (reducing the standard deviations), the effect of the range of system sizes is more significant. And although it can be argued that the error bars of the black line in the upper panel of Fig. 3.10 are still very large, we have already shown that

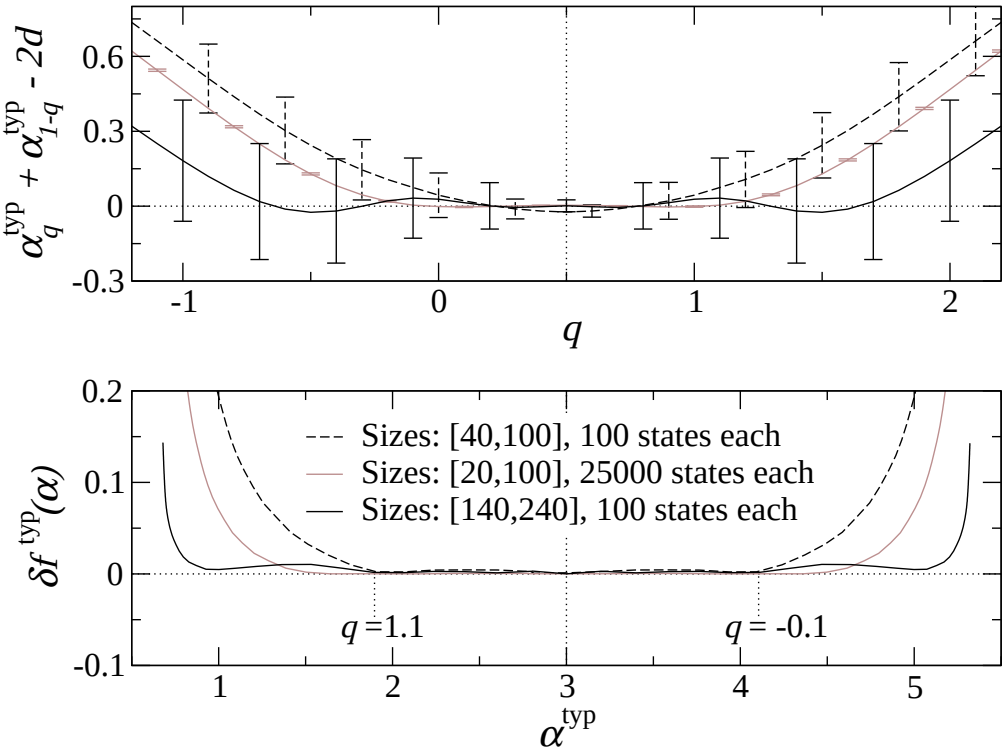

Figure 3.10: Measure of degree of symmetry of the multifractal spectrum of Fig. 3.9 obtained from scaling with system size. The upper panel shows the numerical evaluation of the symmetry law as a function of q. The bottom panel contains $\delta f(\alpha)$ versus α. Dashed black: 7 system sizes from $L = 40$ to 100 and 10^2 states for each. Grey: 9 system sizes from $L = 20$ to 100 and $\sim 2.5 \times 10^4$ states for each. Solid black: 6 system size from $L = 140$ to 240 and $\sim 10^2$ states for each. There is no correspondence between the abscissa axes of the upper and lower plots. For clarity, two values of q for the black line are explicitly written.

when increasing the number of states the symmetry simply gets better and thus the line will move even closer to zero. In the lower panel of Fig. 3.10 the deviation from symmetry $\delta f(\alpha)$ defined in (3.4) is also shown and corroborates these findings.

Hence, whenever the reliability of data is improved by increasing the number of disorder realizations, or when finite-size effects are reduced by considering larger system sizes, we get a better agreement with the symmetry law (2.21) of the multifractal spectrum. Assuming the degree of symmetry is a qualitative measure of the MFA itself, then from a numerical viewpoint, the best strategy when doing scaling with system size and typical averaging would be to go for the largest system sizes

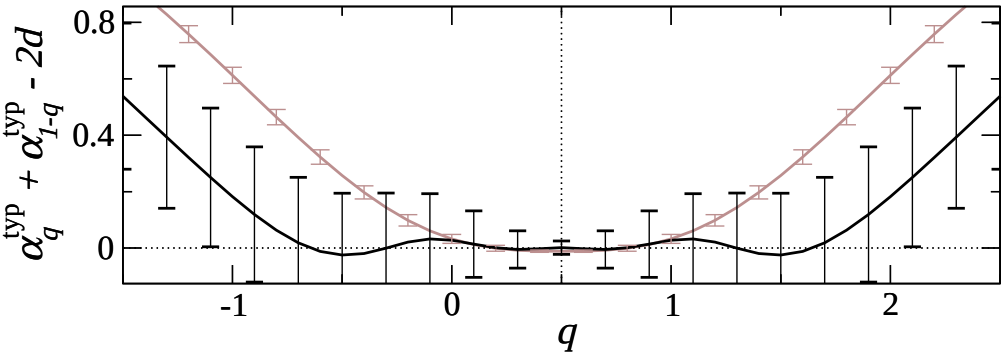

Figure 3.11: Comparison of degree of symmetry for the spectra obtained using typical averaging of P_q for the cases of box-size [BS] scaling (gray) and system-size [SS] scaling (black). The best spectrum for each case has been considered: [BS] $L = 240$ with 95 states and [SS] $L \in [140, 240]$ with 100 states for each size. The plot shows the numerical evaluation of the symmetry law as a function of q.

accessible even though it means having less realizations of disorder.

3.3 Summary

We have obtained the multifractal spectrum from the box- and system-size scaling of the typical average of the gIPR. We find that, upon increasing either the number of disorder realizations or by taking larger system size, the $f^{\text{typ}}(\alpha)$ spectrum becomes evermore close to obeying the proposed symmetry relation (2.21). Using the typical average, the best symmetry in the singularity spectrum is obtained by taking large system sizes. Due to the nature of the typical averaging, taking more states only changes the shape of the $f^{\text{typ}}(\alpha)$ up to a point. By considering larger system sizes, a significant improvement of the symmetry relation is achieved, leading to lower values of α^{typ} and f^{typ} on the left side of the spectrum as well as a better agreement with the upper cut-off of $\alpha \leq 6$.

In Fig. 3.11, let us now compare box- and system-size scaling. With system-size scaling the symmetry is (nearly) satisfied for a wider range of α values as compared with the box-size scaling. Box-size scaling is more strongly influenced by finite-size effects. However, the agreement with the symmetry relation is lost for

both methods at large $|q|$ or equivalently at $|\alpha - 3| \gg 0$. Unsurprisingly, these are the regions greatly affected by numerical inaccuracies and finite-size effects. Hence we conclude that within the accuracy of the present calculation and within the limits of the typical averaging procedure, the proposed symmetry relation (2.21) is valid at the Anderson transition in 3D.

Last, let us remark that the relation (2.21) implies negative values of f for small values of α. As discussed previously, this is hard to see using the typical averaging procedure. In the next chapter, we have also performed MFA using the *ensemble*-averaged box- and system-size scaling approaches. The results again support the existence of the symmetry for an even larger range of α values and including a negative $f(\alpha)$ part for small α.

Chapter 4

Multifractal Analysis with Ensemble Averaging

The numerical MFA is based on an *averaged* form of the scaling law for the gIPR in the limit $\lambda \equiv l/L \to 0$, where the contributions from all finite-size critical wavefunctions are properly taken into account. The scaling law for the ensemble average involves the arithmetic average of P_q over all realizations of disorder,

$$\langle P_q(\lambda) \rangle \propto \lambda^{\tau^{\rm ens}(q)}, \tag{4.1}$$

where $\langle \cdots \rangle$ denotes the arithmetic average over all states. Thus the definition of the scaling exponents is

$$\tau^{\rm ens}(q) = \lim_{\lambda \to 0} \frac{\ln \langle P_q(\lambda) \rangle}{\ln \lambda}, \tag{4.2}$$

and the corresponding definitions of α and $f(\alpha)$ can be written in a compact form as

$$\alpha_q^{\text{ens}} = \lim_{\lambda\to 0} \frac{1}{\ln\lambda} \left\langle \sum_{k=1}^{N_\lambda} \widetilde{\delta}_k(q,\lambda) \ln \widetilde{\delta}_k(1,\lambda) \right\rangle , \tag{4.3a}$$

$$f_q^{\text{ens}} \equiv f(\alpha_q^{\text{ens}}) = \lim_{\lambda\to 0} \frac{1}{\ln\lambda} \left\langle \sum_{k=1}^{N_\lambda} \widetilde{\delta}_k(q,\lambda) \ln \widetilde{\delta}_k(q,\lambda) \right\rangle . \tag{4.3b}$$

Here $\widetilde{\delta}_k(q,\lambda) \equiv \mu_k^q(\lambda)/\langle P_q(\lambda)\rangle$, which is not normalized for every wavefunction but after the average over all of them. Let us emphasize that although Eqs. (4.3) are handy analytically, it is much more useful for numerical purposes to develop them in longer expressions with simpler factors (see Sec. 4.2).

In contradistinction to the typical average in the previous chapter which is determined by the behaviour of representative wavefunctions, the ensemble average weighs the contribution of all wavefunctions equally, including rare (and hence not representative) realizations of the disorder. These rare events are indeed responsible for the negative values of $f(\alpha)$. Therefore it is very important to take them into account by doing the ensemble average, if one wants to have a complete picture of the singularity spectrum. We emphasize that in the thermodynamic limit both averaging processes must provide the same singularity spectrum in the positive region. The relation between typical and ensemble averaging has been previously commented in the literature [39, 49]. The whole set of data used for the analysis, including system sizes and number of samples for each, is the same as in chapter 3 and is described in detail in Table 3.1.

4.1 Scaling with box size

The easiest way to approach the thermodynamic limit in the scaling law (4.1) is considering the limit $l \to 0$ for the box size l. Using this method, we only need realizations for a system with a fixed linear size L, that is partitioned equally into

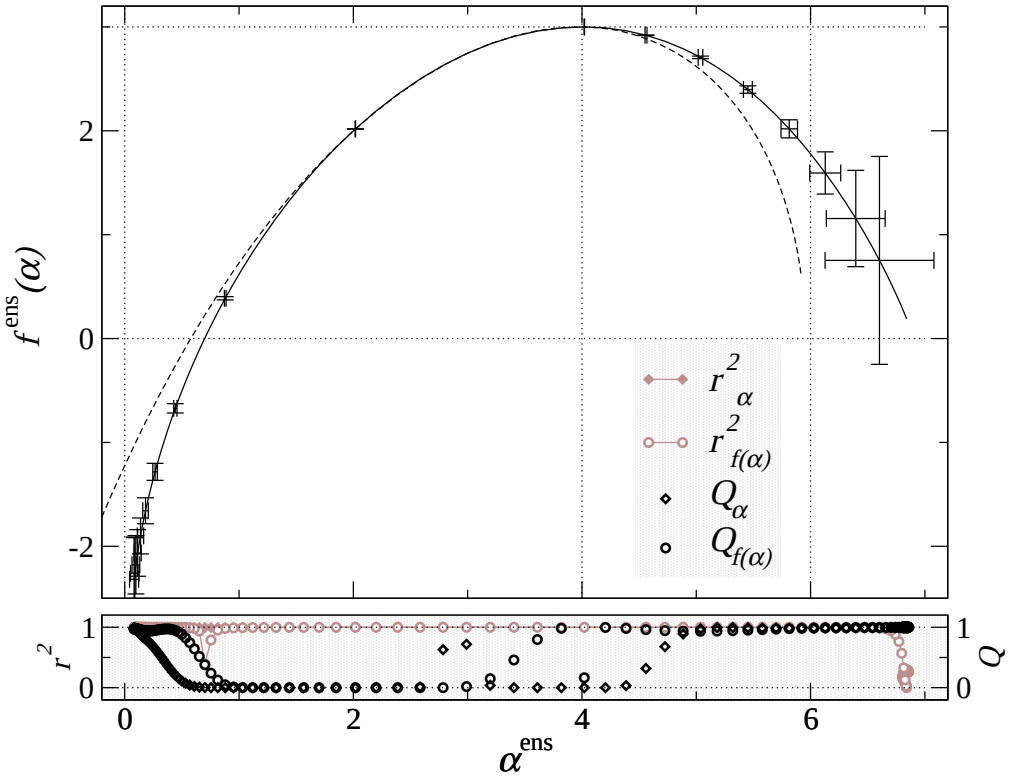

Figure 4.1: Singularity spectrum (black line) obtained using box-size scaling of the ensemble average of P_q for system size $L = 100$ with 2.5×10^4 states. The error bars are equal to one standard deviation. The corresponding symmetry-transformed spectrum $f(2d - \alpha) = f(\alpha) + d - \alpha$ is shown in black dashed line. The values for the linear correlation coefficient r^2 and quality-of-fit parameter Q for both α^{ens} and $f^{\text{ens}}(\alpha)$ are shown in the bottom shaded panel.

an integer number of smaller boxes of linear size l. This is the same partitioning scheme that we have considered in the previous chpter when studying the typical average of the scaling law.

For each state, the q-th moment of the box probability $\mu_k^q(l)$ is evaluated in each box, and P_q is obtained by summing the contribution from all boxes. The scaling behaviour (4.1) is then obtained for different values of l. In all the computations the values of the box size ranges in the interval $10 \leqslant l \leqslant L/2$.

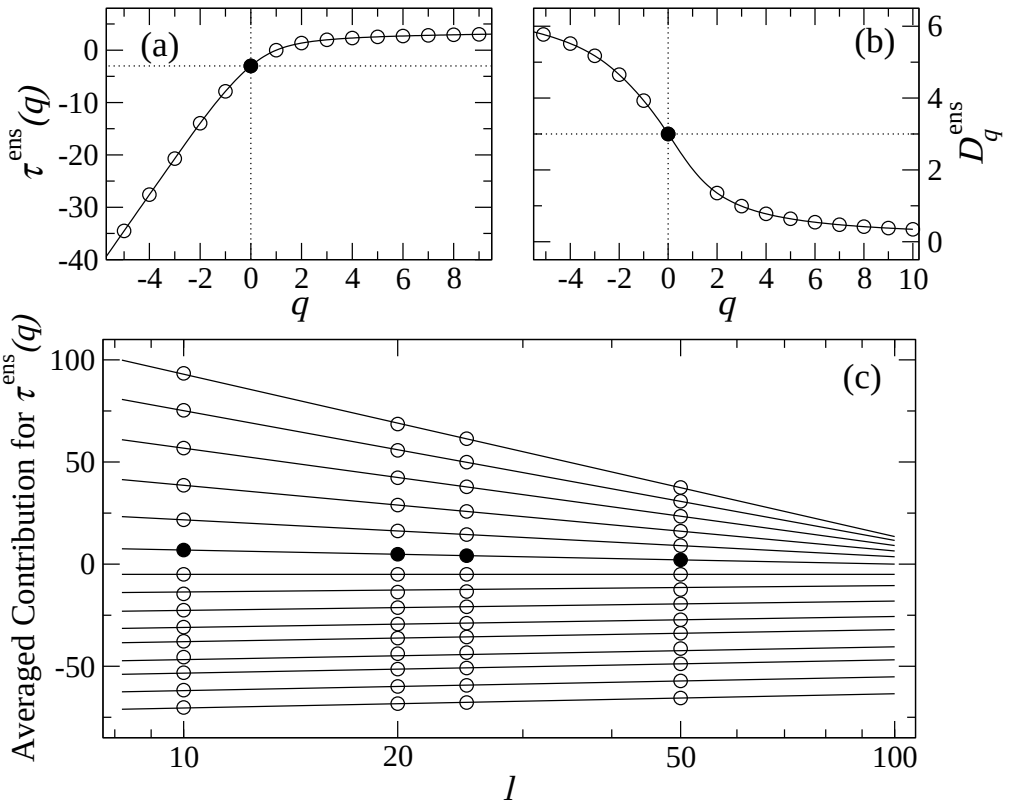

Figure 4.2: (a) Mass exponents $\tau^{\rm ens}(q)$ and (b) generalized fractal dimensions $D_q^{\rm ens}$ corresponding to the singularity spectrum in Fig. 4.1. Dashed lines in upper panels highlight the values $D_0 = d$ and $\tau_0 = -d$. Symbols highlight integer values of q. Panel (c): linear fits of Eq. (4.2). Only fits for integer values of q ranging from $q = -5$ (top) to $q = 9$ (bottom) are shown. The value of $\tau^{\rm ens}(q)$ is given by the slope of the fits. Data points for $q \neq 0$ have been properly shifted vertically for optimal visualization. Data for $q = 0$ highlighted with filled symbols. Standard deviations are contained within symbol size in all panels.

4.1.1 General features of $f^{\rm ens}(\alpha)$

The singularity spectrum for $L = 100$ having 2.5×10^4 states is shown in Fig. 4.1 with its symmetry transformed spectrum. The first thing to notice is that the $f^{\rm ens}(\alpha)$ spectrum attains negative values in the region of small α, corresponding to high values of the wave function amplitudes. The negative region of the multifractal spectrum describes the scaling of certain sets of unusual values of $|\psi_i^2|$ which only occur for rare critical functions. Let us recall that $f(\bar{\alpha}) < 0$ is the fractal dimension

of the set of points where $|\psi_i^2| \sim L^{-\bar{\alpha}}$, which implies that the number of such points decreases with the system size as $L^{-|f(\bar{\alpha})|}$. These negative dimensions are then determined by events whose probability of occurrence decreases with the system size. The negative part of the spectrum provides valuable information about the distribution of wavefunction values for a finite-size system near the critical point and is needed to give a complete characterization of the multifractal nature of the critical states at the metal-insulator transition. At the left-half part of $f^{\rm ens}(\alpha)$ in Fig. 4.1, we observe its termination in the negative region towards $\alpha \to 0$. The values of α and $f(\alpha)$ are obtained from the slopes of the linear fit of Eqs. (4.3) via a general χ^2 minimization taking into account the statistical uncertainty of the averaged right-hand side terms. The behaviour of the linear correlation coefficient r^2 and the quality-of-fit parameter Q for the different parts of the spectrum (corresponding to different values of the moments q) is shown in the bottom panel of Fig. 4.1. The r^2 value is very near to one for almost all α which shows the near perfect linear behaviour of the data points. The parameter Q gives an estimation on how reliable the fits are according to the error bars of the points involved in the fits. The unusual decrease of Q observed around $\alpha = 3$, corresponding to $q \sim 0.5$, in Fig. 4.1 is due to an underestimation of the standard deviations of the points in the fits, since the linear correlation coefficient is still very high in this region. It can also be seen that the uncertainties for the points of $f^{\rm ens}(\alpha)$ tend to grow when approaching the ends of the spectrum. This effect is more significant when doing ensemble average, but it should be naturally expected since the higher the value of $|q|$ is, the more the numerical inaccuracies of $|\psi_i|^2$ are enhanced, specially in the region of negative q, corresponding to the right branch of the spectrum. The mass exponents $\tau^{\rm ens}(q)$ and the fits of Eq. (4.2) are shown in Fig. 4.2, along with the generalized fractal dimensions $D_q^{\rm ens} \equiv \tau^{\rm ens}(q)/(q-1)$ corresponding to the spectrum in Fig. 4.1.

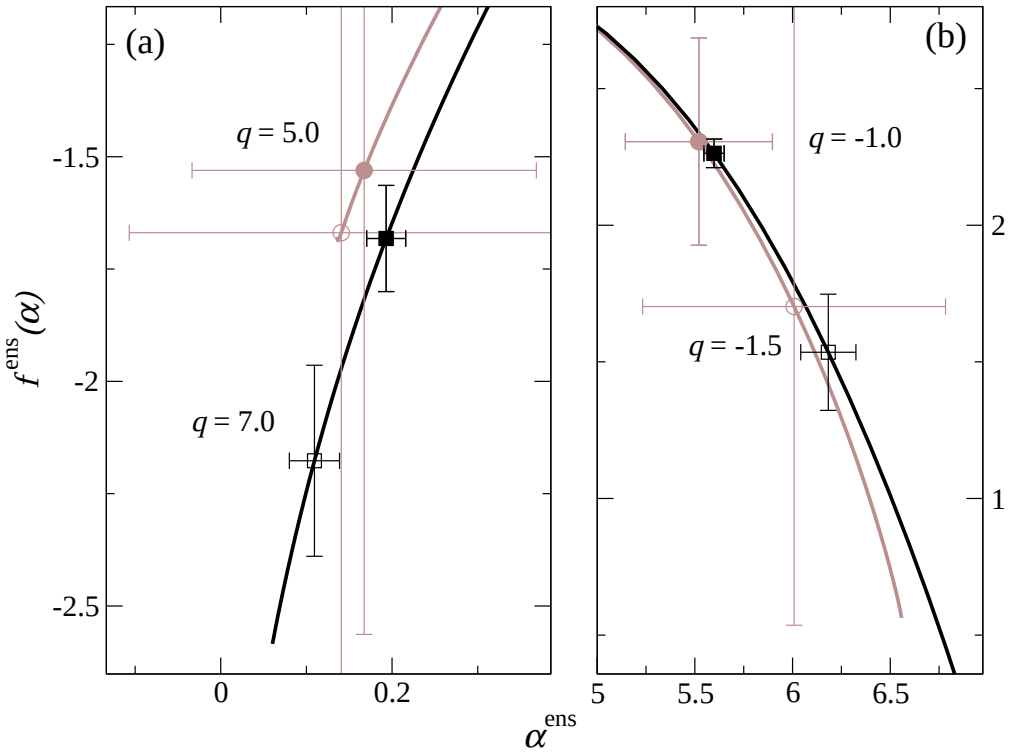

Figure 4.3: Left (a) and right (b) branches of the singularity spectrum obtained using box-size scaling and ensemble average for system size $L = 60$ with 2.5×10^2 (grey) and 2.5×10^4 (black) number of states. The filled symbols denote $q = 5.0$ (a) and $q = -1.0$ (b). The empty symbols mark $q = 7.0$ (a) and $q = -1.5$ (b). The error bars are equal to one standard deviation.

4.1.2 Effects of system size and disorder realizations on $f^{\mathrm{ens}}(\alpha)$

In Fig. 4.3 we study the effects of the number of states and disorder realizations on $f^{\mathrm{ens}}(\alpha)$ for $L = 60$ having 2.5×10^2 and 2.5×10^4 states. Considering two particular q values at each tail, when the number of samples is increased we see that the domain of $f^{\mathrm{ens}}(\alpha)$ is enlarged. The point corresponding to a given q appears later in the spectrum and thus the left end reaches more negative values with more states [Fig. 4.3(a)]. The same stretching effect can also be observed for the right branch in Fig. 4.3(b). Additionally the reliability of the data points in the singularity spectrum is significantly improved as shown by the huge decrease in their uncertainties. These effects prove the strong dependence of the ensemble averaging on the number of

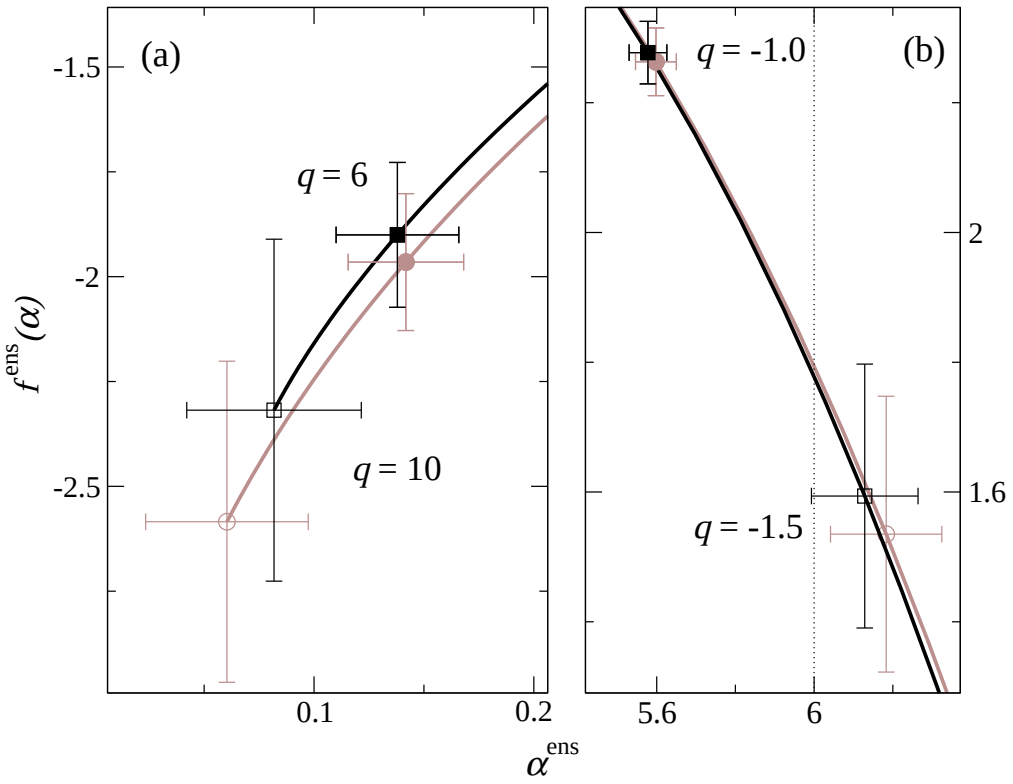

Figure 4.4: Left (a) and right (b) branches of the singularity spectrum obtained using box-size scaling and ensemble average for system sizes $L = 60$ (grey) and $L = 100$ (black) where each has 2.5×10^4 states. The filled symbols denote $q = 6.0$ (a) and $q = -1.0$ (b). The empty symbols mark $q = 10.0$ (a) and $q = -1.5$ (b). The error bars indicate one standard deviation.

samples taken.

The effect of the system size on the shape of the singularity spectrum is presented in Fig. 4.4. Here we consider system sizes $L = 60$ and $L = 100$ each having 2.5×10^4 number of states. Once again, we take two particular q values at each tail as shown in panels (a) and (b) and observe how their locations change when the system size is varied. When we consider a bigger system size with the same number of realizations, the domain of $f^{\text{ens}}(\alpha)$ tends to decrease, and so for the same q range, we see less negative values at the left end [Fig. 4.4(a)]. In other words to be able to observe the same extent of the negative $f^{\text{ens}}(\alpha)$ values of $L = 60$, one must average over more states when a bigger system size such as $L = 100$ is considered.

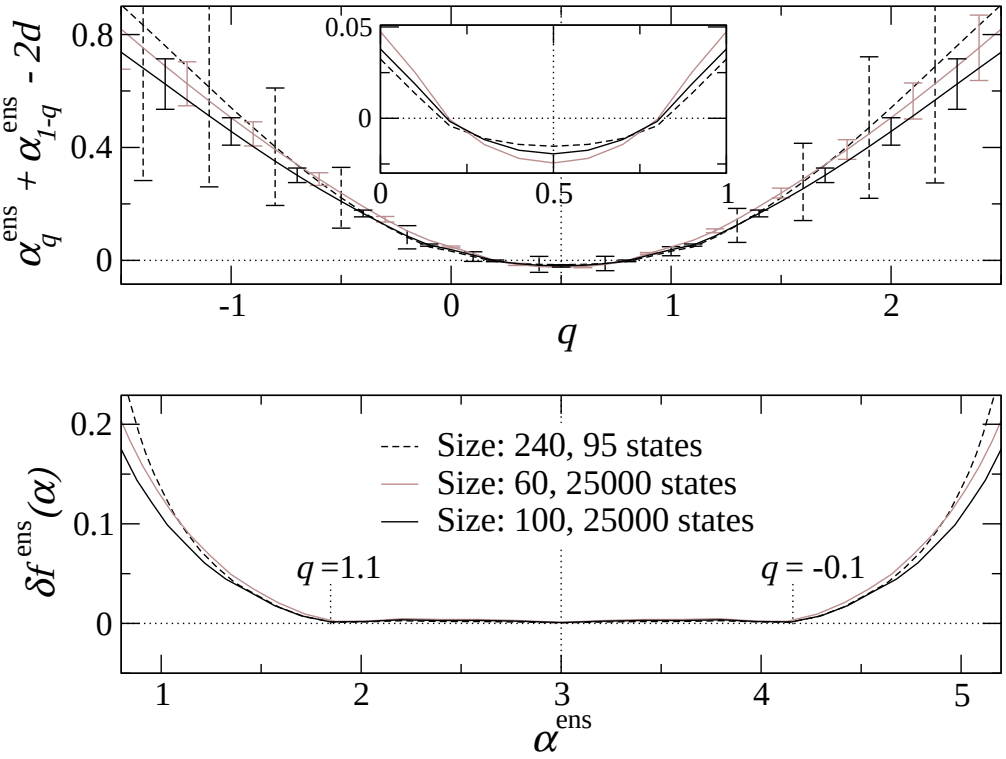

Figure 4.5: Measure of degree of symmetry of the multifractal spectrum obtained from ensemble average doing scaling with box size. The upper panel shows the numerical evaluation of the symmetry law as a function of q for system sizes $L = 240$ (dashed black) with 95 states, $L = 60$ (gray) with 2.5×10^4 states and $L = 100$ (solid black) for 2.5×10^4 states. For each curve only one error bar in every three is shown for clarity. The bottom panel shows $\delta f(\alpha)$ versus α. There's no correspondence between the abscissa axes of the upper and lower plots. For clarity, two values of q for the black line are explicitly written.

The same shrinking effect also occurs in the right branch of the spectrum. This unexpected behaviour is due to the nature of the ensemble averaging process, that is strongly determined by the contribution of rare events which are less likely to happen for larger systems. This important effect will be discussed in more detail in Sec. 4.2.

4.1.3 Symmetry relation

In the upper panel of Fig. 4.5 we give a numerical evaluation of the symmetry law. An approximate estimation of the symmetry law is also shown in the lower panel

using (2.21), which measures the distance between the spectrum and its symmetry-transformed counterpart. We compare data for $L = 240$ (95 states), $L = 60$ (2.5×10^4 states) and $L = 100$ (2.5×10^4 states). Our results show that in general the closest agreement to the symmetry in the singularity spectrum is achieved for the cases with the highest number of disorder realizations, in particular for $L = 100$ ($f(\alpha)$ shown in Fig. 4.1). Although around the symmetry point $q = 1/2$ the spectrum obtained using the largest system size available, $L = 240$ with 95 states, tends to behave slightly better (inset in upper panel of Fig. 4.1), the tendency is inverted when looking at a broader region of q values. This result is a clear manifestation of how important the number of disorder realizations is when doing ensemble average.

It is therefore clear that the more realizations, the better the symmetry is. Obviously a bigger system size helps reduce finite-size effects, but we have shown that increasing system size also implies generating more states in order to obtain the same extent of $f^{\text{ens}}(\alpha)$. Thus from a numerical viewpoint an agreement between system size and disorder realizations must be found to optimize the use of box-size scaling and ensemble averaging.

4.2 Scaling with system size

The scaling with the system size may be the most adequate way to describe the thermodynamic limit of the scaling law for the gIPR (4.1) ($L \to \infty$), however the numerical eigenstate problem is highly demanding for very large 3D systems [28].

The formulae (4.2) and (4.3) for the singularity spectrum are now affected by the substitution: $\lim_{\lambda\to 0} \Rightarrow -\lim_{L\to\infty}$. As for the typical average 3, the box size l which determines the integrated probability distribution is set to $l = 1$ for non-negative moments ($q \geqslant 0$) and to a value $l > 1$ (usually $l = 5$) for $q < 0$, in order to minimize the errors and the uncertainties in the right branch of $f(\alpha)$. For

the case $l = 1$ the formulae to obtain the spectrum reduce to

$$-\alpha_q^{\rm ens} \ln L \sim \frac{\left\langle \sum_i |\psi_i|^{2q} \ln |\psi_i|^2 \right\rangle}{\left\langle \sum_j |\psi_j|^{2q} \right\rangle}, \tag{4.4a}$$

$$-f_q^{\rm ens} \ln L \sim \frac{\left\langle \sum_i |\psi_i|^{2q} \ln |\psi_i|^{2q} \right\rangle}{\left\langle \sum_j |\psi_j|^{2q} \right\rangle} - \ln \left\langle \sum_i |\psi_i|^{2q} \right\rangle. \tag{4.4b}$$

We note the clear difference between the ensemble average (4.4) and the typical average techniques [Eqs. (3.5) in chapter 3]. The values of $\alpha_q^{\rm ens}$ and $f_q^{\rm ens}$ are obtained from the slopes of the linear fits of the averaged terms in Eqs. (4.3) ($q \geqslant 0$) and (4.4) ($q < 0$) versus $\ln L$, for different values of the system size L.

4.2.1 General features of $f^{\rm ens}(\alpha)$

The multifractal spectrum obtained from the ensemble average is shown in Fig. 4.6, where we have considered 9 different linear system sizes ranging from $L = 20$ to 100 for the scaling after averaging over $\sim 2.5 \times 10^4$ states for each size as shown in Table 3.1. The branch of negative values characterizing $f^{\rm ens}(\alpha)$ can be clearly seen. The absence of an infinite slope in the spectrum when crossing the abscissa axis must also be emphasized. As discussed in chapter 3 this confirms the fact that the divergence of the slope at the termination points observed when doing the typical average, $f^{\rm typ}(\alpha)$, is purely a finite-size effect, since both averages must provide the same result for $f(\alpha) \geqslant 0$ in the thermodynamic limit. This is also supported by the systematic shift of the left end of $f^{\rm typ}(\alpha)$ to smaller values of α whenever more states or larger system sizes are considered. The error bars for the values of $f^{\rm ens}(\alpha)$ are considerably larger than the ones obtained for $f^{\rm typ}(\alpha)$ using the same system sizes and disorder realizations [Fig. (3.6) in chapter 3]. This is of course a consequence of having larger errors for the points used in the linear fits, shown in Fig. 4.7. These higher uncertainties are due to the nature of the average itself and the probability distribution function for the generalized IPR. The

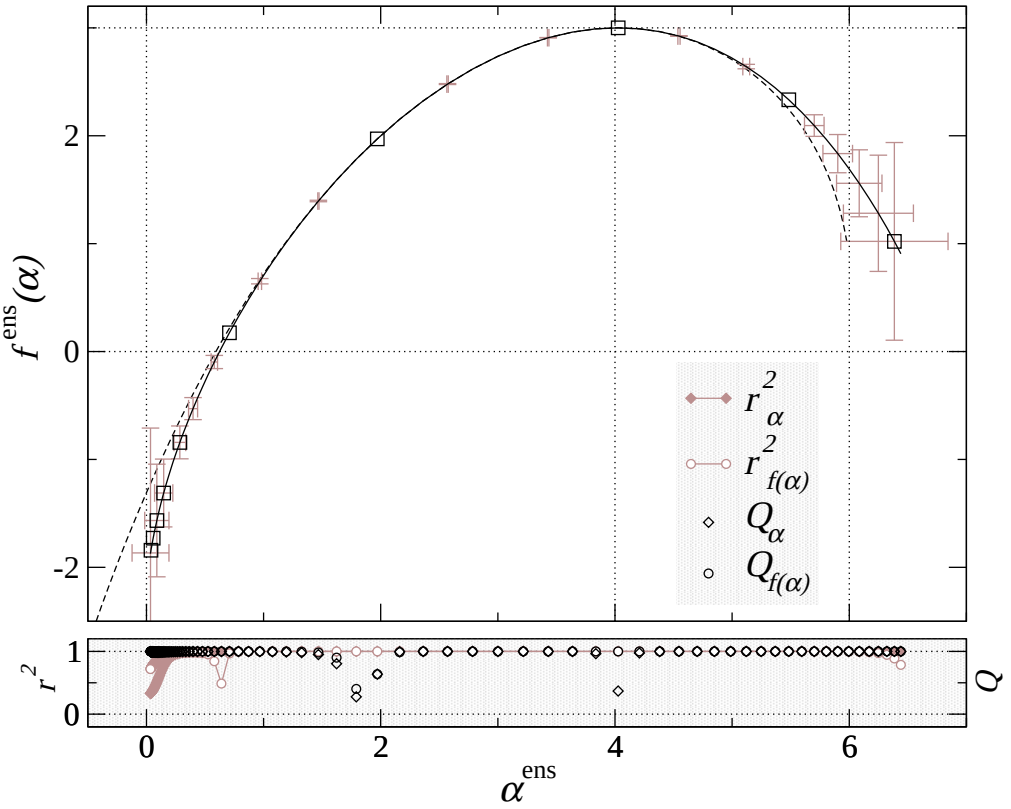

Figure 4.6: Singularity spectrum obtained from ensemble averaging. System sizes from $L = 20$ to 100 have been considered with $\sim 2.5 \times 10^4$ different wavefunctions for each system size as shown in Table 3.1. The dashed line is the symmetry-transformed spectrum. The values of q range from $q = -2$ to $q = 7$ with a step of 0.1 ($l = 1$ for $q \geqslant 0$ and $l = 5$ for $q < 0$). Symbols highlight the values corresponding to integer q. Error bars in grey are standard deviations. The lower panel shows the linear correlation coefficient (r^2) and the quality-of-fit parameter (Q) of the linear fits to obtain the values for α and $f(\alpha)$.

probability density for P_q is an asymmetric function around its maximum with long tails [49,50], resembling a log-normal distribution. The calculation of the arithmetic average of P_q, involved in the ensemble average is therefore much more heavily based on the number of disorder realizations than the determination of the geometric mean used for the typical average, and thus larger uncertainties and slower convergence must be expected for the ensemble-averaged situation with the same number of wavefunctions. Regarding the errors in the values of $f^{\text{ens}}(\alpha)$, it is remarkable how their magnitude grows, for high values of $|q|$, apparently at the same rate as the

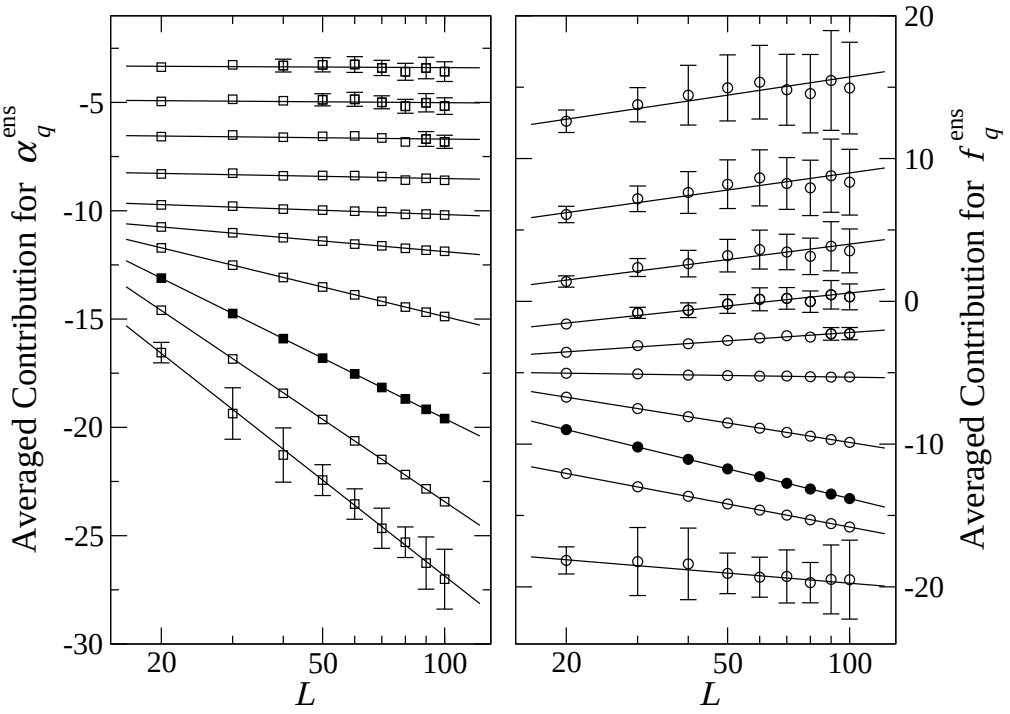

Figure 4.7: Linear fits of Eqs. (4.3) for $\alpha_q^{\rm ens}$ values (left) and $f_q^{\rm ens}$ values (right) of the singularity spectrum in Fig. 4.6. Only fits for integers values of q ranging from $q = 7$ (top) to $q = -2$ (bottom) are shown. The values of $\alpha_q^{\rm ens}$ and $f_q^{\rm ens}$ are given by the slopes of the fits. Data points for $q \neq 0$ have been properly shifted vertically to ensure optimal visualization. Data for $q = 0$ highlighted with filled symbols. When not shown, standard deviations are contained within symbol size.

spectrum deviates from the symmetry-transformed curve (dashed line in Fig. 4.6). This suggests that it might be possible to observe almost a perfect agreement with the symmetry law, using this small range of system sizes for the scaling, if the number of realizations were large enough.

4.2.2 Effects of the number of disorder realizations on $f^{\rm ens}(\alpha)$

The effect of increasing the number of states in the ensemble average can be seen in Fig. 4.8, for scaling with $L \in [20, 100]$. A reduction of the standard deviations must be expected whenever more realizations are taken into account. To make this clear we have considered two situations: averaging over 10^3 states or over $\sim 2.5 \times 10^4$ states for each size. In Fig. 4.8 the points with the specified vertical uncertainty

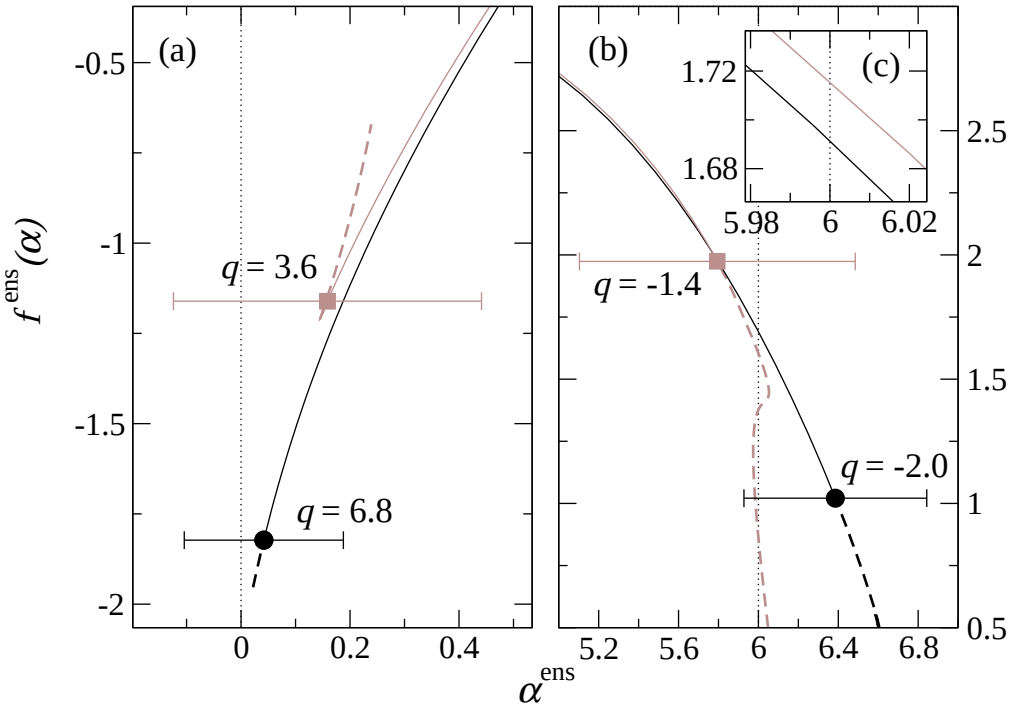

Figure 4.8: Left (a) and right(b) branches of the singularity spectrum obtained from ensemble averaging scaling with system sizes from $L = 20$ to 100 and same number of states for each size: (grey) 10^3, (black) $\sim 2.5 \times 10^4$. The values of q range from $q = -10$ to $q = 10$ with a step of 0.1 ($l = 1$ for $q \geqslant 0$ and $l = 5$ for $l < 0$). The vertical standard deviation for the points marked with filled symbols is always $\sigma_f = 1.0$, and only the uncertainty for α has been included, for clarity. The q value corresponding to each of the symbols is indicated. Dashed lines represent the spectrum in each case for higher values of q. Inset (c) shows the change in the value $f(\alpha = 6)$ for the cases: (grey) 5×10^3 states for each size, (black) $\sim 2.5 \times 10^4$ states for each size.

appear later (for higher values of q) on the left and right branches of the spectrum when we increase the number of states in the average. This clearly means that for a fixed position on the $f^{\text{ens}}(\alpha)$ curve, the uncertainty shrinks when more states are included. There is however, another significant effect that must be emphasized. In Fig. 4.8(a) and (b), the spectrum obtained for values of q higher than the ones indicated is represented by dashed lines. For the average including only 10^3 samples for each size, the values of the spectrum for high $|q|$ are completely absurd and $f(\alpha)$ behaves in an unexpected way, showing "kinks" and bumps as a consequence of a

loss of precision in the fits caused by very large uncertainties. This implies that by increasing the number of states in the ensemble average not only the standard deviations are reduced for each point, but the domain of accessible values for $f(\alpha)$ is also enlarged, e.g. for more wavefunctions the spectrum reaches more negative values [Fig. 4.8(a)]. This is in marked contrast to the typical average for which one obtains almost the same range of $f(\alpha)$ independently of the number of states considered. When doing the ensemble average, the appearance of these "kinks" in the spectrum, either for system-size or box-size scaling where they have also been observed, is always the fingerprint of a lack of sampling of the distributions, i.e. not enough disorder realizations.

In the inset (c) of Fig. 4.8, we have also illustrated the behaviour of the value $f(\alpha = 6)$, at the upper boundary required by the symmetry relation, when the number of states is changed from 5×10^3 to $\sim 2.5 \times 10^4$ for each system size. The spectrum tends to be in better agreement with the upper boundary required by (2.21) when the number of disorder realizations increases.

4.2.3 Effects of the range of system sizes on $f^{\mathbf{ens}}(\alpha)$

In order to study the effects of the system size, we show in Fig. 4.9 the singularity spectrum obtained doing scaling in different intervals: $L \in [40, 100]$ and $L \in [140, 240]$, taking ~ 100 wave functions for each size in both cases. The fact that we have only averaged over 100 states for each size, makes the standard deviations noticeably large, however this does not affect the conclusions qualitatively. When we consider larger system sizes for a fixed number of disorder realizations, the region where we can reliably obtain the multifractal spectrum shrinks. Moreover if we go to high enough values of $|q|$ (highlighted by dashed lines in Fig. 4.9), it can be noticed how the wrong behaviour of $f(\alpha)$ is enhanced. This is a very counterintuitive result, since one would expect that for increasing system sizes, the number of disorder realizations needed to obtain the spectrum with a given degree of reliability should

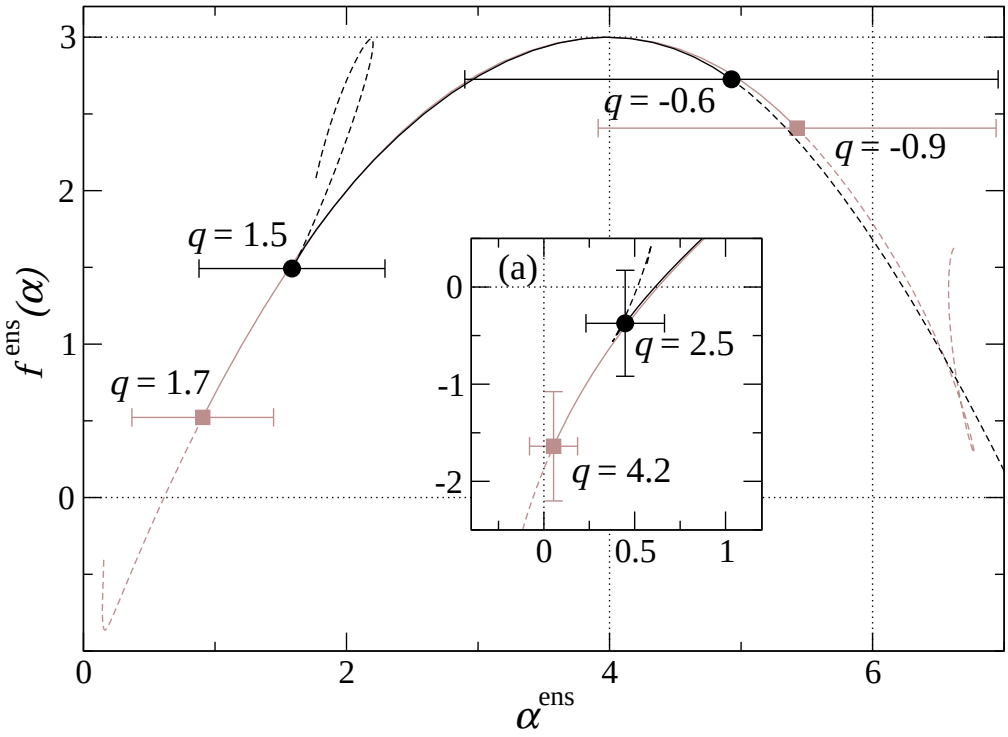

Figure 4.9: Singularity spectrum obtained from ensemble averaging scaling with 7 system sizes $L \in [40, 100]$ and 10^2 states for each size (grey), and 6 system sizes $L \in [140, 240]$ and $\sim 10^2$ states for each size (black). The values of q range from $q = -10$ to $q = 10$ with a step of 0.1 ($l = 1$ for $q \geqslant 0$ and $l = 5$ for $l < 0$). Filled symbols correspond to points with the same vertical standard deviation ($\sigma_f \simeq 1.0$, not shown for clarity). Dashed lines represent the spectrum in each case for values of q higher than the ones indicated beside their corresponding points. Inset (a) shows the spectrum for a different set of data: $L \in [20, 60]$ (grey) and $L \in [60, 100]$ (black) with $\sim 2.5 \times 10^4$ states for each size in both cases.

decrease proportionally – that is in fact what happens with the typical averaging. However for ensemble averaging the conclusion is just the opposite: if you want to improve the spectrum in a given region of the tails and you consider larger system sizes to reduce finite size effects, the number of disorder realizations must also be increased. This is due again to the nature of the ensemble averaging process and the shape of the distributions for the gIPR. The arithmetic average is heavily based on rare events which are less likely to appear for bigger systems, and so the number of realizations has to grow with the system size in order to include the proper amount

of rare events. This can be more clearly understood in the region of negative fractal dimensions. We know that the number of points in a single wave function such that $|\psi_i^2| \sim L^{-\bar{\alpha}}$ where $f(\bar{\alpha}) < 0$, is $L^{-|f(\bar{\alpha})|} \ll 1$. Therefore to be able to see the region of negative fractal dimensions we would need a number of states $\mathcal{N}$ such that we can guarantee $\mathcal{N}L^{-|f(\bar{\alpha})|} \gg 1$. This implies that the number of disorder realizations must go as $\mathcal{N} \sim L^{|f(\bar{\alpha})|}$, and thus it increases with the system size. This effect can be observed in the inset (a) of Fig. 4.9, where we have compared scaling with sizes $L \in [20, 60]$ and $L \in [60, 100]$ with $\sim 2.5 \times 10^4$ states for each size in both cases. For higher sizes and the same number of states, we are not able to see the same region of negative fractal dimensions. Aside from this effect, it must nevertheless be emphasized that when we consider larger system sizes, the right branch of the spectrum tends to find a better agreement with the upper boundary required by the symmetry law.

4.2.4 Symmetry relation

To discuss the fulfilment of the symmetry using ensemble average and scaling with system size, let us look at Fig. 4.10 where the numerical evaluation of the symmetry law (2.20) is shown for different ranges of system sizes and disorder realizations. The best result, according to the symmetry, corresponds undoubtedly to the case with the highest number of disorder realizations, $\sim 2.5 \times 10^4$, for which the scaling analysis involves sizes from $L = 20$ to 100. The difference is remarkable between the situation corresponding to (i) $L \in [40, 100]$ averaging over 100 states only, where the symmetry is hardly satisfied at all, and (ii) the best case where the development of the plateau for $\alpha_q + \alpha_{1-q} - 2d$ around $q = 0.5$ can be seen very clearly. The spectrum obtained for $L \in [120, 240]$ with ~ 100 states for each size also deviates noticeably from the symmetry. These differences can also be seen in the bottom panel of Fig. 4.10 where the degree of symmetry is estimated by $\delta f(\alpha)$.

For the ensemble average going to very large system sizes is not the best

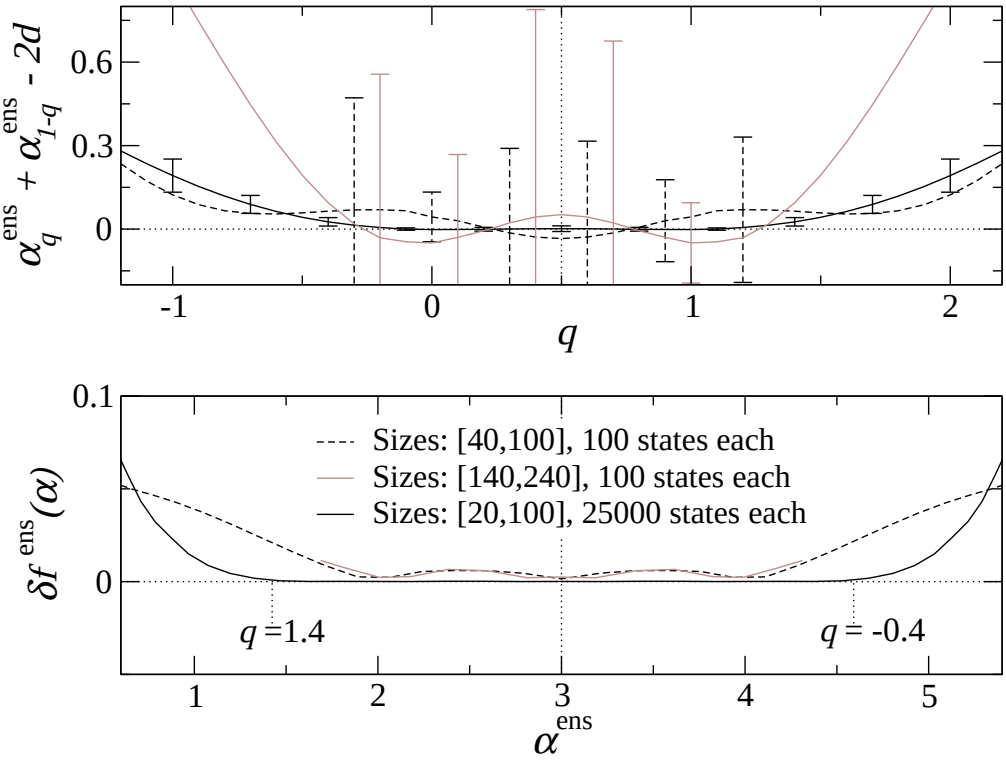

Figure 4.10: Measure of degree of symmetry of the multifractal spectrum obtained from ensemble average doing scaling with system size. The upper panel shows the numerical evaluation of the symmetry law as a function of q. Dashed black: 7 system sizes from $L = 40$ to 100 and 10^2 states for each. Grey: 6 system size from $L = 140$ to 240 and $\sim 10^2$ states for each. Solid black: 9 system sizes from $L = 20$ to 100 and $\sim 2.5 \times 10^4$ states for each. The bottom panel shows $\delta f(\alpha)$ versus α. There's no correspondence between the abscissa axes of the upper and lower plots. For clarity, two values of q for the black line are explicitly written.

strategy unless one can generate an increasing number of states. It must be clear that of course finite size effects will be reduced using large sizes but the number of wavefunctions used for the average has to grow with the system size considered. For a given range of system sizes, increasing the number of states improves the reliability of data, enlarges the accessible domain of $f(\alpha)$, specially in the region of negative dimensions, and improves the symmetry.

4.3 Comparison of different scaling and averaging approaches

Taking the symmetry relation (2.20) as a measure of the quality of the numerical MFA, let us compare the results of the different scaling and averaging techniques. In Fig. 4.11 we show the best analyses obtained from box-size scaling and system-size scaling using typical average and ensemble average in both cases. Data corresponding to the typical average has been extracted from chapter 3. The performance of the system-size scaling technique (solid lines) is clearly much better than box-size scaling (dashed lines). This is not a very surprising result, since one expects finite-size effects to be more enhanced in box-size scaling. For each of the scaling procedures the ensemble average (black) is also better than the typical average (grey). This may be not be so intuitive, since due to the nature of the distribution functions for P_q [49, 50], one might expect the typical average to be a better choice. However it turns out that the ensemble average does better in revealing the true behaviour in the thermodynamic limit.

Let us recall the strategies that give the best result for each of the techniques. For typical average the best symmetry is achieved using the largest system sizes available, either for box-size or system-size scaling, although the number of realizations is not the highest. On the other hand, using ensemble average, the safest choice is to consider smaller system sizes for which a very large number of disorder realizations can be obtained.

4.4 Summary

In this chapter we have studied the symmetry law (2.20) for the multifractal spectrum of the electronic states at the metal-insulator transition in the 3D Anderson model, using the ensemble-averaged scaling law of the gIPR (4.1). A detailed analysis has revealed how the MFA is affected by system size and number of samples.

System-size scaling with ensemble average has manifested itself as the most adequate method to perform numerical MFA, in contrast to box-size scaling and typical average which had been mainly the method of choice in previous studies [36, 54, 55]. Since the ensemble average is strongly based on the number of disorder realizations, from a numerical point of view, the best strategy to carry out the analysis is to consider a sensible range of system sizes for which a very large number of states can be generated.

All our results suggest that the symmetry law is true in the thermodynamic limit, since a better agreement is found whenever a high enough number of disorder realizations and larger system sizes are considered. The symmetry relation (2.21) then provides a powerful tool to obtain a complete picture of $f(\alpha)$ at criticality, since it would suffice to obtain numerically the spectrum in the most reliable region, $q > 0$, and apply the symmetry to complete the function for $q < 0$.

The results obtained for $f(\alpha)$ also provide some useful information about the validity of previous analytical results. The perturbative analysis in $d = 2 + \epsilon$ made by Wegner [40] led to the following spectrum

$$\begin{aligned} f^{\mathrm{W}}(\alpha) =& d - \frac{[\alpha - (d+\epsilon)]^2}{4\epsilon} \\ & - \frac{\zeta(3)}{64}\left[(\alpha - d)^2 - \epsilon^2\right]\left[(\alpha - d)^2 + 15\epsilon^2\right] \end{aligned} \tag{4.5}$$

where $\zeta(x)$ denotes the Riemann zeta function. Remarkably Wegner's result obeys the symmetry relation (2.21), provided the spectrum is indeed terminated at $\alpha = 0$ and $\alpha = 2d$. The first two terms in (4.5) constitute the usual parabolic approximation (PA). The extra quartic term is an overestimation in 3D ($\epsilon = 1$), as explicitly stated by Wegner, which gives a non-acceptable spectrum. To obtain the correct $f(\alpha)$ at $\epsilon = 1$ all the other terms in the perturbation series are required. Therefore the deviation of the multifractal spectra from the PA must be naturally expected. The reduced anomalous scaling exponents $\Delta_q/q(1-q)$ are the most adequate quanti-

ties to analyse non-parabolicity of the $f(\alpha)$ [42], since they are constant for a strictly parabolic spectrum. In Fig. 4.12 we show the reduced anomalous scaling exponents for the best analyses obtained in this work and previously shown in Fig. 4.11. The exponents $\Delta_q/q(1-q)$ are also an extremely sensitive probe of the symmetry relation (2.20), as all small deviations from $\Delta_q = \Delta_{1-q}$ are greatly amplified around the symmetry point. In an ideal case the reduced anomalous scaling exponents should be symmetric around $q = 1/2$ where their maximum must be located. In Fig. 4.12 the method combining system-size scaling and ensemble average is again confirmed as the numerically most adequate to perform MFA.

In spite of the large amount of information that the numerical analyses, here and in chapter 3, and the symmetry relation (2.20) have provided, the complete picture of the multifractal spectrum for the MIT in 3D is still elusive. In particular further research is needed to confirm the possible existence of termination points [39] and whether these happen at negative values on both sides, since this has important implications upon the distribution functions of the wavefunction amplitudes near the localisation-delocalisation transition. Furthermore, we present in the appendix that the symmetry relation can also be expressed in terms of the generalized dimensions D_q. Here, we also give estimates for D_2 and D_4 based on the symmetry relation.

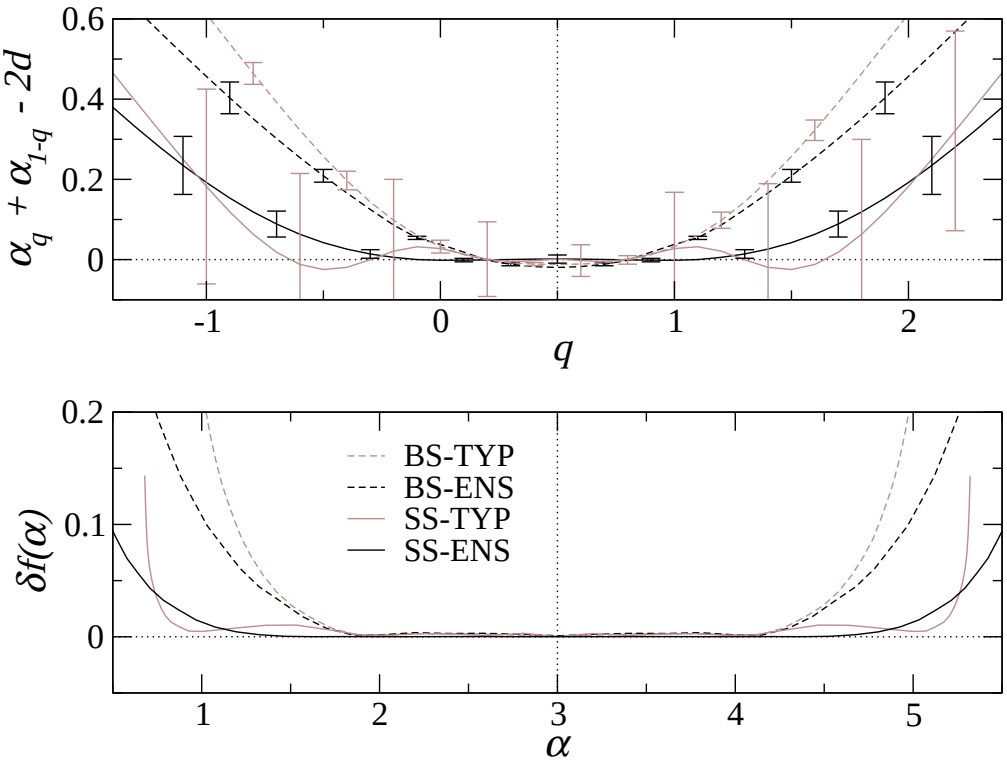

Figure 4.11: Comparison of degree of symmetry for spectra obtained using: box-size scaling typical average [BS-TYP] (dashed grey), box-size scaling ensemble average [BS-ENS] (dashed black), system-size scaling typical average [SS-TYP] (solid grey), system-size scaling ensemble average [SS-ENS] (solid black). The best spectrum for each case has been considered: [BS-TYP] $L = 240$ (95 states), [BS-ENS], $L = 100$ (2.5×10^4 states), [SS-TYP] $L \in [140, 240]$ ($\sim 10^2$ states for each size), [SS-ENS] $L \in [20, 100]$ ($\sim 2.5 \times 10^4$ states for each size). Data for typical average extracted from chapter 3. The upper panel shows the numerical evaluation of the symmetry law as a function of q. The bottom panel shows $\delta f(\alpha)$ versus α. There's no correspondence between the abscissa axes of the upper and lower plots.

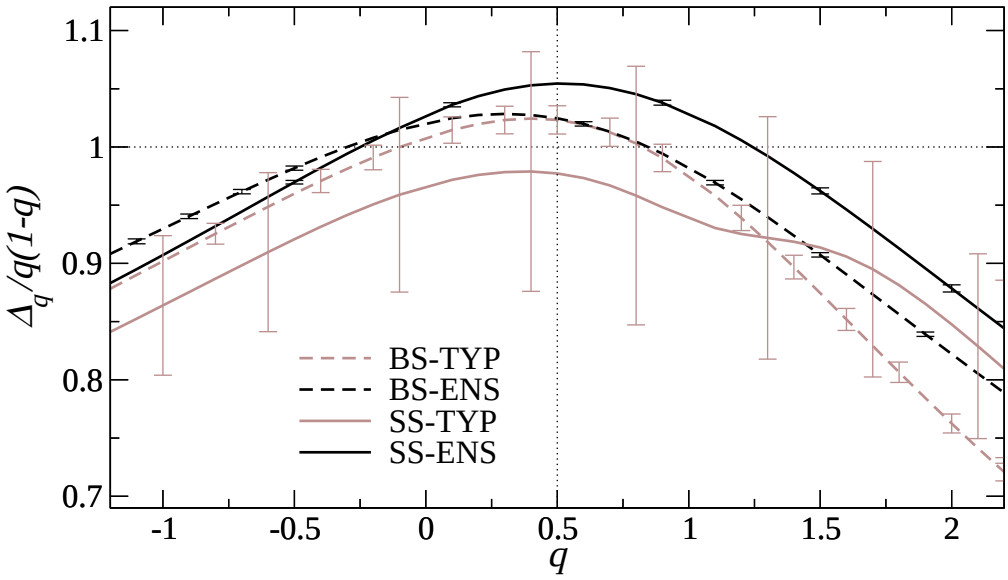

Figure 4.12: Reduced anomalous scaling exponents for the best spectrum obtained using: box-size scaling typical average [BS-TYP] (dashed grey), box-size scaling ensemble average [BS-ENS] (dashed black), system-size scaling typical average [SS-TYP] (solid grey), system-size scaling ensemble average [SS-ENS] (solid black). See caption of Fig. 4.11 for more details. The horizontal dotted line marks the value corresponding to the parabolic approximation.

Chapter 5

Optimisation of Multifractal Analysis using Box-Size Scaling

In the implementation of the box-size scaling method, one usually considers a fixed system size L and partitions it into smaller boxes. The scaling behaviour of the gIPR with box size is then obtained by varying l and averaging over many samples. Hence, with only one system size to be considered, box-size scaling is numerically inexpensive and has been much used previously [36, 54, 55]. There exist, however, multiple ways of carrying out this box partitioning, and some of them might lead to better results, e.g. better fits or an improved statistical analysis. Some improved box-counting methods have already been proposed in different contexts [59–61], although not well suited to be straightforwardly applied to multifractal wavefunctions. In the present chapter we analyse the performance of several partitioning schemes, some of which have previously been used in the literature to perform the MFA [36, 54, 62]. In particular, we shall study the application of cubic versus non-cubic boxes, the use of periodic boundary conditions to enlarge the system, and multiple origins for the partitioning grid, and adaptive linear fits. In Fig. 5.1 we indicate these various strategies schematically. Here, we show that the use of cubic boxes with integer L/l seems to be best suited to calculate the singularity spectrum

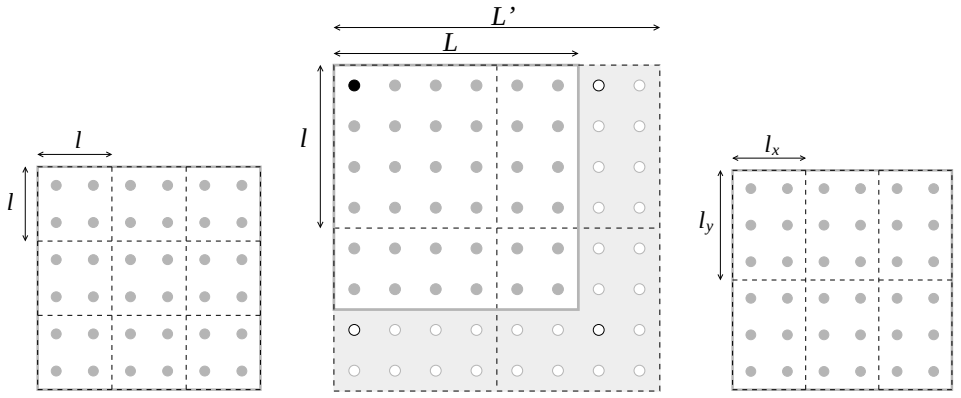

(a) Cubic boxes for integer L/l and $L = 6$ and $l = 2$

(b) Unrestricted values of l. In this case $L = 6$, and for $l = 4$ we have $L' = 2{\times}4$. For the scaling $\lambda = l/L'$ would be used.

(c) Non-cubic boxes with $L = 6$, $l_x = 2$ and $l_y = 3$. For the scaling $\lambda = \sqrt{l_x l_y}/L$

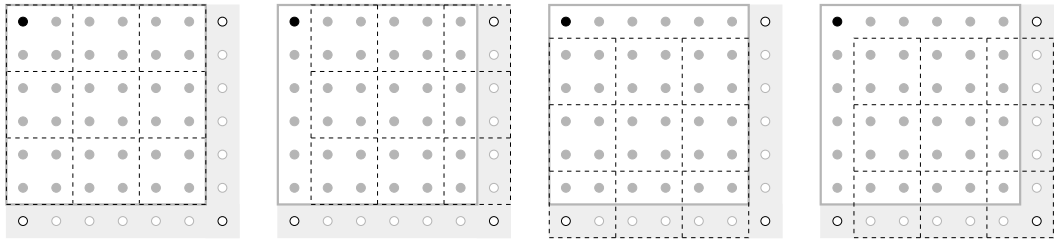

(d) Multiple origins for cubic boxes and integer L/l. The l^2 non-equivalent origins for the partitioning are shown for the case $L = 6$ and $l = 2$

Figure 5.1: Two-dimensional illustration of the different box-partitioning schemes. The black dashed lines mark the partitioning grid. The thick grey line corresponds to the boundaries of the physical system with linear size L. In cases (b) and (d), the empty points in the shaded regions outside the system are obtained using periodic boundary conditions to properly complete all boxes. The position of the black sites highlights the periodicity pattern.

using the box-size scaling of P_q.

In chapters 3 and 4 we had shown that the box-size scaling method is more likely to be affected by finite size effects as compared to the so-called system-size scaling approach. The latter method is based on varying system size L with fixed box size l in the limit $L \to \infty$ [39]. Nevertheless, we emphasize that box-size scaling is still a useful alternative since (i) the computational and data-storage requirements are much less demanding than for system-size scaling, (ii) in certain regions of the spectrum such as close to the maximum, box-size scaling is also quite accurate, and

(iii) in some situations it might be the only applicable method, i.e. when carrying out an MFA of experimental data [10, 63, 64] for which the system size cannot be easily changed. It is therefore important to know how to maximise the use and performance of box-size scaling.

5.1 Partitioning into cubic boxes with integer ratios L/l

The most simple way of partitioning the system with linear size L is to use an isotropic cubic grid which can fit exactly the system. In this case the box-sizes in each direction satisfy $l_x = l_y = l_z$ with values of l such that $L/l \equiv n \in \mathbb{N}$, and thus we always cover the system of size L^3 with an integer number of boxes, as illustrated in Fig. 5.1a. This scheme is the common traditional partitioning strategy of the box-counting method [33,38,54]. The singularity spectrum $f(\alpha)$ obtained for a system with $L = 60$ after taking the typical average over 10^3 states is shown in Fig. 5.2. It must be emphasized that since we are dealing with a discrete system, the values of the box-size must be larger than the lattice spacing, in order to observe properly the multifractal fluctuations of the distribution [38]. Usually we consider values for the box-size in the interval $l \in [10, L/2]$. The points used for the linear fits shown in Fig. 5.3 correspond to $l = 10, 12, 15, 20, 30$. Although easy to implement numerically, the drawback of the present method is that depending on the system size sometimes only a few values for l are allowed and that imposes a restriction on the reliability of the fits to obtain α_q and f_q. In the following sections we consider several additional partitioning strategies and compare their performance to the basic integer cubic-boxes technique.

5.2 Using cubic boxes with unrestricted values for l

As illustrated in panel (b) of Fig. 5.1, an alternative partitioning method would be to use *all* values of l in the range $10 \leqslant l < L/2$. The system is partitioned into

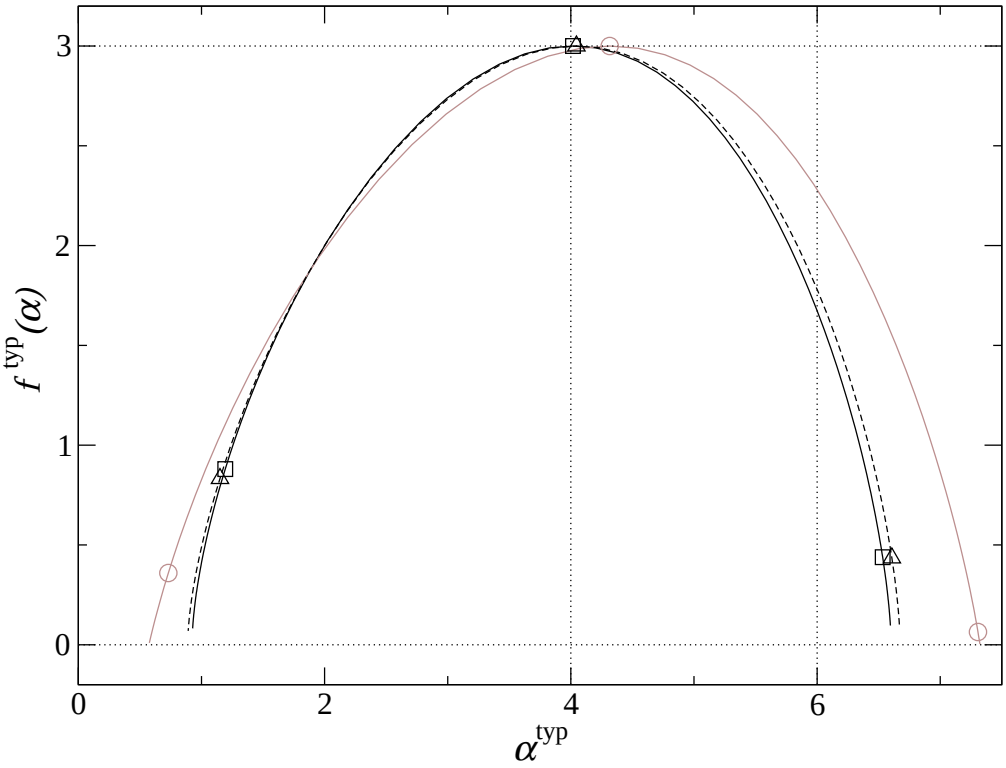

Figure 5.2: Singularity spectrum obtained from box-size scaling of the typical average of P_q for $L = 60$ averaging over 10^3 states using different schemes of box-partitioning: cubic boxes for integer L/l (solid black), cubic boxes for all values of l (grey), non-cubic boxes (dashed black). The symbols denote the position of $q = 2$ (left), $q = 0$ (centre) and $q = -4$ (right).

cubic boxes without imposing the restriction of L/l being an integer. As such, there are values of l where some of the outer boxes will have a lack of sites. This can be overcome by using periodic boundary conditions where all necessary values $|\psi_i|^2$ will be repeated until all boxes are properly filled, and thus the system size is enlarged into L'. For each box-size l the effective system size $L' = nl$, with integer n, is the required length ensuring that the original system is completely covered with the minimum number of boxes. Therefore for each l we have a different L'. One must realise that although the diagonalisation process to obtain the eigenstates uses periodic boundary condition (PBC) to minimise edge effects, no true periodicity pattern exists in the wavefunction itself. However by using this partitioning scheme

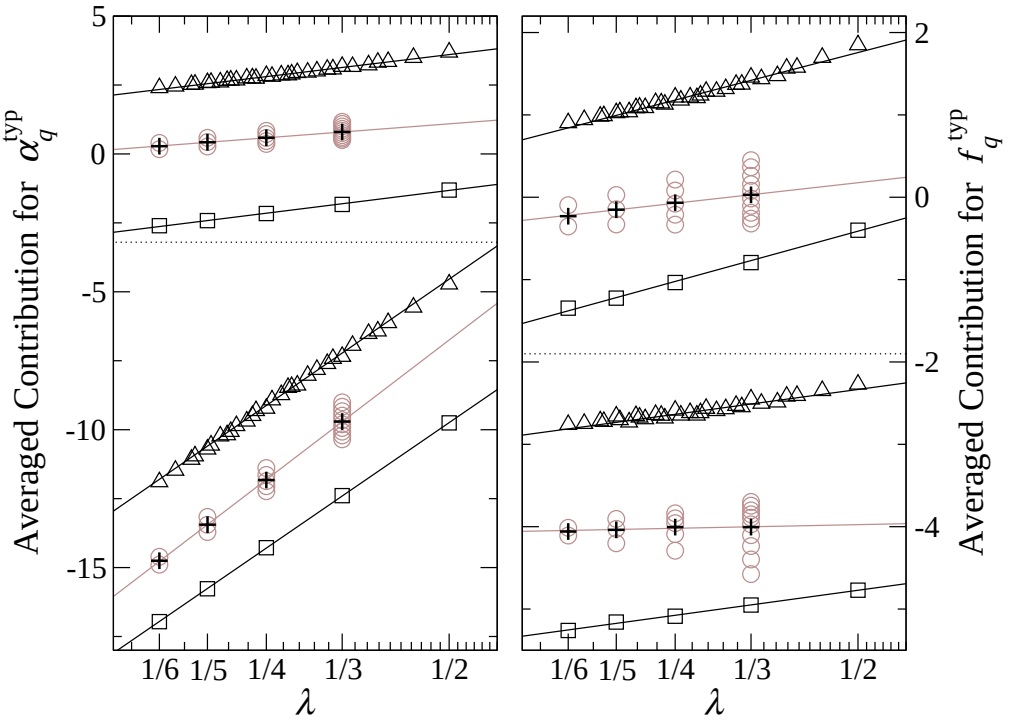

Figure 5.3: Linear fits of Eqs. (3.3) for $\alpha_q^{\rm typ}$ (left) and $f_q^{\rm typ}$ (right) values of the singularity spectra shown in Fig. 5.2 using different schemes of box-partitioning: cubic boxes for integer L/l (black, square), cubic boxes for all values of l (grey, circle), non-cubic boxes (black, triangle). For the method of cubic boxes for all values of l, the data point corresponding to the average contribution for each λ (plus symbol) is also shown. The dotted lines separate fits for $q = 2$ (top) from $q = -4$ (bottom). The values of $\alpha_q^{\rm typ}$ and $f_q^{\rm typ}$ are given by the slopes of the fits. Data points have been properly shifted vertically to ensure optimal visualisation. In all cases, the standard deviations are contained within symbol size.

we are imposing a periodicity pattern on the distribution of $|\psi_i|^2$ that in principle might distort its multifractal properties. Furthermore, we must emphasize here that the enlargement of the system into L' as seen in Fig. 5.1b requires a renormalisation of the wavefunctions if one wants to use the Eqs. (3.3) and (4.3). In Fig. 5.2, a comparison can be found between the typical singularity spectra obtained using the current box-partitioning method and the one involving cubic-boxes with integer L/l. The corresponding linear fits used to obtain $\alpha_q^{\rm typ}$ and $f_q^{\rm typ}$ for a couple of values of q are shown in Fig. 5.3.

Using this partitioning approach the number of available λ values in the fits is

not increased, since whenever the system is enlarged the correct value for the scaling variable must be also redefined to $\lambda = l/L'$, which is the inverse of the number of boxes needed to cover the system in each dimesion. Therefore different box-sizes give contributions to the same λ value in the fit. All these contributions as well as the corresponding weighted average are explicitly shown in Fig. 5.3. The linear fits performed to obtain the singularity spectrum are based on a χ^2 minimisation taking into account the individual standard deviations of each point. The first thing to notice is that the uncertainties of the individual contributions to a given λ are clearly in conflict with the range of values spanned by the points. In fact we have observed that there exists a defined tendency of behaviour for these contributions. In the fits for α_q (left panel in Fig. 5.3), for large positive q and a fixed value of λ the higher contribution is given by the box-size l which does not require an extension of the system. As l is increased and the system size is enlarged, preserving the value of λ, the contributions are progressively smaller. This makes the value of the slope, that is α_q, go systematically to smaller values at the end of the left branch of the spectrum, when compared to the method in Sec. 5.1. For high negative q the behaviour is the opposite, for a given λ the additional contributions of the box-sizes requiring system enlargement grow with the box-size, and therefore the slope attains higher values, i.e. α_q moves towards higher values at the end of the right branch of the spectrum. This leads to a systematic broadening of $f(\alpha)$ as shown in Fig. 5.2 . The effect of the additional contributions in the fits for f_q (right panel in Fig. 5.3) causes a decrease of the slopes for high q, either negative or positive. We have also checked that the shape of the singularity spectrum is strongly dependent on the range of box-sizes taken into account for the linear fit. All these facts clearly make the present partitioning method very unreliable and not suitable to perform a numerical MFA.

5.3 Partitioning with rectangular boxes

Another strategy is to consider an anisotropic non-cubic box partitioning as shown in Fig. 5.1c, with at least one of the linear sizes l_x, l_y, l_z different from the other two. For simplicity we will consider values for the box sides such that $L/l_{x,y,z}$ is an integer. Hence in all directions the system can be covered exactly with an integer number of boxes, although this number can be different for each direction x, y, z. The scaling parameter used in the present case is $\lambda = \bar{l}/L$ with an effective linear box-size defined as $\bar{l} = (l_x l_y l_z)^{1/3}$. Let us note that different combinations of $\{l_x, l_y, l_z\}$ can lead to the same $\bar{l}$ and thus we could have different contributions to the same λ, as in the method described in Sec. 5.2. In the fits of Fig. 5.3 only the averaged contribution for each λ is shown. The corresponding singularity spectrum (Fig. 5.2) is similar to the $f(\alpha)$ obtained using only cubic boxes with integer L/l. We again note a tendency to broaden but it is less pronounced than when using unrestricted values for the box-size. Although in the present case the number of points used in the linear fits is noticeably increased as seen in Fig. 5.3, no significant improvement with regards to the reliability of the $f(\alpha)$ has been observed.

5.4 Using multiple origins for the box partitions

An further possibility to increase the reliability of the multifractal spectrum would be to consider different origins for the partitioning method as demonstrated in Fig. 5.1d. This means that instead of considering the box-partitioning from a single origin, we could use different points in the system as origins. This is equivalent, once we have done the partitioning for a given box-size l and we have a rigid partition grid, to shift the whole wavefunction at the same time one site at a time in all directions a maximum of l sites. Here, one uses the PBC in such a way that the wavefunction sites that are left of the grid in one direction enter the system through the opposite end. Note that each value of $|\psi_i|^2$ is used only once. Hence for each box-size

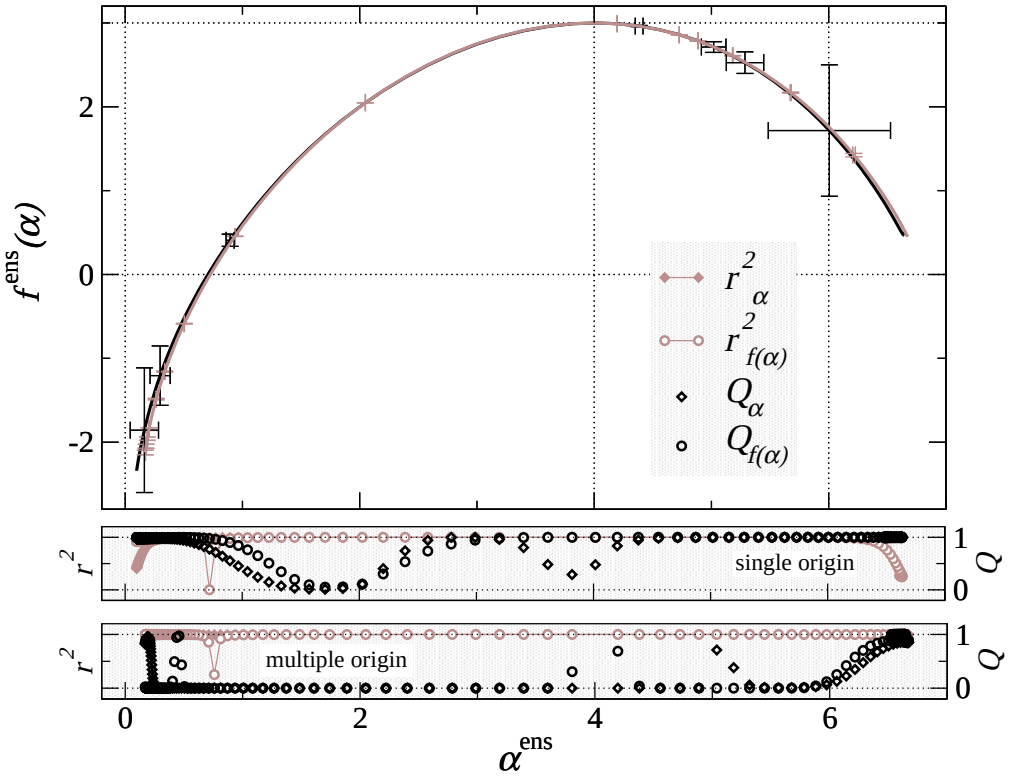

Figure 5.4: Singularity spectrum obtained from box-size scaling for $L = 60$ averaging over 10^3 states. Ensemble average using cubic boxes for integer L/l with single-origin (black) and multiple origins (grey) for the box partitioning. The error bars are equal to one standard deviation. The values for the linear correlation coefficient r^2 and quality-of-fit parameter Q of the fits to obtain $\alpha_q^{\rm ens}$ and $f_q^{\rm ens}$ in the single origin and multiple origin cases are shown in the bottom shaded panels as labelled.

we have l^3 different non-equivalent origins for the box-partitioning. Therefore for a given box-size l the number of contributions in the average of the gIPR P_q is multiplied by l^3. Since the ensemble average is specially sensitive to the number of disorder realizations considered, we show in Fig. 5.4 how $f^{\rm ens}(\alpha)$ behaves when multiple origins are taken into account. The change with respect to the single-origin situation is really insignificant, there is almost a perfect overlap for both lines. But the standard deviations are reduced almost to zero when multiple origins are considered. This is due to the fact that the standard deviations of the averaged contributions for the points in the fits, include a term $1/\sqrt{\mathcal{N}}$ where $\mathcal{N}$ is the number of states we average over. Since every origin counts as a different contribution, then

the uncertainties are greatly reduced. However, let us show that this reduction is in fact misleading and does not really mean an increase in reliability. In the bottom panels of Fig. 5.4, we compare the quality-of-fit parameter Q of the linear fits to obtain α and $f(\alpha)$ for the single-origin and multiple-origin techniques. In both cases the linear correlation coefficient r^2 is close to 1 in the whole α range indicating a good linear behaviour. But in the multiple-origin situation, the values of Q_α and $Q_{f(\alpha)}$ decrease considerably suggesting that the uncertainties of the points in the fits have been clearly underestimated. Therefore there is no gain in reliability. Considering multiple origins maybe seen as considering eigenstates of other disordered systems which correspond to cyclic permutations in the three spatial directions of the initial disorder realization. Clearly, such transformations will not give independent disorder realizations. In fact the contribution of all these wavefunctions related by cyclic permutations must be very similar, since their probability distribution function for $|\psi_i|^2$ values is identical. Therefore it is not correct to consider their contribution as a different disorder realization. That explains why the spectrum hardly changes when compared to the single-origin situation. From our point of view this strategy should not be considered as a good method to reduce the uncertainty. It must also be emphasized that the multiple-origin strategy is very expensive in terms of computational time.

5.5 An adaptive MFA-fit strategy

Aside from the different schemes of partitioning, let us also study another strategy related to the selection of values of box-sizes that are considered for the linear fit. Having in mind that the proper region of values for l to do the scaling might also depend on the value of q, we implemented an adaptive-linear-fit strategy. For a given value of q, we consider a window with a certain number of points to do the fit and we maximise the values of r^2 and Q by shifting this window throughout all the

available interval of values for l, only for box-sizes with integer L/l. In this way for each q the best linear behaviour is achieved using a different region of contiguous l values. In this case we have considered a system with size $L = 210$, for which 14 available values of l exist in the interval $l \in [2, L/2]$, and we tried different widths of the window for l. Unfortunately using this strategy we have not been able to see proper multifractal spectra. Due to the fluctuations of the uncertainty for the points in the fits, sometimes the shifting of the window of l-values does not follow a smooth tendency with q, moreover it also happens that for a given q the best fit for α_q and f_q is achieved in a different range of l. These effects give rise to the appearance of discontinuities and irregularities in $f(\alpha)$. Apparently our initial premise is not true.

5.6 Summary

We have shown that the simple box-partitioning MFA method based on the use of cubic boxes with integer side length L/l and a single-origin for the partitioning, although bearing some limitations, is numerically the most reliable one. It is also optimal in terms of time and computational requirements, and it has already been successfully implemented in chapters 3 and 4 to obtain the scaling behaviour at the Anderson transition for very large system sizes. Therefore it should be considered the method of choice. Furthermore, our results in Fig. 5.2 show that the strategy of cubic boxes with integer sizes L/l and the use of a single origin increases the agreement with the proposed symmetry in the singularity spectrum $f(2d - \alpha) = f(\alpha) + d - \alpha$.

Chapter 6

Multifractal Analysis with the Probability Density Function

The possibility of carrying out a multifractal analysis directly from the raw statistics of intensities $|\psi|^2$, i.e. the probability density function (PDF), is especially interesting since their distributions can be measured experimentally in classical [6] and quantum [10, 11, 64, 65] experiments. However, the numerical relation between the PDF and the multifractal spectrum $f(\alpha)$ has not been completely elucidated. In this chapter we show how to obtain the multifractal spectrum based on the PDF. The PDF-to-$f(\alpha)$ connection is a numerically much simpler procedure than the usual scaling of q-moments of $|\psi|^2$ which is discussed in detail in the previous three chapters. Furthermore, it yields direct understanding of physical properties at criticality, such as the existence of a symmetry relation, the observation of negative fractal dimensions and the physical meaning of the possible appearance of termination points. We apply the PDF-based approach to the three-dimensional Anderson model within the Gaussian orthogonal ensemble, using a large number of critical states at $E = 0$ and very large system-sizes up to $L^3 = 240^3$.

6.1 Relation between $f(\alpha)$ and the PDF(α)

At criticality, the distribution for the wavefunction intensity $|\psi|^2$ has the scaling form [39]

$$\mathcal{P}_L(|\psi|^2) \sim \left(1/|\psi|^2\right) L^{f\left(-\ln|\psi|^2/\ln L\right)-d}. \tag{6.1}$$

Recall that in terms of $\mathcal{P}_L(|\psi|^2)$, the ensemble-averaged gIPR $L^d\langle|\psi|^{2q}\rangle$ for box size $l = 1$ can be expressed as $L^d\langle|\psi|^{2q}\rangle = L^d \int_0^1 \mathcal{P}_L(|\psi|^2)\ |\psi|^{2q}\ \mathrm{d}|\psi|^2 \propto L^{-\tau(q)}$. A distribution function of this form (6.1) satisfies the scaling relation (2.3) of the gIPR. Making a change of variable in terms of $\alpha \equiv -\ln|\psi|^2/\ln L$, the PDF is $\mathcal{P}_L(\alpha) \sim L^{f(\alpha)-d}$, where $f(\alpha)$ is the multifractal spectrum, i.e. the fractal dimensions of the sets of points in the wavefunction with values $|\psi_i|^2 = L^{-\alpha}$.

The relation (6.1) between $\mathcal{P}_L(\alpha)$ and $f(\alpha)$ suggests a complete characterization of multifractality directly from the PDF. The proportionality in (6.1) contains an L-dependent normalization constant which can be naively included as

$$\mathcal{P}_L(\alpha) = \mathcal{P}_L(\alpha_0)L^{f(\alpha)-d}, \tag{6.2}$$

where α_0 is the position of the maximum of the multifractal spectrum, $f(\alpha_0) = d$. Furthermore, since $f(\alpha) < d$ for all $\alpha \neq \alpha_0$, we see that $\mathcal{P}_L(\alpha_0)$ corresponds in fact to the maximum value of the PDF itself. Note that $\mathcal{P}_L(\alpha = \alpha_0)$ as the maximum of the PDF is true only in the thermodynamic limit or for large enough L. Hence α_0 can be easily obtained numerically. Since at criticality the shape of $f(\alpha)$ and hence the position of α_0 do not depend on L, the value of α_0 obtained from the critical PDF must also be L-invariant as we show in Fig. 6.1. From the PDF of $L = 50$ to 200 with 5×10^4 and 100 states respectively, we have estimated the position of the maximum of the PDF to be $\alpha_0 = 4.027 \pm 0.016$ which is in agreement with that obtained from the system-size scaling of the ensemble-averaged gIPR in chapter 4, $\alpha_0 \in [4.024, 4.030]$. Furthermore, using the normalization condition we

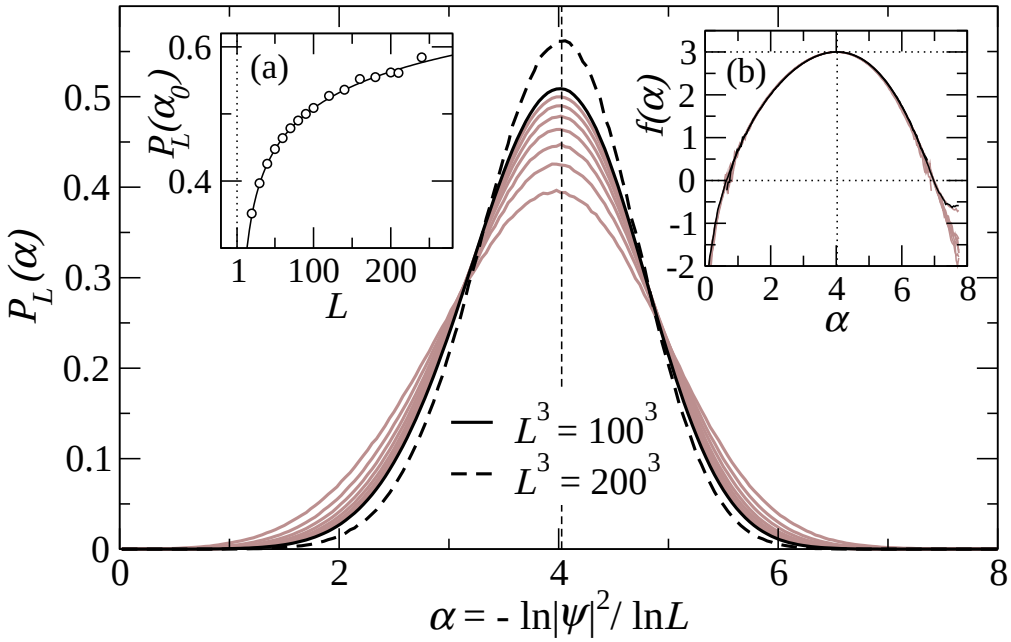

Figure 6.1: PDF at criticality for $\Delta\alpha = 0.04$. The gray lines correspond to L from 30 (bottom) to 90 (top). Standard deviations are within the line width. For $L \leqslant 100$ and $L > 100$ we average over 5×10^4 and 100 states respectively. The vertical dashed line marks the mean value for $\alpha_0 = 4.027 \pm 0.016$ using L from 50 to 200. Inset (a) shows $\mathcal{P}_L(\alpha_0)$ vs L. Standard deviations are contained within symbol size. The solid line is the fit $a\ln(L/l)^b$, with $a = 0.297 \pm 0.002$, $b = 0.490 \pm 0.005$. Inset (b) shows the collapse of all the PDF from $L = 30$ to 240 onto the $f(\alpha)$.

have $\mathcal{P}_L(\alpha_0) = \left(\int_0^\infty L^{f(\alpha)-d}d\alpha\right)^{-1}$. Using the saddle point method, justified in the limit of large L, we compute $\mathcal{P}_L(\alpha_0) \sim \sqrt{\ln L}$, which holds very well even for small L as shown in Fig. 6.1(a).

From the PDF for one fixed L the multifractal spectrum is hence straightforwardly obtained from (6.2) as

$$f(\alpha) = d + \ln[\mathcal{P}_L(\alpha)/\mathcal{P}_L(\alpha_0)]/\ln L. \tag{6.3}$$

In Fig. 6.1(b), we show the corresponding $f(\alpha)$ for the $\mathcal{P}_L(\alpha)$ of different system sizes from $L = 30$ to 240. It is clear that $\mathcal{P}_L(\alpha)$ is always system-size dependent and it is through the $f(\alpha)$ spectrum that all PDFs for different L collapse onto the same function. Therefore the $f(\alpha)$ can also be understood as the natural scale-

invariant distribution of the wavefunction at criticality. We find excellent agreement between the singularity spectrum obtained from the PDF for $L = 30, \ldots, 240$ and the one obtained from the more involved box-size scaling of the gIPR as discussed in chapters 3 and 4. Alternatively, if $f(\alpha)$ is known, the PDF can be easily generated.

6.2 System size scaling of the PDF

In order to minimize finite-size effects, we can also determine $f(\alpha)$ from the PDF using system-size scaling. We note that for a given L the number of points in the wavefunction with values in the interval $\alpha \in [\alpha - \Delta\alpha/2, \alpha + \Delta\alpha/2]$ is $\mathcal{N}_L(\alpha) \equiv L^d \mathcal{P}_L(\alpha)\Delta\alpha$, where L^d is the volume and $\Delta\alpha$ is the bin size used to generate the numerical PDF whose method will be discussed in detail below. Hence the following so-called normalized volume of the α-set $\widetilde{\mathcal{N}}_L(\alpha) \equiv L^d \mathcal{P}_L(\alpha)/\mathcal{P}_L(\alpha_0)$ obeying

$$\widetilde{\mathcal{N}}_L(\alpha) = L^{f(\alpha)}, \tag{6.4}$$

can be used to extract $f(\alpha)$ from a series of systems with different L. Each point in the PDF-generated $f(\alpha)$ is simply computed as the slope of $\ln \widetilde{\mathcal{N}}_L(\alpha)$ versus $\ln L$. In Fig. 6.2 we compare the multifractal spectrum obtained using system-size scaling of the PDF (6.4) with the one from gIPR scaling for $L \in [20, 100]$ and having 5×10^4 critical states for each size. We find very good agreement between both, as well as between the numerical PDFs and those generated from the gIPR $f(\alpha)$ [Fig. 6.2(a)].

Numerically, the PDF is approximated by

$$\mathcal{P}_L(\alpha) \underset{\Delta\alpha \to 0}{\equiv} \left\langle \theta\left(\Delta\alpha/2 - \left|\alpha + \ln|\psi_i|^2/\ln L\right|\right)\right\rangle / \Delta\alpha, \tag{6.5}$$

where θ is the Heaviside step function and $\langle . \rangle$ involves an average over the volume of the system and all realizations of disorder. To minimize the uncertainty especially in the small $|\psi_i|^2$, which becomes greatly enhanced in terms of $\alpha = -\frac{\ln|\psi_i|^2}{\ln L}$, the ampli-

tudes used for the histogram are those obtained from a coarse-graining procedure of the state using boxes of linear size $l = 5$. Therefore the system size in all equations is the *effective* system size L/l. The uncertainty of the PDF value is estimated from the usual standard deviation for a counting process as $\sigma_{\mathcal{P}_L(\alpha)} = \sqrt{\mathcal{P}_L(\alpha)/N_w L^d \Delta\alpha}$, where N_w is the total number of states in the average, and for the α values a constant $\sigma_\alpha = \Delta\alpha/3$ is assigned. This procedure assumes uncorrelated α's and hence $|\psi|^2$'s; this is only true between different disorder realizations, but not necessarily within each state. Hence the errors of the PDF are probably somewhat underestimated and the small uncertainty of the $f(\alpha)$-values obtained from PDF scaling in Fig. 6.2 must be interpreted carefully. There also exists another source of error difficult to quantify, namely, how much the histogram for finite $\Delta\alpha$ deviates from the real PDF when $\Delta\alpha \to 0$. In spite of this, the PDF method is easy to implement numerically and hence a valid alternative to the more demanding gIPR scaling techniques.

6.3 Symmetry Relation in the PDF

The symmetry relation in the singularity spectrum at criticality, $f(2d-\alpha) = f(\alpha) + d - \alpha$ [43] for $L \to \infty$, implies the existence of a symmetry for the PDF (recall Eq. (6.2)) which should also hold for large enough system sizes,

$$\mathcal{P}_L(2d - \alpha) = L^{d-\alpha}\mathcal{P}_L(\alpha). \tag{6.6}$$

In terms of the wavefunction intensities, Eq. (6.6) reads

$$\mathcal{P}_L(L^{-2d}/|\psi|^2) = (L^d|\psi|^2)^3\ \mathcal{P}_L(|\psi|^2). \tag{6.7}$$

With $|\psi|^2 = L^{-\alpha}$, the above equation follows from making a change of variables $\mathcal{P}_L(\alpha)\mathrm{d}\alpha = \mathcal{P}_L(L^{-\alpha})\mathrm{d}L^{-\alpha}$. Hence, $\mathcal{P}_L(\alpha) = -\mathcal{P}_L(L^{-\alpha})L^{-\alpha}\ln L$ and $\mathcal{P}_L(2d-\alpha) = -\mathcal{P}_L(L^{-(2d-\alpha)})L^{-(2d-\alpha)}\ln L$. Equation (6.7) establishes that at the critical point

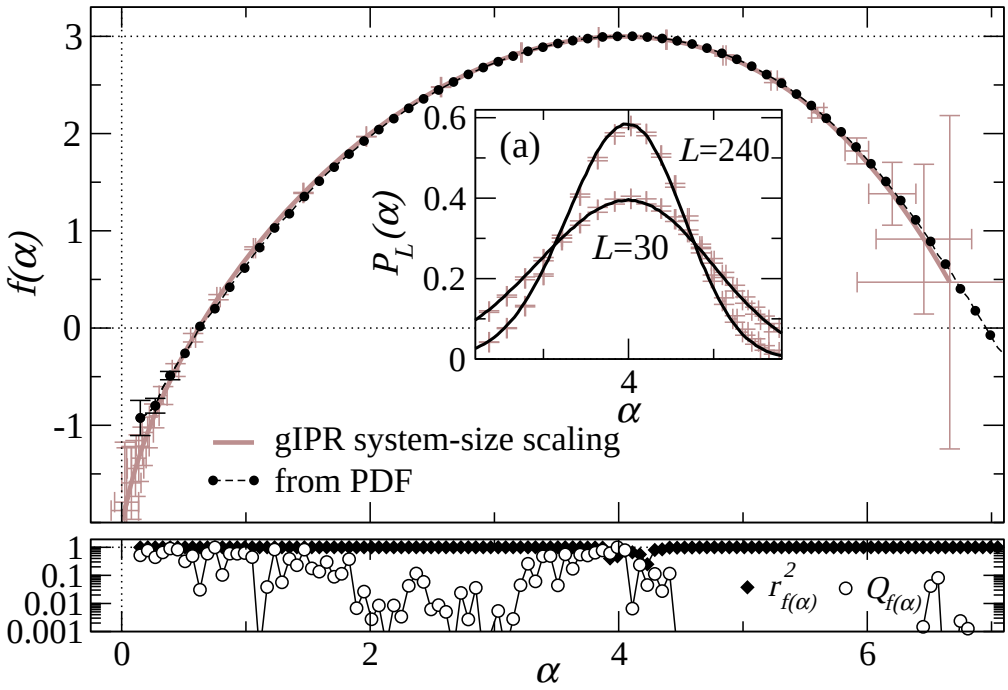

Figure 6.2: $f(\alpha)$ obtained from system-size scaling of the PDF and the gIPR, for $L \in [20, 100]$. Only one every second symbol is shown for clarity. Standard deviations are within symbol size when not shown. The inset shows the numerical PDF (black) and the PDF calculated from the gIPR $f(\alpha)$ (gray). The bottom panel gives the linear correlation coefficient r^2 and quality-of-fit parameter Q for the $f(\alpha)$ obtained from the log-log linear fits of Eq. (6.4).

the distribution of the wavefunction intensity in the interval $L^{-2d} < |\psi|^2 \leqslant L^{-d}$ is indeed determined by the PDF in the region $L^{-d} \leqslant |\psi|^2 < 1$. The lower bound for the $|\psi|^2$ values is a result of the upper bound for the singularity strength $\alpha \leqslant 2d$. Of course, $|\psi|^2_{\max} \leqslant 1 \Rightarrow \alpha \geqslant 0$. Furthermore, the symmetry relation in the PDF confirms the existence of the symmetry axis at $\alpha = d$.

We carry out a numerical check of the symmetry relation (6.6) by evaluating $\delta\mathcal{P}_L(\alpha) = \mathcal{P}_L(\alpha) - L^{\alpha-d}\mathcal{P}_L(2d-\alpha)$ accounting for the distance between the original PDF and its symmetry-transformed counterpart at every α point, as well as the cumulative difference $\delta(L) = \int_0^{2d} d\alpha |\delta\mathcal{P}_L(\alpha)|$ for all α values. The symmetry-transformed PDF for $L = 100$ and the evolution of $\delta\mathcal{P}_L(\alpha)$ for different L are shown in Fig. 6.3. In Fig. 6.3(a), the symmetry-transformed PDF seems to deviate from

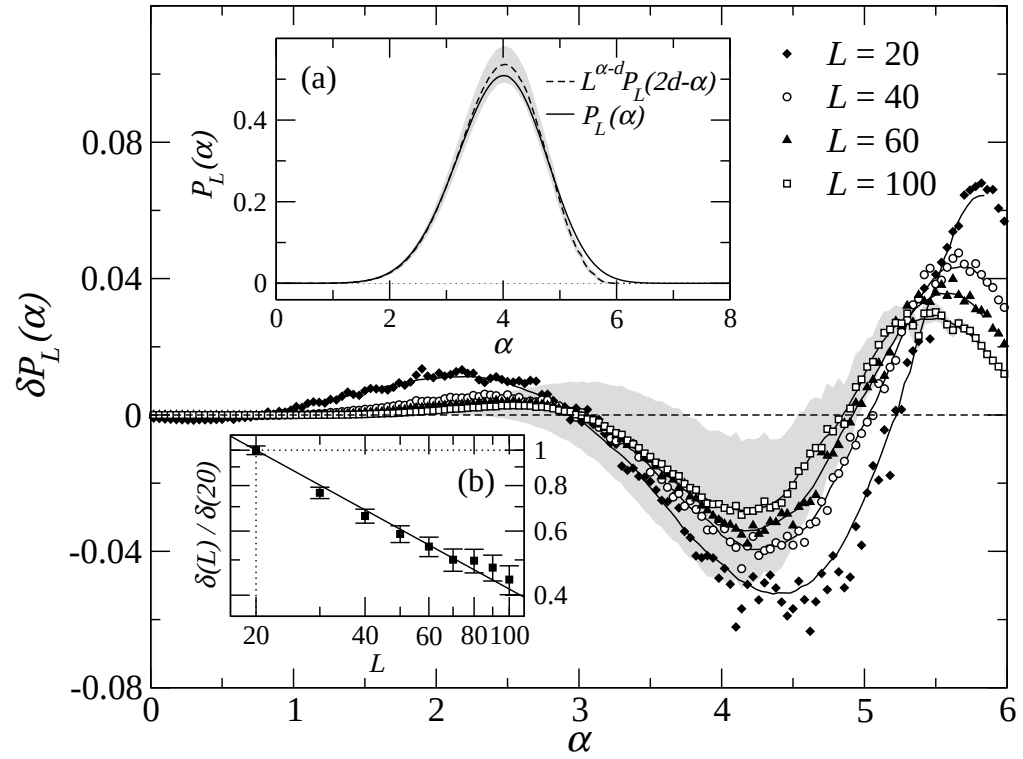

Figure 6.3: Degree of symmetry of the PDF. The shaded region in the background marks the 66% c.i. of the values for $L = 100$. The lines show the evolution in average for each L. The inset (a) displays the symmetry transformed PDF for $L = 100$ and its 95% c.i. (shaded region). The inset (b) shows a log-log plot of $\delta(L)$ normalized to its maximum value. The solid line is a linear fit with slope $b = -0.545 \pm 0.017$.

the numerical PDF in the large α region. Note that the symmetry relation maps the PDF for small $|\psi|^2 < L^{-d}$ onto the PDF for large $|\psi|^2 > L^{-d}$. The large α part of the symmetry-transformed PDF was generated using the small α region of the original PDF, i.e., those regions corresponding to anomalously large $|\psi|^2$ with negative f(α) whose number decreases with L as $N_\alpha \propto L^{-f(\alpha)}$. As one considers more disorder realizations which means increasing the probability of finding this large $|\psi|^2$ then the symmetry relation will be better satisfied especially in the right tail of the PDF. Nevertheless, we show in Fig. 6.3(b) that for a fixed number of states the symmetry relation is better satisfied as L increases, and the improvement can be roughly quantified as $\delta(L) \sim L^{-0.545}$ as shown.

6.4 Non-Gaussian Nature of the PDF

The parabolic approximation for $f(\alpha) \simeq d - \frac{[\alpha-(d+\epsilon)]^2}{4\epsilon}$ in $d = 2 + \epsilon$ [40] implies a gaussian approximation (GA) for the PDF, $\mathcal{P}_L^{GA}(\alpha) = \sqrt{\ln L/4\pi\epsilon}\, L^{-[\alpha-(d+\epsilon)]^2/4\epsilon}$. The PDFs in Fig. 6.1 might indeed appear roughly gaussian and in Fig. 6.4 we show gaussian fits of the PDF for $L = 100$, obtained via a usual χ^2 minimization taking into account the uncertainties of the PDF values. However, the quality-of-fit parameter Q, which gives an indication on the reliability of the fit, is ridiculously small ($Q < 10^{-300000}$). Since the standard deviations of the PDF values may have been slightly underestimated we also study how Q behaves when we intentionally increase the error bars by a factor n. As shown in Fig. 6.4(c) one would have to go to unreasonable high values of $n \sim 85$ to accept a gaussian nature for the PDF as plausible. The deviation from $\mathcal{P}_L^{GA}(\alpha)$ is also noticeable. Hence our statistical analysis confirms that the PDF is non-gaussian in agreement with the observed non-parabolic nature of $f(\alpha)$ at the 3D MIT.

6.5 Rare events and their negative fractal dimensions

The volume of the α-set, $\mathcal{N}_L(\alpha) = L^d \mathcal{P}_L(\alpha)\Delta\alpha$ for a given L, gives the number of points in the wavefunction with amplitudes in the range $|\psi_i|^2 \in [L^{-\alpha-\Delta\alpha/2}, L^{-\alpha+\Delta\alpha/2}]$. It scales with the system size as $\mathcal{N}_L(\alpha) \sim \sqrt{\ln L}\, L^{f(\alpha)}$. The negative values of $f(\alpha)$ correspond then to those α-sets whose volume decreases with L for large enough L. Physically, the negative fractal dimensions at small α are caused by the so-called rare events containing localized-like regions of anomalously high $|\psi_i|^2$ at criticality. The probability, which is proportional to $L^{-d-|f(\alpha)|}$, of finding them likewise decreases with L. In Fig. 6.5, we show examples of rare eigenstates. Due to the finite size term $\sqrt{\ln L}$, the threshold α_- [where $f(\alpha_-) = 0$], below which the decreasing behaviour of $\mathcal{N}_L(\alpha)$ with L is detected, will change with the system size itself, and so the normalized volume (6.4) of the α-set must be used. In Fig. 6.6 we show the behaviour

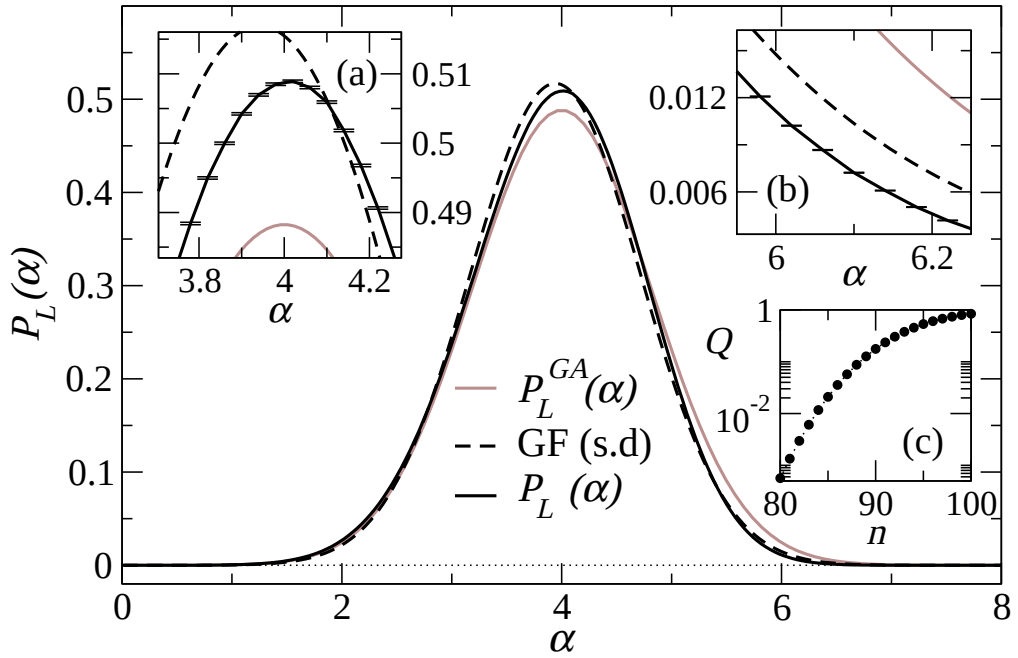

Figure 6.4: Gaussian fit ($\sqrt{a/\pi}\, e^{-a(x-b)^2}$) of the PDF for $L^3 = 100^3$ (dashed-line): $a = 0.840 \pm 0.005$, $b = 3.942 \pm 0.004$, $Q < 10^{-300000}$. The solid gray line shows the GA for $\epsilon = 1$. Insets (a) and (b) are blow-ups of the maximum and the right tail of the PDF. Inset (c) shows the quality-of-fit parameter Q when the standard deviation of the PDF-points is multiplied by the factor n.

of $\widetilde{\mathcal{N}}_L(\alpha)$ vs L for two values of α corresponding to a positive and a negative fractal dimension. The exponential decreasing of the volume of the α-set for $f(\alpha) < 0$ is clearly observed from the PDF values. In Fig. 6.6(a) it is demonstrated how the normalized volume of the α-set becomes scale invariant at α_- and thus $\widetilde{\mathcal{N}}_L(\alpha_-) = 1$. The opposite tendencies with L at each side of α_- can also be seen. The estimated value for $\alpha_- \in [0.643, 0.675]$ from the PDF scaling agrees with the result obtained using the multifractal spectrum from gIPR scaling, $\alpha_- = 0.626 \pm 0.028$.

6.6 Termination points in $f(\alpha)$

The fate of the $f(\alpha)$ spectrum at $\alpha = 0$ and $\alpha = 2d$ is currently under debate in the literature [47] due to the emergence of singularities at these points. At present, it is not clear whether $f(\alpha)$ continues towards $-\infty$ or terminates with finite values. The

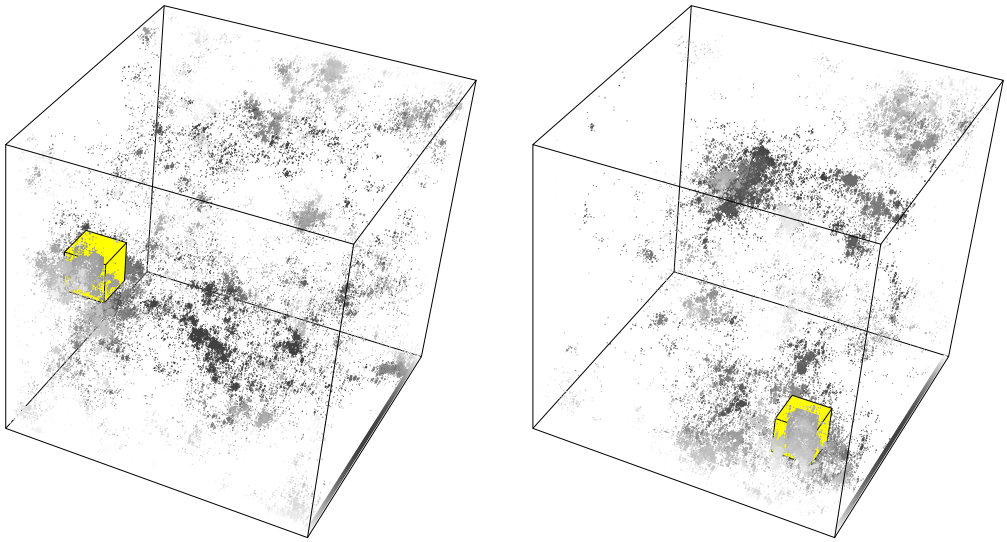

Figure 6.5: Rare eigenstates for the 3D Anderson model ($E = 0$, $W_c = 16.5$) for $L^3 = 100^3$. The sites with probability $|\psi_j|^2 > L^{-3}$ are shown as boxes with volume $|\psi_j|^2 L^3$. The grayscale distinguishes between different slices of the system along the axis into the page. The biggest boxes with black edges enclose the site with the maximum normalized amplitude: $|\psi_i|^2 = 0.4484$ (left) and 0.3617 (right).

physical consequences of the divergence of $f(\alpha)$ at those points are: (i) $|\psi_i|^2 > L^{-2d}$ at criticality since $2d$ would be an upper bound for α, and (ii) the probability to find the most rare event, namely the most extremely localized state ($|\psi_{i_0}|^2 = 1$, corresponding to $\alpha = 0$), at the critical point must always be zero independently of the system size [$\mathcal{P}_L(0) = 0$]. In principle the PDF can be used to look for termination points (TP). However, a reliable analysis in the vicinity of $\alpha = 0$ requires a huge number of disorder realizations; relying on the symmetry relation [43] a study around $\alpha = 2d$ is more appropriate. For $1 \ll \alpha < 2d$ and as long as there is a finite TP, the PDF admits the series expansion We assume that $f'(\alpha)|_{\alpha=0}$ and $f'(\alpha)|_{\alpha=2d}$ remain finite for finite L. Note that a finite TP with $f'(\alpha)|_{\alpha=0,2d} \to -\infty$ implies the same infinite slope for the PDF at $\alpha = 0,\ 2d$. This is not seen in our results.

$$\mathcal{P}_L(\alpha) \simeq \mathcal{P}_L(\alpha_0) L^{f(2d)-d} \left[1 + q_{2d}(\alpha - 2d) \ln L\right], \tag{6.8}$$

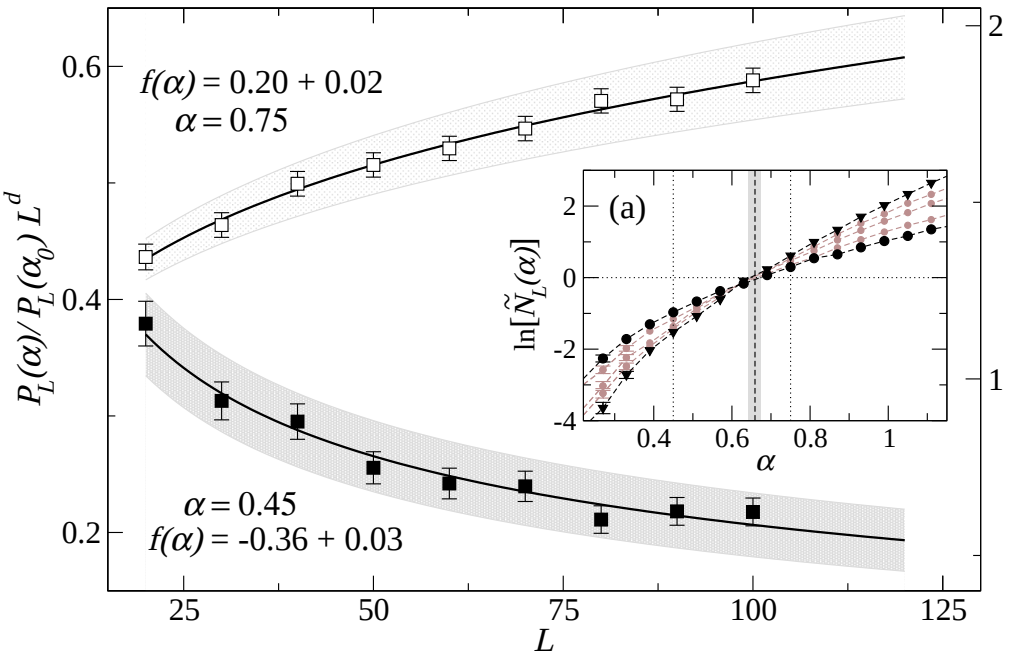

Figure 6.6: $\widetilde{N}_L(\alpha)$ vs L for $\alpha = 0.45$ (filled squares, left y axis) and 0.75 (open squares, right y axis). The solid lines are the $L^{f(\alpha)}$ curves where $f(\alpha)$ is obtained from the log-log linear fits of Eq. (6.4). The shaded regions mark the 66% c.i. of the $L^{f(\alpha)}$ values. The inset shows $\ln[\widetilde{N}_L(\alpha)]$ vs α for different L in the range [20 (black circle), 100 (black triangle)]. Standard deviations are within symbol size, whenever not shown. The vertical dashed line corresponds to the mean value of the crossing point $\alpha_- = 0.659 \pm 0.008$.

where $q_{2d} \equiv f'(\alpha)|_{\alpha=2d}$. The existence of a finite TP at $\alpha = 0$ requires $f(2d)$ and q_{2d} to be L-independent, for large enough L. In Fig. 6.7 we show the values of $f(2d)$ and q_{2d} obtained for different L. The value of $f(2d)$ seems to reach a saturation for large L although the numerical analysis cannot exclude a very slow decreasing tendency. A similar result is found for q_{2d}. Still larger L and more states are needed to decide the fate of $f(\alpha)$ at 0 and $2d$.

6.7 Summary

In this chapter, the probability density function (PDF) for critical wavefunction amplitudes is studied in the three-dimensional Anderson model. We have presented a

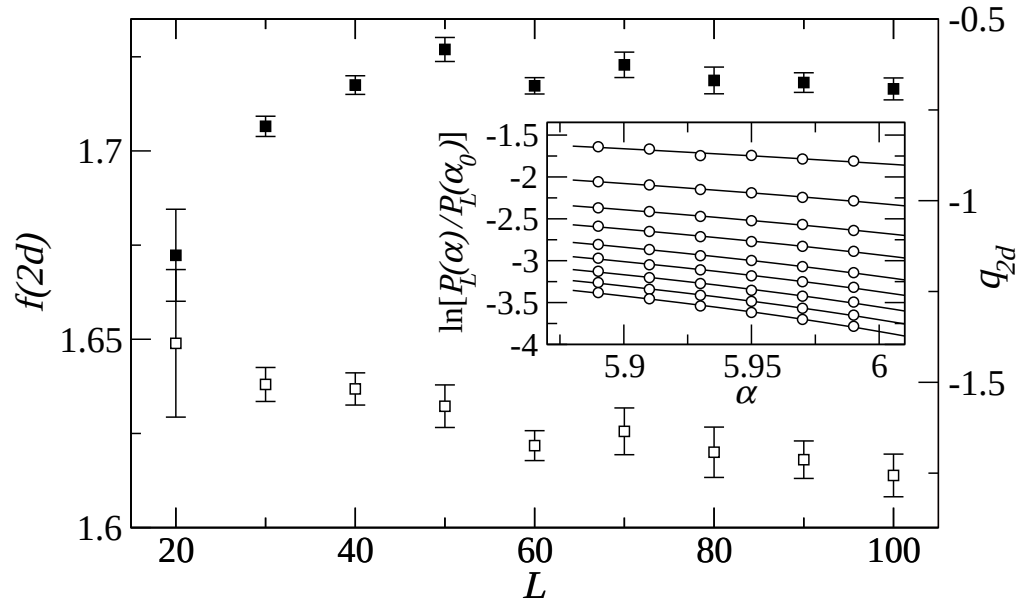

Figure 6.7: $f(2d)$ (filled squares, left y axis) and $q_{2d} \equiv f'(\alpha)|_{\alpha=2d}$ (open squares, right y axis) as functions of system size. The inset shows the fits of Eq. (6.8) for different L from 20 (top) to 100 (bottom). Standard deviations are within symbol size.

formal expression between the PDF and the multifractal spectrum $f(\alpha)$ in which the role of finite-size corrections is properly analyzed. We have shown the non-gaussian nature and the existence of a symmetry relation in the PDF. From the PDF, we extracted information about $f(\alpha)$ at criticality such as the presence of negative fractal dimensions and we commented on the possible existence of termination points. A PDF-based multifractal analysis is shown to be a valid alternative to the standard approach based on the scaling of inverse participation ratios.

Chapter 7

Finite Size Scaling of Multifractal Exponents

7.1 Finite Size Scaling Methodology

Near the metal to insulator transition, the only relevant length scale is the correlation length ξ (or the localization length in the insulating regime) which diverges as the state approaches the critical point. The one-parameter scaling theory states that a quantity $\mathcal{X}$ defining the critical transition such as the conductance g could be scaled by the correlation length in the thermodynamic limit $\xi_{L\to\infty}$ such that, in the vicinity of the critical point x_c, all $\mathcal{X}(L,x)$ from different sizes L with varying parameters x is described by only one scaling function $\mathcal{F}\left(\frac{L}{\xi}\right)$. The values of $\mathcal{X}$ is determined by parameters such as L, energy and disorder. These parameters change the value of $\mathcal{X}$ only through the one variable L/ξ. Furthemore the relation $\mathcal{X} = \mathcal{F}\left(\frac{L}{\xi}\right)$ enables the determination of the critical properties of the transition such as the critical disorder, mobility edge and critical exponent from finite size data. The values of the $\mathcal{X}(L,x)$ collapse onto the scaling function $\mathcal{F}\left(\frac{L}{\xi}\right)$ that has two branches if there is an MIT. These two branches correspond to the localised ($x > x_c$) and extended ($x < x_c$) phases.

From the first order approximation for the correlation length in Eq. (1.5), the scaling function could then be expressed as $\mathcal{F}(XL^{1/\nu})$ where the critical exponent ν defines the divergence of the correlation length near the critical point and $X = |\frac{x-x_c}{x_c}|$. Since $z = XL^{1/\nu} = 0$ at $x = x_c$, $\mathcal{F}$ can then be Taylor expanded around $x = x_c$. The scaling function then becomes

$$\mathcal{X} = \mathcal{X}_c + a_1 X L^{1/\nu} + a_2 X^2 L^{2/\nu} + \cdots , \tag{7.1}$$

where the first term $\mathcal{X}_c$ is the critical value at $x = x_c$. By fitting all the $\mathcal{X}(L, x)$ data points into the Taylor series expansion of $\mathcal{F}$, the transition point x_c and critical exponent ν can be numerically obtained as can be clearly seen from the preceding equation. If there is a transition then a plot of $\mathcal{X}(L, x)$ vs x will show a common crossing point x_c at which there is scale-invariance.

To properly estimate the values of the critical parameters of the transition, we use a set of fit functions which include two kinds of corrections to the universal scaling [66, 67], (i) nonlinearities of the x dependence of the scaling variables and (ii) an irrelevant scaling variable which accounts for a systematic shift with L of the transition point (i.e, crossing point in the plot of $\mathcal{X}(L, x)$ vs x). The first correction is due to the fact that when the range of x considered is broad then it is not correct anymore to assume a simple linear dependence in x of the scaling variables and nonlinearities in x must be taken into account. On the other hand, the shifting of x_c arises whenever there is a significant finite size effect whose contribution vanishes for large enough system sizes. Therefore, the scaling function including corrections to scaling is given by

$$\mathcal{X}(L, x) = \mathcal{F}(\chi_{\mathrm{r}} L^{1/\nu}, \chi_{\mathrm{i}} L^{y}), \tag{7.2}$$

where χ_{r} and χ_{i} are the relevant and leading irrelevant scaling fields, respectively. The exponent y in the irrelevant field is expected to be negative $y < 0$. Assuming the irrelevant scaling variable is well-behaved, the function can be Taylor expanded

in the second argument around $x = x_c$ up to the order n_i,

$$\mathcal{X}(L,x) = \sum_{n=0}^{n_{\rm i}} \chi_{\rm i}^n L^{ny} \mathcal{F}_n(\chi_{\rm r} L^{1/\nu}). \tag{7.3}$$

Moreover, each F_n is expanded in Taylor series up to the order n_r as

$$\mathcal{F}_n = \sum_{k=0}^{n_{\rm r}} a_{nk} \chi_{\rm r}^k L^{k/\nu}. \tag{7.4}$$

The absolute scales of the arguments of $\mathcal{F}$ in (7.2) is not defined. Hence, we set $a_{01} = a_{10} = 1$. Nonlinearities in the x-dependence of the scaling variables are taken into account by expanding $\chi_{\rm r}$ and $\chi_{\rm i}$ in terms of X up to order $m_{\rm r}$ and $m_{\rm i}$, respectively, such that

$$\chi_{\rm r}(X) = \sum_{m=1}^{m_{\rm r}} b_m X^m, \quad \chi_{\rm i}(X) = \sum_{m=0}^{m_{\rm i}} c_m X^m, \tag{7.5}$$

with $b_1 = c_0 = 1$. The expansions in the fit functions are carried out up to orders $n_{\rm i}, n_{\rm r}, m_{\rm r}, m_{\rm i}$ which are adjusted to the specific data and should be kept as low as possible, while giving the best fit to the data and FSS plot and minimizing the χ^2 values for the determination of critical parameters $W_{\rm c}$ and ν. The Levenberg-Marquardt method was used to perform the non-linear fit [26, 68]. We emphasize that the validity of the scaling results is determined by the goodness-of-fit parameter.

If there is a common crossing point x_c for the $\mathcal{X}(L,x)$ then the irrelevant correction is not necessary and we can set $n_i = m_i = 0$. Furthermore, by setting $n_r = m_r = 1$ and $n_i = m_i = 0$, a linear relation $\mathcal{X}(L,x) = a_{00} + a_{01} X L^{1/\nu}$ is obtained. In the presence of irrelevant scaling, the correct scaling behaviour is obtained by subtracting the irrelevant terms as

$$\mathcal{X}(L,x)_{\rm corrected} = \mathcal{X}(L,x) - \sum_{n=1}^{n_{\rm i}} \chi_{\rm i}^n L^{ny} \mathcal{F}_n(\chi_{\rm r} L^{1/\nu}). \tag{7.6}$$

The single-parameter scaling for $\mathcal{X}(L,x)_{\text{corrected}}$ becomes

$$\mathcal{X}(L,x)_{\text{corrected}} = \mathcal{F}_0\left(\pm\frac{L}{\xi}\right), \tag{7.7}$$

where the correlation length ξ is defined as

$$\xi = \mathcal{C}\chi_{\text{r}}(X)^{-\nu}. \tag{7.8}$$

Note that $\chi_{\text{r}}(X)$ may contain higher order terms in X. If there is no nonlinearity in x then a simple power law for ξ is recovered, that is $\xi = \mathcal{C}|\frac{x-x_c}{x_c}|^{-\nu}$ where $\mathcal{C}$ is a constant.

7.2 Scaling Laws for the Generalized Multifractal Exponents

We apply the finite-size scaling procedure to estimate the critical disorder W_c and critical exponent ν of the Anderson transition from the multifractal exponents which describe the complex distribution of the wavefunctions. Here, we consider wavefunctions in the vicinity of the band centre $E = 0$. By fixing the energy, it is the disorder that will drive the state into an Anderson transition. System sizes range from 20^3 to 100^3, and disorder values in the interval $W \in [15.0, 15.25, 15.5, \cdots, 18.0]$. For each size and disorder combination, we have taken at least 10000 uncorrelated states for a total of $1,530,000$ wave functions. Comparing to the averaging-over-many-samples interpretation [2] of the transfer matrix method (TMM), we can reinterpret this as a TMM bar of cross-sectional area, say, 100×100 with 10^6 TMM multiplications — something which is challenging even for TMM.

In this work, we propose a generalization of multifractal concepts of mass exponents and singularity strengths (Lipschitz-Hölder exponents) that is applicable to the *critical regime* and not just at the critical point. At criticality, in the thermo-

dynamic limit ($L \to \infty$), due to the multifractal nature of the states, the effective length scale is $\lambda \equiv \ell/L$ where ℓ and L are the box and system sizes respectively. The first quantity that we are considering are the generalized inverse participation ratios (gIPR) $\langle P_q \rangle$ (2.2) which are simply the sum of the moments of the wavefunction intensities $|\psi|^2$. We recall that at criticality it scales as $\langle P_q \rangle \underset{\lambda \to 0}{\propto} \lambda^{\tau_q}$, where the brackets denote average over disorder realizations. Away from the transition however, the moments will depend on the degree of disorder W, ℓ and L. Moreover, it follows from the scaling hypothesis that close to the transition, there exists a scaling function for $\langle P_q \rangle$ as given by [69]

$$\langle P_q \rangle = \mathcal{R}_q(L/\xi, \ell/\xi) \equiv \mathcal{R}_q(L/\xi, \lambda). \tag{7.9}$$

Since $\langle P_q \rangle = \langle \sum_{\text{all boxes}} \mu_k^q(\lambda) \rangle$ where $\mu_k(\lambda)$ is the box probability that reduces to $|\psi|^2$ for $\ell = 1$, it is clear to see that $\langle P_q \rangle$ changes with either ℓ, L and W. This explains the nature of the two-parameter scaling above and the natural consequence of λ being a scaling parameter is due to $\mathcal{R}_q(L/\xi, \ell/\xi) = \mathcal{R}_q(L/\xi, \lambda \cdot L/\xi)$. By writing the averaged moments in terms of the distribution function for the wavefunction amplitudes, we conclude that close to criticality we can write

$$\langle P_q \rangle (W, L, \lambda) = \lambda^{\tau_q} \mathcal{R}_q \left(L/\xi, \lambda \right), \tag{7.10}$$

where the dependence of the scaling function on λ may be non-trivial, in particular, it is likely to be non-analytic at $\lambda = 0$. Furthermore, Eq.(7.10) can be rearranged in the following form,

$$\widetilde{\tau}_q(W, L, \lambda) = \tau_q + \frac{q(q-1)}{\ln \lambda} \mathcal{T}_q \left(L/\xi, \lambda \right), \tag{7.11}$$

where the new scaling function $\mathcal{T}_q$ is related to the original $\mathcal{R}_q$ and we have defined a set of generalised mass exponents away from the transition as $\widetilde{\tau}_q(W, L, \lambda) \equiv$

$\ln\langle P_q\rangle/\ln\lambda$, which becomes the usual τ_q at the critical point (W_c), and in the limit $\lambda \to 0$. The factor $q(q-1)$ has been explicitly included to satisfy $\widetilde{\tau}_0 = \tau_0 = -d$ and $\widetilde{\tau}_1 = \tau_1 = 0$. That is the mass exponents corresponding to moments $q = 0, 1$ are constant for all disorder. From Eq.(7.11) it is straightforward to obtain the scaling law for the multifractal exponents,

$$\widetilde{\alpha}_q(W, L, \lambda) = \alpha_q + \frac{1}{\ln\lambda}\mathcal{A}_q\left(L/\xi, \lambda\right), \tag{7.12}$$

where the second term on the rhs will be non-zero for all q values, and the generalised exponents are defined as $\widetilde{\alpha}_q(W, L, \lambda)\alpha_q \equiv d\widetilde{\tau}_q/dq \equiv \langle\sum_k \mu_k^q \ln\mu_k\rangle/\left(\langle P_q\rangle \ln\lambda\right)$. Consequently, we can define a disorder, system size and box-size dependent generalised singularity spectrum around the critical point $\widetilde{f}_q \equiv q\widetilde{\alpha}_q - \widetilde{\tau}_q$, obeying

$$\widetilde{f}_q(W, L, \lambda) = f_q + \frac{q}{\ln\lambda}\mathcal{F}_q\left(L/\xi, \lambda\right). \tag{7.13}$$

This generalised multifractal spectrum can be related to the probability density function (PDF) for $\widetilde{\alpha} \equiv \ln\mu_k/\ln\lambda$ around the critical point as $\mathcal{P}(\widetilde{\alpha}; W, L, \lambda) \propto \lambda^{d-\widetilde{f}(\widetilde{\alpha};W,L,\lambda)}$, which as we approach the thermodynamic limit at the critical point becomes the usual relation $\mathcal{P}_\lambda(\alpha) \propto \lambda^{d-f(\alpha)}$ as discussed in chapter 6.

The generalization of the multifractal exponents for all moments suggests a wide range or even an infinite number of parameters from multifractal analysis than can be used to perform finite size scaling. Since the critical parameters are independent of q, the use of different moments provides a further test on the stability or confidence interval of the values of the critical parameters. However, the quality of numerical data for higher moments $|q|$ which are caused by either very small or anomalously large wavefunction amplitudes are not very reliable due to high numerical errors. Nevertheless, highly precise data could be found at $q = 0$ and around its vicinity. In particular the parameter $\widetilde{\alpha}_0$ could be estimated from the PDF of wavefunction intensities since it is the position of the maximum of the PDF for all

disorders. In the thermodynamic limit, the position of the maximum and α_0 should agree so we expect both to exhibit the same scaling behaviour, although for finite L that can be quantitatively different. At criticality as demonstrated in Chapter 6, it is the only scale invariant parameter of an L-dependent PDF. This alternative method might be attractive to experimentalists who can use measured PDF data to perform a finite size study [70, 71]. The maximum of the distribution was estimated by fitting the PDF to $\mathcal{P}(\alpha \equiv \frac{\ln \mu_k}{\ln \lambda}) \propto \lambda^{p(\alpha)}$ where $p(\alpha)$ is a polynomial such that $p(\alpha) = a_0 + \sum_{j\geq 2} a_j(\alpha - \alpha_0)^j$. α_0 is a parameter in the fit and it corresponds to the maximum of the PDF. The fit is performed for the PDF coming from 10 000 states for each set of values (W, L, ℓ). The order of the polynomial $p(\alpha)$ is chosen to maximize the goodness of fit for every case. To obtain a reliable estimate of the uncertainty σ_{α_0}, we carry out the fit 100 times for the 100 distributions obtained from subsets of 100 wavefunctions each for every set (W, L, ℓ).

7.3 Scaling at finite $\lambda = l/L$

To start with, we consider the simple case of fixed $\lambda = \ell/L$. Equations (7.11) and (7.12) reduce to a single parameter scaling $\mathcal{F}(L/\xi)$. Here, the function $\mathcal{F}(\chi_{\rm r} L^{1/\nu}, \chi_{\rm i} L^y)$ which represents the right hand side of Eqs. (7.11) and (7.12) is expanded to the first order of irrelevant scaling variable as $\mathcal{F}_0(\chi_{\rm r} L^{1/\nu}) + \chi_{\rm i} L^y \mathcal{F}_1(\chi_{\rm r} L^{1/\nu})$. As in section 7.1, the relevant $\chi_{\rm r}$ and irrelevant $\chi_{\rm i}$ parameters are expanded in $|\frac{W_c - W}{W_c}|$ up to orders $m_{\rm r}$ and $m_{\rm i}$. Note that each $\mathcal{F}_0$ and $\mathcal{F}_1$ is expanded in the relevant scaling field up to order n_0 or n_1 respectively.

In Table 7.1, we show representative results for 3 fits of $\widetilde{\tau}_q$ and 1 fit for $\widetilde{\alpha}_q$ at various λ and q values. Our results show that in all cases, we have acceptable goodness-of-fit and χ^2 values. The observed larger standard deviation of the critical paramaters for $q = 3$ is due to the fact that by considering higher moments the fluctuations in the wavefunction amplitudes are also enhanced. Hence the $\widetilde{\tau}_3$ points

meth.		q	λ	ν	W_c	N_D	N_P	χ^2	p	$n_0 n_1 m_\mathrm{r} m_\mathrm{i}$
τ	(7.11)	2	0.1	1.58 [.52, .66]	16.57 [.50, .61]	153	13	151	0.2	5130
	(7.11)	2	0.2	1.59 [.57, .61]	16.56 [.52, .58]	153	12	158	0.2	6020
	(7.11)	3	0.1	1.62 [.57, .66]	16.56 [.42, .61]	153	10	133	0.7	5010
α	PDF	0	0.1	1.56 [.54, .59]	16.53 [.49, .55]	153	10	131	0.7	3210

Table 7.1: The 95% confidence intervals of the critical exponent ν and the critical disorder W_c. The number of data is N_D, the number of parameters is N_P, χ^2 is the value of the chi-squared statistic for the best fit, and p is the goodness of fit probability. The orders of the expansions are specified in the last columns. The system sizes are $L = 20, 30, 40, 50, 60, 70, 80, 90, 100$ and λ is the ratio of the box size l to the system size L. The range of disorder is $W \in [15, 18]$. Where applicable, q specifies the moment of the wavefunction amplitude that was considered.

used for the fitting to obtain the critical parameters have a corresponding larger standard errors. In Figs. 7.1 and 7.2, we show the resulting fits together with the original high-precision $\widetilde{\tau}_q$ and $\widetilde{\alpha}_q$ data. From Fig. 7.1, it is obvious that the quality of the $\widetilde{\tau}_q$ data is comparable to the best TMM studies [67]. For all points in the plot, the standard deviation is within symbol size. There is evidently a large irrelevant shift of W_c upon increasing the system size. The tendency of $\widetilde{\tau}_2(W, L)$ can be clearly explained by inset B which shows the location of a critical τ_2 relative to the limiting boundaries of a pure metallic state where the slope is d and a strongly localised state $\tau_q = 0$. At $W < W_c$, increasing L means the system becomes more metallic and hence $\widetilde{\tau}_2$ slowly approaches the metallic limit, $\widetilde{\tau}_2 \to d(q-1)$. Whereas the opposite behaviour is seen for $W > W_c$ in which $\widetilde{\tau}_2$ becomes closer to the horizonal bound of the insulating case. A similar observation can be made for the $\widetilde{\alpha}_q$ data in Fig. 7.2. In the regime of extended states where the disorder is weak, $\widetilde{\alpha}_0$ approaches the metallic limit of $\alpha(W = 0, L) = 3$ upon increasing system size. Whereas in the localized region, $\widetilde{\alpha}_0$ increases with L. In the extreme case of $|\psi|^2 = 1$ at one site and zero elsewhere, $\alpha_0 \to \infty$. The results of Table 7.1 show that all fits give estimates of ν which (i) are consistent with each other, (ii) agree with the TMM results $\nu = 1.58 \pm 0.05$ [67] and $\nu = 1.62 \pm 0.07$ [26] and (iii) are significantly larger than 1 and, within the accuracy, different from 1.5 [72].

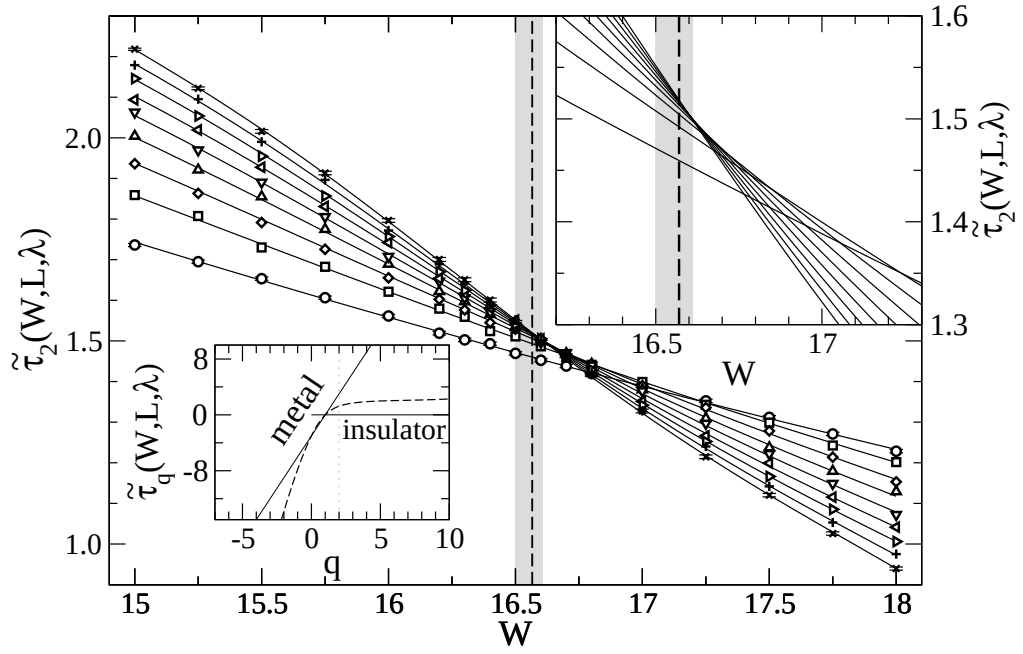

Figure 7.1: Plot of $\widetilde{\tau}_2$ at $E = 0$ and $\lambda = 0.1$ as a function of disorder at various system sizes $L = 20$ ($\circ$), 30 ($\Box$), ..., 100 ($\times$). The errorbars denote standard deviations obtained from averaging over disorder, they are within symbol size and shown for $L = 20$ and $L = 100$ only. The lines are plotted according to Eq. (7.11) for the finite-scaling scaling fit parameters as in the first row of Table 7.1. The vertical dashed line shows the estimated $W_c = 16.57$ and its confidence intervals are indicated by the grey region. Inset A shows the FSS functions (7.11) in an enlarged view of the critical region. Inset B shows the q-dependence of the mass exponents at criticality $\tau_q = D_q(q-1)$ (dashed line), pure metallic state $\tau_q = d(q-1)$ with a slope of d (thin line) and extremely localized state $\tau_q = 0$ (thin horizontal line). The grey dashed line marks $q = 2$.

7.4 Scaling with two parameters

The two-parameter scaling laws given in the previous section allow us to consider points of different λ altogether and fit them into one scaling function. The scaling function can be written in Taylor series as $\mathcal{F}(\chi_r \ell^{1/\nu}, \chi_r L^{1/\nu}) = A_0 + \frac{1}{\ln\lambda} \sum_{n=0}^{n_L} \sum_{k=0}^{n_\ell} a_{nk} \chi_r^n L^{n/\nu}\ \chi_r^k \ell^{k/\nu}$, where χ_r is as before. It is also possible to include irrelevant corrections to both ℓ- and L- scaling. For the present case, we have already obtained acceptable goodness-of-fit values even with the above function which has fewer parameters. Note that $\mathcal{F}$ represents the right hand side of Eq. (7.11) and (7.12). A

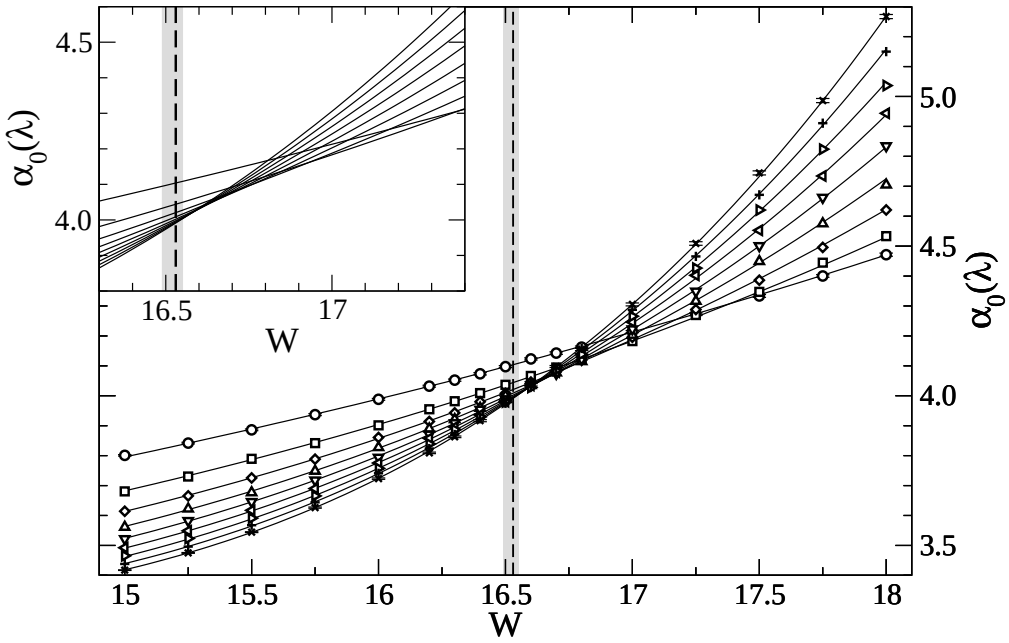

Figure 7.2: Plot of $\widetilde{\alpha}_0$ at $E = 0$ and $\lambda = 0.1$ as a function of disorder at various system sizes $L = 20$ (○), 30 (□), ..., 100 (×) as in Fig. 7.1. The errorbars denote standard deviations obtained from averaging over disorder. The lines are plotted according to Eq. (7.12) for the finite-size scaling fit parameters as in the last row of Table 7.1. The vertical dashed line shows the estimated $W_{\rm c} = 16.53$ and its confidence intervals are indicated by the grey region.

factor of $q(q-1)$ must be included in the second term of $\mathcal{F}$ for the scaling law of $\widetilde{\tau}_q$ as in Eq. (7.11). At the critical point and in the limit of $\lambda \to 0$, the zeroth order term should be $A_0 = \tau_q$ or α_q. Therefore in principle the two-parameter scaling in L and λ (or ℓ) also provides an estimation for the values of the critical multifractal exponents τ_q and α_q.

A representative scaling plot for $\widetilde{\tau}_2$ is shown in Fig. 7.3 along with the best estimates for the critical parameters which are in good agreement with the values given by the single-parameter scaling as listed in Table 7.1. The estimated values of the critical parameters with the 95% confidence interval for $n_{\rm L} = n_\ell = 3$ and $m_{\rm r} = 2$ are $W_c = 16.59\,[16.57, 16.60]$, $\nu = 1.58\,[1.55, 1.60]$ and $\tau_2 = 1.23\,[1.22, 1.24]$. The shaded surface is the two-parameter scaling function $\mathcal{F}(\chi_{\rm r}\ell^{1/\nu}, \chi_{\rm r}L^{1/\nu})$. The estimation of the correlation length is $\xi = \chi_{\rm r}^{-\nu}$ where $\chi_{\rm r}$ is a series expansion in

$|\frac{W-W_c}{W_c}|$ to an acceptable order as previously defined. The $\widetilde{\tau}_2$ points corresponding to disorder $W < W_c$ all lie on the extended (upper) sheet. The lower sheet is the localised area where all the $\widetilde{\tau}_2(W > W_c, L, \ell)$ populate. The existence of the two sheets of $\mathcal{F}$ is an indicaton of an MIT. Each slice of the surface corresponds to a fixed λ.

The large statistics involved for a two-parameter scaling that considers points of different λ give a better estimation of the critical parameters. However, we may have data points corresponding to different ℓ but taken from the same system size L. Points like these have a certain degree of correlations that our error estimations so far have not taken into account. Here, we recount the steps necessary to include such correlations in the data for a proper error analysis. We consider N number of random variate $\langle P(i)\rangle$ for the fitting. Each $\langle P(i)\rangle$ is the sample mean of a set of M random realizations. That is $\langle P(i)\rangle = \sum_{m=1}^{M} P_m(i)/M$. The definition of the χ^2 statistics which is the weighted sum of the square of the residuals is given as $\chi^2 = V^T C^{-1} V$. Here, the column vector $V = \{\langle P(1)\rangle - \mathcal{F}, \langle P(2)\rangle - \mathcal{F}, \cdots, \langle P(N)\rangle - \mathcal{F}\}$ and $\mathcal{F}$ is the model fit. Each element in the $N \times N$ covariance matrix is computed as $C_{ij} = \frac{1}{N}\frac{1}{M}\sum_{m=1}^{M}[P_m(i) - \langle P(i)\rangle][P_m(j) - \langle P(j)\rangle]$. Note that C_{ij} gives the degree of correlation between points $\langle P(i)\rangle$ and $\langle P(j)\rangle$. If the data are uncorrelated, C reduces to a diagonal matrix with zero off-diagonal elements. For correlated data, the C_{ij}'s are nonzero and will generally have the same order of magnitude with C_{ii}. The parameters in the model are determined by minimizing χ^2. We use the Mathematica function FindMinimum for the minimization procedure. The parameter errors are estimated by using a Monte Carlo process that generates a new synthetic data set where each $\langle P(i)\rangle$ is randomly drawn from a Gaussian distribution as defined by the mean and standard deviation of $P(i)$, that is within the confidence interval of $\langle P(i)\rangle$. From each Monte Carlo data set, a set of parameters is determined. The whole process is repeated so that a distribution is obtained for each of the parameter. The error for each parameter is the standard deviation of the corresponding distribution.

Our statistical analysis have shown that there is insignificant correlations in our data such that the estimated values of the critical disorder and critical exponent obtained when correlations are taken into account are within the confidence intervals of the results for the uncorrelated case. The results of our numerical estimations taking into account correlations and higher order irrelevant corrections using $\langle P_2 \rangle$ as the scaling parameter are $W_c = 16.574 \pm 0.005$ and $\nu = 1.56 \pm 0.02$ for $\ell \geqslant 6$, $L \in [20, 100]$ and $\lambda \leqslant 1/3$. High precision numerical analyses are in currently in progress.

7.5 Summary

We have proposed a generalisation of multifractal concepts such as mass exponents, singularity strengths and the multifractal spectrum that is applicable to the critical *regime* and not just at the critical point. In particular, our generalisation enables MFA to be applied without knowing the exact position of the critical point in advance. In fact, an estimate of the position of the critical point is one of the results of the analysis. We have tested our method on the Anderson model of an electron in a disordered system. By combining MFA with FSS analysis we have estimated the critical exponent that describes the divergence of the localisation length. Our estimated values for the critical disorder and exponent are in excellent agreement with previous TMM calculations [67]. This resolves a long standing problem that the critical exponent estimated from exact diagonalization studies was significantly smaller than that computed using TMM [67].

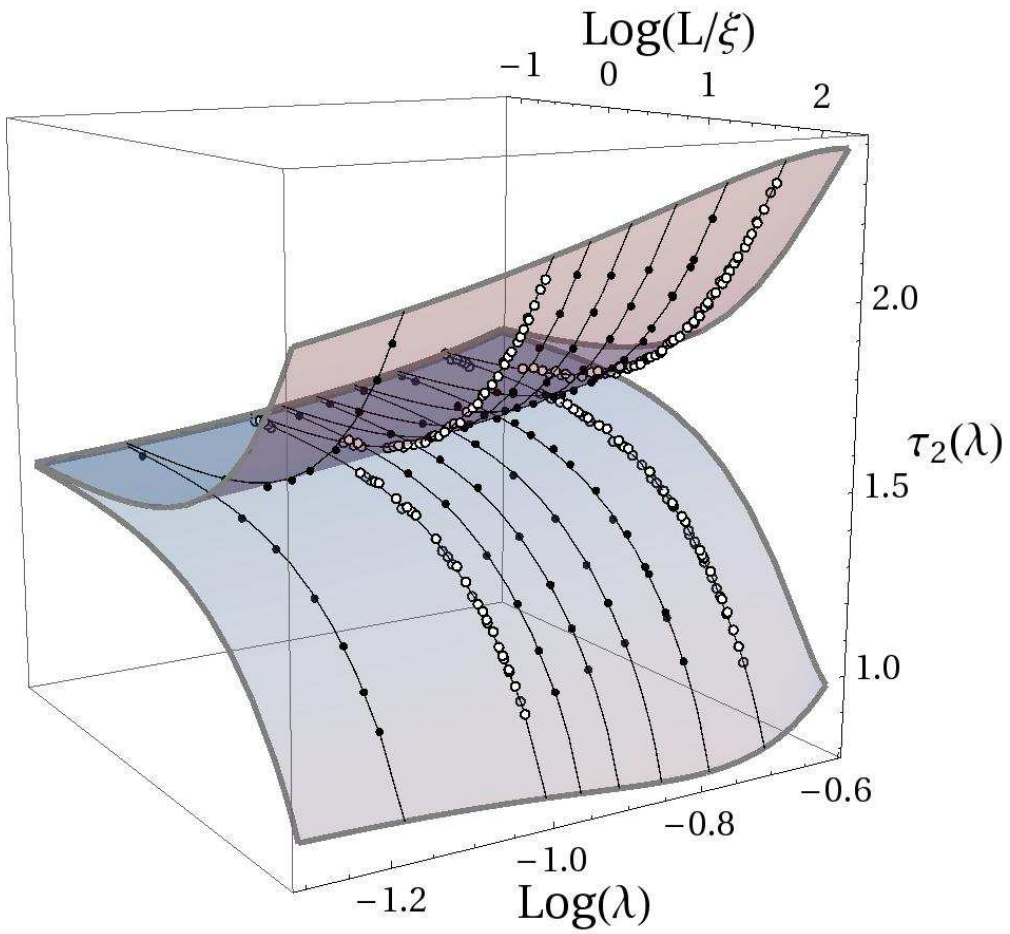

Figure 7.3: Finite-size scaling result for $\widetilde{\tau}_2(\lambda)$ at $E = 0$ when fitted according to Eq. (7.11) indicated by the shaded surface. The 285 points considered for the fit correspond to $W \in [15.25, 17.75]$, $L \in [30, 100]$, $\ell \in [6, L/5]$. The black lines on the surface highlight the different λ values: 1/15, 0.1 (∘), 1/9, 1/8, 1/7, 1/6, 0.2 (∘). The parameters obtained from the fit are $W_c = 16.59$, $\nu = 1.58$ in agreement with those listed in Table 7.1. The estimation for the mass exponent is $\tau_2 = 1.23$ which according to Eq. (7.11) corresponds to the extrapolation of $\widetilde{\tau}_2(\lambda)$ as $\lambda \to 0$. The goodness of fit is 0.09

Chapter 8

Conclusion

To summarize, the aim of this work has been a careful and systematic study on the multifractal characteristics of the electronic state at the critical point and in the critical regime within the Anderson model of localisation using high-precision data and very large system sizes. I hope to have demonstrated that the best strategy to obtain a complete picture of and to find better agreement with the proposed symmetry in the multifractal spectrum $f(\alpha)$ is to use system-size scaling with ensemble averaging in which to specifically consider a sensible range of system sizes with very large number of states. From the multifractal analysis, we have extracted information about critical properties of the Anderson transition such as the following: validity of the symmetry in the multifractal exponents and in the probability distribution function (PDF) of wavefunction intensities, existence of rare events, and estimations of the critical disorder and critical exponent. The multifractal analysis has also allowed us to comment and give speculations about the non-parabolicity of $f(\alpha)$ which is related to the non-Gaussian nature of the PDF and the possibility of termination points in the $f(\alpha)$. Lastly, this work has proposed an alternative method that is numerically simpler to obtain the multifractal spectrum from the PDF of wavefunction intensities.

In the following, we highlight the most important results of this work. Using

state of the art diagonalization technique for sparse matrices, we have reached very large system sizes of up to $L^3 = 240^3$ which corresponds to wavefunction sites of 1.4×10^7. The statistics involved in this work is unprecedented given the very large system sizes used. At the critical point, we have used $\sim 5 \times 10^4$ states for every $L \leqslant 100$ and ~ 100 states every for $L > 100$. For the FSS studies, in the critical regime corresponding to disorder values from 15 to 18, we have taken at least 10000 uncorrelated samples for each size $L \in [20, 30, \cdots, 100]$ and disorder combination, for a total of $1,530,000$ wave functions. Altogether, the total number of states considered in this work exceeds $2,200,000$. The huge statistics here have allowed us to reach regimes such as the tails and negative fractal dimensions of the multifractal spectrum that are highly sensitive to finite size effects and number of disorder realizations.

The study has given an in-depth and large scale analysis on the role of different averaging and the effect of system- and box- size scaling on the shape of the critical multifractal spectrum. The scaling approach is necessary to estimate the behaviour in the thermodynamic limit that is being reached faster by using system-size scaling. When considering states of varying L, different disorder realizations are taken into account and finite size effects are reduced. Due to the nature of typical average which is dominated by a single representative site, it has been shown here that an increase in disorder realizations will only change $f^{\text{typ}}(\alpha)$ up to a point but increasing L shifts $f^{\text{typ}}(\alpha)$ towards the left, i.e., towards lower values of α^{typ} and f^{typ}. On the other hand, the $f^{\text{ens}}(\alpha)$ obtained by ensemble averaging which considers contributions from all disorder realizations equally is shown to be heavily dependent on the number of samples taken. Furthermore, $f^{\text{ens}}(\alpha)$ gives a more complete profile of the spectrum because it contains information about negative fractal dimensions and shows contributions from the tails of the distribution. Both of which are lost when using typical averaging The study has demonstrated that for a fixed L, $f^{\text{ens}}(\alpha)$ reaches more negative values upon an increase in disorder realizations.

Since the region of the negative fractal dimensions is caused by the so-called rare events whose number decreases with L, an increase in L must be accompanied with an increase in the disorder realizations to reach the same extent of negative fractal dimensions.

This work is first to demonstrate the validity of a proposed symmetry relation in the multifractal exponents for the 3D Anderson Model within the orthogonal universality class. The statistical analyses have shown that the symmetry relation seems to hold in the thermodynamic limit since it is better satisfied whenever higher number of disorder realizations and larger system sizes are considered. Better agreement to the symmetry is found whenever $f(\alpha)$ reaches more negative values, α moves closer to zero and the right tail of $f(\alpha)$ satisfies the upper boundary of $\alpha \leq 2d$. The best method to satisfy the symmetry relation is to use system-size scaling with ensemble averaging that considers a sensible range of system sizes for which very large number of states can be obtained.

In pursuit of a numerical optimisation of the box-scaling technique, different box-partitioning schemes have been discussed including cubic and non-cubic boxes, use of periodic boundary conditions to enlarge the system, and implementation of single and multiple origins for the partitioning grid. The numerically most reliable method is to divide a system of linear size L equally into cubic boxes of size l for which L/l is an integer. This method is the least numerically expensive while having a good reliability.

An exact relation between the singularity spectrum and the probability density function of the wavefunction intensities is given which includes a size-dependent correction factor that must be taken into account. Using this relation, it has been demonstrated that $f(\alpha)$ can be obtained from the PDF and vice versa. Furthermore, it has been shown that the $f(\alpha)$ is the scale-invariant distribution at criticality. As a natural consequence of the symmetry in the $f(\alpha)$, the critical PDF has also been shown to obey a corresponding symmetry relation.

Using a generalization in the definition of multifractal exponents that is applicable to the critical regime and not just at the critical point, the study has proposed scaling laws for generalized mass exponents $\widetilde{\tau}_q$, singularity strength $\widetilde{\alpha_q}$ and singularity spectrum $\widetilde{f}_q$. Using single- and two-parameter scaling with FSS analysis, the location of the critical point and critical exponents have been estimated that are in excellent agreement with previous transfer matrix calculations. The results presented here resolve the long-standing issue of systematically smaller exponents found in previous results based on exact diagonalization [73–76].

Appendix A

Symmetry Relation in the Generalized Dimensions

The symmetry relation for the anomalous scaling exponents $\Delta_1 = \Delta_{1-q}$ [43] can be written in terms of the generalised fractal dimensions $D_q \equiv d + \Delta_q/(q-1)$ as,

$$D_q(q-1) + qD_{1-q} = (2q-1)d. \tag{A.1}$$

For $q > 1/2$ then it follows,

$$\begin{aligned} D_0 &= d, \quad q = 1, \\ D_2 + 2D_{-1} &= 3d, \quad q = 2, \\ 2D_3 + 3D_{-2} &= 5d, \quad q = 3, \\ 3D_4 + 4D_{-3} &= 7d, \quad q = 4, \\ &\dots \end{aligned}$$

In Fig. A.1 we show the numerical evaluation of the symmetry relation in terms of D_q. If the symmetry were perfectly obeyed by our data, all data points should lie on the q-axis. As can be seen in the figure, we can roughly conclude that for $q \leqslant 2$ the

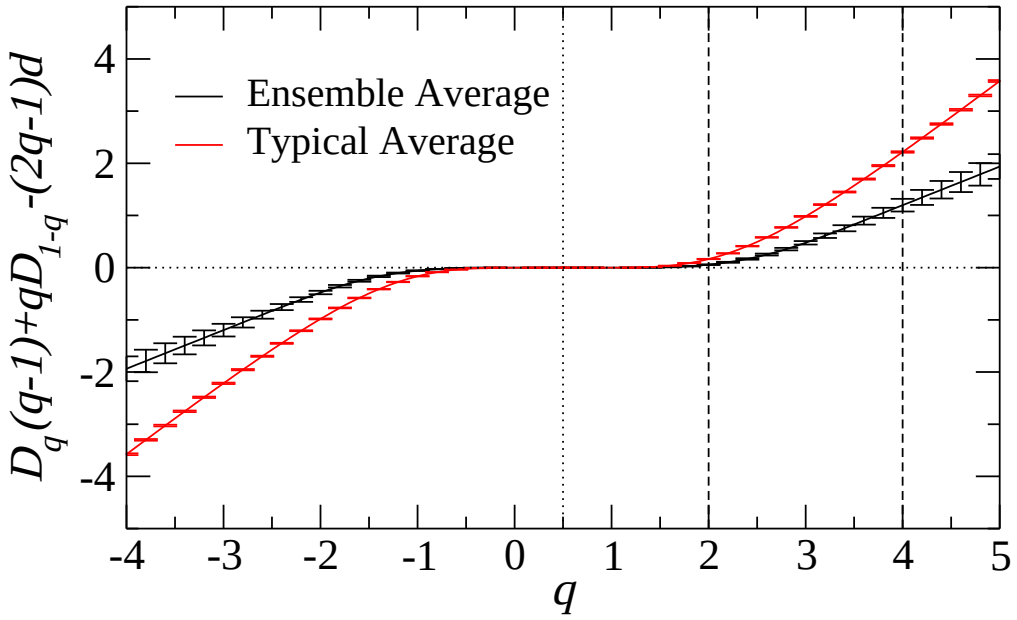

Figure A.1: Symmetry relation for the generalised fractal dimensions at the 3-D Anderson model. Data were obtained doing system-size scaling with $L \in [20, 100]$ and 2.5×10^4 critical states for each size. Error bars denote standard deviations.

symmetry is well satisfied and so the numerical values for D_q are not expected to change much when larger system sizes are considered for the analysis. However for $q > 2$ the deviation from the symmetry relation is noticeable and so the numerical values of D_q still differ from the ones corresponding to the thermodynamic limit.

The numerical values of D_q are listed in Table A.1. The standard deviation of the values must be interpreted as a measure of the uncertainty in terms of the number of critical states considered, and not as an absolute error for the value in the thermodynamic limit. In other words, when considering larger system sizes, some values of D_q (those for which the symmetry is not satisfied) will change much more than the standard deviation listed in the table. According to Fig. A.1, the ensemble average gives a better agreement with the symmetry relation and so the values D_q^{ens} are more reliable than those from typical average. On the other hand, as shown in Fig. A.2, the value $q = 4$ already belongs to the region of negative fractal dimensions, and so it means that the value of D_4 obtained from typical average

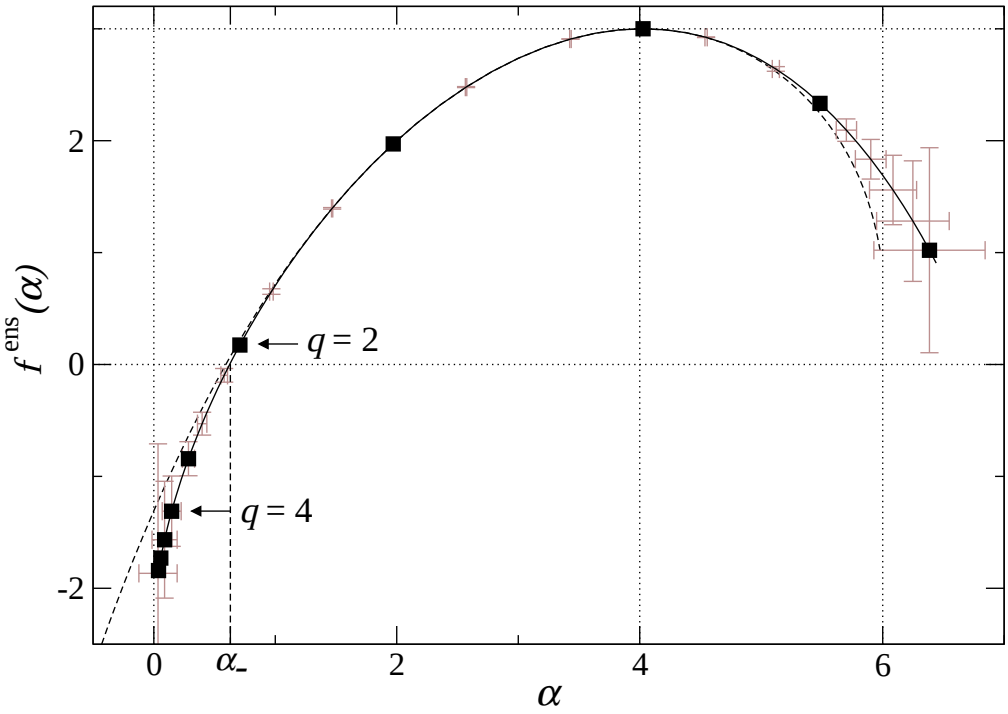

Figure A.2: Multifractal spectrum obtained using ensemble average as in chapter 4. Filled symbols mark the position of the points corresponding to integer values for q.

must be different than that obtained from ensemble average. As suggested by figure Fig. A.2 the positive left branch of the $f(\alpha)$ is described with q from 0 to values slightly higher than 2, explicitly $q_c \simeq 2.1 - 2.2$, and so we should have $D_q^{\rm typ} = D_q^{\rm ens}$ for $q < q_c$, since in the thermodynamic limit both averages must give the same result in the positive region of the spectrum.

A.1 Ensemble average

For $D_2^{\rm ens}$ and $D_4^{\rm ens}$ the values $D_2^{\rm ens} = 1.24 \pm 0.07$ and $D_4^{\rm ens} = 0.63 \pm 0.2$ seem reasonable estimates. Here were are using for the error in D_2 the difference between ensemble and typical average values, i.e. $(1.35361 - 1.24296)/2 = 0.055 \sim 0.06$ plus ~ 0.01 from their standard error, hence the total error is about 0.07. For D_4, we cannot use the typical value as explained above, but from the D_2 calculation, we note that the true error is about an order of magnitude larger, thus we have

$10 \cdot 0.015 \simeq 0.2$. We have checked that using these error bars the symmetry relation is satisfied within the uncertainty interval. Therefore these values seem appropriate to check relations involving D_2 and D_4.

A.2 Typical average

On the other hand for typical average the situation is different, since the scaling of the typical moments for high q will be highly affected by finite size effects. This can be noticed in the difference values obtained for $D_2^{\rm typ}$ and $D_2^{\rm ens}$, which must be equal in the thermodynamic limit. Since finite size effects are less enhanced in the ensemble average we consider the value of $D_2^{\rm ens}$ to be more correct. However, for $q > q_c$ the D_q from typical and ensemble average must differ, and again $D_q^{\rm typ}$ will converge very slowly to their values in the thermodynamic limit. We know that for the exponents $\tau(q)$ we have $\tau^{\rm typ}(q) = \tau^{\rm ens}(q)$ for $q < q_c$ and they differ for $q > q_c$ where the typical is simply given by $\tau^{\rm typ}(q) = q\alpha_-$, where α_- is the crossing point $f(\alpha_-) = 0$ [Fig. A.2] which in the thermodynamic limit must be the same for ensemble (crossing to negative dimensions) and typical averages (end of the spectrum). Then it means than for $q > q_c$ the generalized fractal dimensions from typical average are given by

$$D_q^{\rm typ} = \frac{q}{q-1}\alpha_-. \tag{A.2}$$

We could use this expression to estimate $D_q^{\rm typ}$ using the α_- that we can calculate from the $f(\alpha)$ obtained from ensemble average, which is less affected by system size effects. We have $\alpha_- = 0.63 \pm 0.03$ and thus for $q = 4$ it means according to Eq. (A.2) that in the thermodynamic limit $D_4^{\rm typ} = 0.84 \pm 0.04$. The value obtained from the scaling, listed in the table, $D_4^{\rm typ} = 1.02$ is still far form the previous value. For $q > q_c$ the values of $D_q^{\rm typ}$ are strongly affected by finite-size effects and they must converge to those given by Eq. (A.2). The convergence is very slowly and so they will always

be dependent on the range of system-sizes used in the analysis. So Eq. (A.2) could a give a good approximation of the dimensions under typical average for $q > q_c$. It must also be emphasized that for the typical average the symmetry relation for the multifractal spectrum and in particular Eq. (A.1) does not hold for $q > q_c$.

ENSEMBLE AVERAGE		
q	D_q^{ens}	$\sigma_{D_q^{\text{ens}}}$
0.00000	3.00000	0.00000
0.10000	2.89638	0.00017
0.20000	2.79126	0.00036
0.30000	2.68520	0.00055
0.40000	2.57880	0.00075
0.50000	2.47276	0.00097
0.60000	2.36778	0.00119
0.70000	2.26456	0.00142
0.80000	2.16370	0.00167
0.90000	2.06575	0.00193
1.10000	1.88019	0.00250
1.20000	1.79314	0.00281
1.30000	1.71014	0.00314
1.40000	1.63128	0.00350
1.50000	1.55658	0.00429
1.60000	1.48601	0.00429
1.70000	1.41949	0.00472
1.80000	1.35691	0.00517
1.90000	1.29813	0.00565
2.00000	**1.24296**	**0.00614**
2.10000	1.19125	0.00664
2.20000	1.14279	0.00716
2.30000	1.09738	0.00768
2.40000	1.05485	0.00820
2.50000	1.01499	0.00872
2.60000	0.97763	0.00924
2.70000	0.94260	0.00975
2.80000	0.90971	0.01026
2.90000	0.87884	0.01076
3.00000	0.84981	0.01124
3.10000	0.82252	0.01171
3.20000	0.79681	0.01217
3.30000	0.77259	0.01262
3.40000	0.74974	0.01305
3.50000	0.72817	0.01346
3.60000	0.70777	0.01387
3.70000	0.68847	0.01426
3.80000	0.67020	0.01463
3.90000	0.65287	0.01534
4.00000	**0.63642**	**0.01534**

TYPICAL AVERAGE		
q	D_q^{typ}	$\sigma_{D_q^{\text{typ}}}$
0.00000	3.00000	0.00000
0.10000	2.89639	0.00018
0.20000	2.79130	0.00037
0.30000	2.68523	0.00058
0.40000	2.57877	0.00080
0.50000	2.47256	0.00104
0.60000	2.36729	0.00128
0.70000	2.26368	0.00153
0.80000	2.16254	0.00177
0.90000	2.06473	0.00200
1.10000	1.88262	0.00239
1.20000	1.79989	0.00255
1.30000	1.72341	0.00268
1.40000	1.65336	0.00279
1.50000	1.58967	0.00288
1.60000	1.53207	0.00295
1.70000	1.48016	0.00300
1.80000	1.43344	0.00305
1.90000	1.39143	0.00308
2.00000	**1.35361**	**0.00310**
2.10000	1.31953	0.00312
2.20000	1.28876	0.00313
2.30000	1.26091	0.00313
2.40000	1.23563	0.00314
2.50000	1.21264	0.00314
2.60000	1.19166	0.00314
2.70000	1.17247	0.00313
2.80000	1.15487	0.00313
2.90000	1.13868	0.00313
3.00000	1.12375	0.00312
3.10000	1.10994	0.00311
3.20000	1.09715	0.00311
3.30000	1.08527	0.00310
3.40000	1.07421	0.00309
3.50000	1.06390	0.00308
3.60000	1.05425	0.00308
3.70000	1.04522	0.00306
3.80000	1.03675	0.00306
3.90000	1.02878	0.00305
4.00000	**1.02128**	**0.00305**

Table A.1: D_q values for ENSEMBLE(left) and TYPICAL(right) AVERAGE. Obtained from system-size scaling $L \in [20, 100]$ with 2.5×10^4 critical states for each L

Bibliography

[1] P. W. Anderson. Absence of diffusion in certain random lattices. *Phys. Rev.*, 109:1492–1505, 1958.

[2] B. Kramer and A. MacKinnon. Localization: theory and experiment. *Rep. Prog. Phys.*, 56:1469–1564, 1993.

[3] Ferdinand Evers and Alexander D. Mirlin. Anderson transitions. *Rev. Mod. Phys.*, 80:1355–1417, 2008.

[4] T. Brandes and S. Kettemann (eds). *The Anderson Transition and its Ramifications — Localisation, Quantum Interference, and Interactions*. Springer, 2003.

[5] R. Dalichaouch, J. P. Armstrong, S. Schultz, P. M. Platzman, and S. L. McCall. Microwave localization by two-dimensional random scattering. *Nature*, 354:53–55, 1991.

[6] H. Hu, A. Strybulevych, J. H. Page, S. E. Skipetrov, and B. A. Van Tiggelen. Localization of ultrasound in a three-dimensional elastic network. *Nature Physics*, 4:945–948, 2008.

[7] S. Faez, A. Strybulevych, J. H. Page, A. Lagendijk, and B. A. van Tiggelen. Observation of multifractality in anderson localization of ultrasound. *Phys. Rev. Lett.*, 103:155703, 2009.

[8] D. S. Wiersma, P. Bartolini, A. Lagendjik, and R. Righini. Localization of light in a disordered medium. *Nature*, 390:671–673, 1997.

[9] Shayan Mookherjea, Jung S. Park, Shun-Hui Yang, and Prabhakar R. Bandaru. Localization in silicon nanophotonic slow-light waveguides. *Nature Photonics*, 2:90–93, 2008.

[10] K. Hashimoto, C. Sohrmann, M. Morgenstern, T. Inaoka, J. Wiebe, R. A. Römer, Y. Hirayama, and R. Wiesendanger. The transition from localized to extended states observed in real space. *Phys. Rev. Lett.*, 2008. arXiv: cond-mat/0807.3784.

[11] Anthony Richardella, Pedram Roushan, Shawn Mack, Brian Zhou, David A. Huse, David D. Awschalom, and Ali Yazdani. Visualizing critical correlations near the metal-insulator transition in $Ga_1{-}xMn_{xAs}$. *Science*, 327(5966):665–669, 2010.

[12] Giacomo Roati, Chiara D'Errico, Leonardo Fallani, Marco Fattori, Chiara Fort, Matteo Zaccanti, Giovanni Modugno, Michele Modugno, and Massimo Inguscio. Anderson localization of a non-interacting bose-einstein condensate. *Nature*, 453:895–899, 2008.

[13] Juliette Billy, Vincent Josse, Zhanchun Zuo, Alain Bernard, Ben Hambrecht, Pierre Lugan, David Clement, Laurent Sanchez-Palencia, Philippe Bouyer, and Alain Aspect. Direct observation of Anderson localization of matter waves in a controlled disorder. *Nature*, 453:891–894, 2008.

[14] Gerd Bergmann. Physical interpretation of weak localization: A time-of-flight experiment with conduction electrons. *Phys. Rev. B*, 28:2914–2920, 1983.

[15] G. Bergmann. Weak localization in thin films, a time-of-flight experiment with conduction electrons. *Phys. Rep.*, 107:1–58, 1984.

[16] E. Abrahams, P. W. Anderson, D. C. Licciardello, and T. V. Ramakrishnan. Scaling theory of localization: absence of quantum diffusion in two dimensions. *Phys. Rev. Lett.*, 42:673–676, 1979.

[17] A. MacKinnon and B. Kramer. One-parameter scaling of localization length and conductance in disordered systems. *Phys. Rev. Lett.*, 47:1546–1549, 1981.

[18] A. MacKinnon and B. Kramer. The scaling theory of electrons in disordered solids: additional numerical results. *Z. Phys. B*, 53:1–13, 1983.

[19] D. J. Thouless. Electrons in disordered systems and the theory of localization. *Phys. Rep.*, 13:93–142, 1974.

[20] J. L. Cardy. In C. Domb and J. L. Lebowitz, editors, *Phase Transitions and Critical Phenomena*, volume 11, New York, 1987. Academic.

[21] D. Belitz and T. R. Kirkpatrick. The Anderson-Mott transition. *Rev. Mod. Phys.*, 66:261–380, 1994.

[22] R. A. Römer and M. Schreiber. *The Anderson Transition and its Ramifications — Localisation, Quantum Interference, and Interactions*, volume 630 of *Lecture Notes in Physics*, chapter Numerical investigations of scaling at the Anderson transition, pages 3–19. Springer, Berlin, 2003.

[23] K. Slevin, P. Markoš, and T. Ohtsuki. Scaling of the conductande distribution near the Anderson transition. *Phys. Rev. B*, 67:155106, Apr 2003.

[24] K. Slevin, P. Markoš, and T. Ohtsuki. Reconciling conductance fluctuations and the scaling theory of localization. *Phys. Rev. Lett.*, 86:3594–3597, 2001.

[25] T. Ohtsuki, K. Slevin, and T. Kawarabayashi. Review on recent progress on numerical studies of the Anderson transition. *Ann. Phys. (Leipzig)*, 8:655–664, 1999. ArXiv: cond-mat/9911213.

[26] F. Milde, R. A. Römer, M. Schreiber, and V. Uski. Critical properties of the metal-insulator transition in anisotropic systems. *Eur. Phys. J. B*, 15:685–690, 2000. ArXiv: cond-mat/9911029.

[27] M. Bollhöfer and Y. Notay. Jadamilu: a software code for computing selected eigenvalues of large sparse symmetric matrices. *Comp. Phys. Comm.*, 177:951–964, 2007.

[28] O. Schenk, M. Bollhöfer, and R. Römer. On large scale diagonalization techniques for the anderson model of localization. *SIAM Journal of Sci. Comp.*, 28:963, 2006.

[29] B. Mandelbrot. *The Fractal Geometry of Nature*. W. H. Freeman, New York, 1982.

[30] J. Feder. *Fractals*. Plenum Press, New York, 1988.

[31] K.J. Falconer. *The geometry of fractal sets*. Cambridge University Press, 1985.

[32] T. Nakayama and K. Yakubo. *Fractal Concepts in Condensed Matter Physics*, volume 140 of *Springer Series in Solid State Sciences*. Springer, 2003.

[33] A. B. Chabra and R. V. Jensen. Direct determination of the $f(\alpha)$ singularity spectrum. *Phys. Rev. Lett.*, 62:1327–1330, 1989.

[34] H. Aoki. Critical behaviour of extended states in disordered systems. *J. Phys. C*, 16:L205–208, 1983.

[35] H. Aoki. Fractal dimensionality of wave functions at the mobility edge: Quantum fractal in the Landau levels. *Phys. Rev. B*, 33:7310–7313, 1986.

[36] M. Schreiber and H. Grussbach. Multifractal wave functions at the Anderson transition. *Phys. Rev. Lett.*, 67:607–610, 1991.

[37] V. I. Fal'ko and K. B. Efetov. Multifractality: Generic property of eigenstates of 2d disordered metals. *Europhys. Lett.*, 32:627, 1995.

[38] M. Janssen. Multifractal analysis of broadly-distributed observables at criticality. *Int. J. Mod. Phys. B*, 8:943, 1994.

[39] F. Evers, A. Mildenberg, and A. D. Mirlin. Quantum hall effects in normal and superconducting systems: localization and multifractality. *Phys. Stat. Sol. b*, 245:284, 2008.

[40] F. Wegner. Four-loop-order beta-function of nonlinear sigma-models in symmetric spaces. *Nucl. Phys. B*, 316:663–678, 1989.

[41] A. W. W. Ludwig, M. P. A. Fisher, R. Shankar, and G. Grinstein. Integer quantum Hall transition: An alternative approach and exact results. *Phys. Rev. B*, 50:7526, 1994.

[42] H. Obuse, A. R. Subramaniam, A. Furusaki, I. A. Gruzberg, and A. W. W. Ludwig. Boundary multifractality at the integer quantum Hall plateau transition: implications for the critical theory. *Phys. Rev. Lett.*, 101:116802, Sep 2008.

[43] A. D. Mirlin, Y. V. Fyodorov, A. Mildenberger, and F. Evers. Exact relations between multifractal exponents at the anderson transition. *Phys. Rev. Lett.*, 97:046803, 2006.

[44] A.D. Mirlin and Y.F. Fyodorov. Distribution of local densities of states, order parameter function and critical behavior near the anderson transition. *Phys. Rev. Lett.*, 72:526, 1994.

[45] Y. V. Fyodorov and D. V. Savin. Statistics of impedance, local density of states, and reflection in quantum chaotic systems with absorption. *JETP Letters*, 80:725, 2004.

[46] D. V. Savin, H. J. Sommers, and Y. V. Fyodorov. Universal statistics of the local greens function in wave chaotic systems with absorption. *JETP Letters*, 82:544, 2005.

[47] H. Obuse, A. R. Subramaniam, A. Furusaki, I. A. Gruzberg, and A. W. W. Ludwig. Multifractality and conformal invariance at 2d metal-insulator transition in the spin-orbit symmetry class. *Phys. Rev. Lett.*, 98:156802, 2007.

[48] A. Mildenberger and F. Evers. Wave function statistics at the symplectic two-dimensional anderson transition: Bulk properties. *Phys. Rev. B*, 75:041303, 2007.

[49] A. D. Mirlin and F. Evers. Multifractality and critical fluctuations at the Anderson transition. *Phys. Rev. B*, 62:7920, 2000.

[50] F. Evers and A. D. Mirlin. Fluctuations of the inverse partcipation ratio at the Anderson transition. *Phys. Rev. Lett.*, 84:3690–3693, 2000.

[51] F. Evers, A. Mildenberger, and A. D. Mirlin. Multifractality of wave functions at the quantum hall transition revisited. *Phys. Rev. B*, 64:241303, 2001.

[52] Matthew S. Foster, Shinsei Ryu, and Andreas W. W. Ludwig. Termination of typical wave-function multifractal spectra at the anderson metal-insulator transition: Field theory description using the functional renormalization group. *Phys. Rev. B*, 80:075101, 2009.

[53] Alberto Rodriguez, Louella J. Vasquez, and Rudolf A. Römer. Multifractal analysis of critical states in the 3d anderson model: different strategies for box-partitioning method. *Eur. Phys. J. B*, 2008.

[54] F. Milde, R. A. Römer, and M. Schreiber. Multifractal analysis of the metal-insulator transition in anisotropic systems. *Phys. Rev. B*, 55:9463–9469, 1997.

[55] H. Grussbach and M. Schreiber. Determination of the mobility edge in the Anderson model of localization in three dimensions by multifractal analysis. *Phys. Rev. B*, 51:663–666, 1995.

[56] U. Elsner, V. Mehrmann, F. Milde, R. A. Römer, and M. Schreiber. The Anderson model of localization: a challenge for modern eigenvalue methods. *SIAM J. Sci. Comp.*, 20:2089–2102, 1999. ArXiv: physics/9802009.

[57] I. K. Zharekeshev and B. Kramer. Advanced lanczos diagonalization for models of quantum disordered systems. *Comp. Phys. Comm.*, 121–122:502–504, 1999.

[58] M. Schreiber, F. Milde, R. A. Römer, U. Elsner, and V. Mehrmann. Electronic states in the Anderson model of localization: benchmarking eigenvalue algorithms. *Comp. Phys. Comm.*, 121–122 (1–3):517–523, 1999.

[59] Ashvin B. Chhabra and K. R. Sreenivasan. Negative dimensions: Theory, computation, and experiment. *Phys. Rev. A*, 43:1114–1117, 1991.

[60] M. Yamaguti and C. P. C. Prado. Smart covering for a box-counting algorithm. *Phys. Rev. E*, 55(6):7726–7732, 1997.

[61] P. Kestener and A. Arneodo. Three-dimensional wavelet-based multifratal method: the need for revisiting the multifractal description of turbulence dissipation data. *Phys. Rev. Lett.*, 91(19):194501, Nov 2003.

[62] E. Cuevas. $f(\alpha)$ multifractal spectrum at strong and weak disorder. *Phys. Rev. B*, 68:024206, 2003.

[63] M. A. Lebyodkin and T. A. Lebedkina. Multifractality and randomness in the unstable plastic flow near the lower strain-rate boundary of instability. *Phys. Rev. E*, 77:026111, 2008.

[64] M. Morgenstern, J. Klijn, C. Meyer, M. Getzlaff, R. Adelung, R. A. Römer, K. Rossnagel, L. Kipp, M. Sibowski, and R. Wiesendanger. Direct comparison between potential landscape and local density of states in a disordered two-dimensional electron system. *Phys. Rev. Lett.*, 89:136806–4, 2002. ArXiv: cond-mat/0202239.

[65] M. Morgenstern, J. Klijn, Chr. Meyer, and R. Wiesendanger. Real-space observation of drift states in a two-dimensional electron system at high magnetic fields. *Phys. Rev. Lett.*, 90(5):056804, 2003.

[66] J. L. Cardy. *Scaling and Renormalization in Statistical Physics.* Cambridge University Press, Cambridge, 1996.

[67] K. Slevin and T. Ohtsuki. Corrections to scaling at the Anderson transition. *Phys. Rev. Lett.*, 82:382–385, 1999. ArXiv: cond-mat/9812065.

[68] W. H. Press, B. P. Flannery, S. A. Teukolsky, and W. T. Vetterling. *Numerical Recipes in FORTRAN.* Cambridge University Press, Cambridge, 2nd edition, 1992.

[69] K. Yakubo and M. Ono. Finite-size scaling of multifractal wave functions: The metal-insulator transition in two-dimensional symplectic systems. *Phys. Rev. B*, 58:9767, 1998.

[70] Julien Chabé, Gabriel Lemarié, Jean Claude Garreau, Dominique Delande, Pascal Szriftgiser, and Benoit Grémaud. Experimental observation of the anderson metal-insulator transition with atomic matter waves. *Phys. Rev. Lett.*, 101:255702, 2008.

[71] Gabriel Lemarié, Julien Chabé, Pascal Szriftgiser, Jean Claude Garreauand, Benoit Grémaud, and Dominique Delande. Observation of the anderson metal-insulator transition with atomic matter waves: Theory and experiment. *Phys. Rev. A*, 80:043626, 2009.

[72] Antonio M. García-García. Semiclassical theory of the anderson transition. *Phys. Rev. Lett.*, 100(7):076404, 2008.

[73] I. K. Zharekeshev and B. Kramer. Asymptotics of universal probability of neighboring level spacings at the Anderson transition. *Phys. Rev. Lett.*, 79:717–720, 1997. ArXiv: cond-mat/9706255.

[74] E. Hofstetter. Disordered systems and the metal-insulator transition: A super universality class. *Phys. Rev. B*, 57:12763–12767, 1998. ArXiv: cond-mat/9611060.

[75] F. Milde, R. A. Römer, and M. Schreiber. Energy-level statistics at the metal-insulator transition in anisotropic systems. *Phys. Rev. B*, 61:6028–6035, 2000. ArXiv: cond-mat/9909210.

[76] D. Vollhardt and P. Wölfle. In W. Hanke and Ya V. Kopaev, editors, *Electronic Phase Transitions*, page 1, Amsterdam, 1992. North-Holland.